國 立 中 央 大 學

大 氣 科 學 學 系

碩 士 論 文

Extreme Heavy Rainfall Event on 01-02 June 2017 over Northern Taiwan Area: Analysis of Radar Observation and Ensemble Simulations

研 究 生：蔡沛蓉

指導教授：鍾高陞 博士

廖宇慶 博士

中 華 民 國 一 一 一 年 六 月

國立中央大學圖書館學位論文授權書

填單日期：111/8/9　　　　2019.9 版

授權人姓名	蔡沛蓉	學 號	109621010
系所名稱	大氣科學學系大氣物理碩士班	學位類別	■碩士　□博士
論文名稱	Extreme Heavy Rainfall Event on 01-02 June 2017 over Northern Taiwan Area: Analysis of Radar Observation and Ensemble Simulations	指導教授	鍾高陞、廖宇慶

學位論文網路公開授權

授權本人撰寫之學位論文全文電子檔：

・在「**國立中央大學圖書館博碩士論文系統**」.

(✓)同意立即網路公開

(　)同意 於西元______年______月_____日網路公開

(　)不同意網路公開，原因是：______________________

・在**國家圖書館「臺灣博碩士論文知識加值系統」**

(✓)同意立即網路公開

(　)同意 於西元______年______月_____日網路公開

(　)不同意網路公開，原因是：______________________

依著作權法規定，非專屬、無償授權國立中央大學、台灣聯合大學系統與國家圖書館，不限地域、時間與次數，以文件、錄影帶、錄音帶、光碟、微縮、數位化或其他方式將上列授權標的基於非營利目的進行重製。

學位論文紙本延後公開申請 (紙本學位論文**立即公開者此欄免填**)

本人撰寫之學位論文紙本因以下原因將延後公開

・**延後原因**

(　)已申請專利並檢附證明，專利申請案號：

(　)準備以上列論文投稿期刊

(　)涉國家機密

(　)依法不得提供，請說明：______________

・**公開日期**：西元__________年_________月_________日

※繳交教務處註冊組之紙本論文(送繳國家圖書館)若不立即公開，請加填「國家圖書館學位論文延後公開申請書」

研究生簽名：蔡沛蓉　　　指導教授簽名：鍾高陞 廖宇慶

*本授權書請完整填寫並親筆簽名後，裝訂於論文**封面之次頁**。

國立中央大學碩士班研究生
論 文 指 導 教 授 推 薦 書

大氣科學學系大氣物理碩士班 學系/研究所 蔡沛蓉 研究生

所提之論文 Extreme Heavy Rainfall Event on 01-02 June 2017 over Northern Taiwan Area: Analysis of Radar Observation and Ensemble Simulations

係由本人指導撰述，同意提付審查。

廖宇慶

指導教授 鍾高陞 (簽章)

111 年 7 月 18 日

1110718

國立中央大學碩士班研究生
論 文 口 試 委 員 審 定 書

大氣科學學系大氣物理碩士班 學系/研究所 蔡沛蓉 研究生

所提之論文 Extreme Heavy Rainfall Event on 01-02 June 2017 over Northern Taiwan Area: Analysis of Radar Observation and Ensemble Simulations

經由委員會審議，認定符合碩士資格標準。

學位考試委員會召集人 陳宇能

委　　　　　員 洪景山

林沛練

廖宇慶

鍾高陞

中　華　民　國　111　年　7　月　18　日

1110718

摘要

本研究主要探討2017年6月1日至02日台灣北部梅雨鋒面個案。此鋒面於清晨滯留於台灣北部並在8小時內降下超過300毫米之累積雨量，本研究透過觀測資訊和數值模擬結果進而探討此極端降雨事件的主要肇始原因，依雷達資料和紅外線色調強化衛星圖，可將鋒面系統按生命期分為三個階段，分別為南移階段、MCS合併階段與MCS重建階段，由多都卜勒風場合成系統(Wind Synthesis System using Doppler Measurements, WISSDOM)反演得水平解析為1 km及高度解析為0.5 km之三維風場，除作為鋒面移動動力及結構探討的工具外，後續也作為與模式模擬比較時的動力參考及真實場。為了了解鋒面強降雨事件形成之條件及特徵，本研究利用美國國家海洋和大氣管理局之全球預報模式 (National Centers for Environmental Prediction, NCEP) 提供之全球最終再分析場資料 (Final operational global analysis, FNL) 進而擾動、積分取得128支系集模擬成員，並透過K-means群集分析設8小時內累積降水100毫米為閾值，最終可將128支系集分為五群，分布於台灣北部外海、北部沿海以及內陸地區，藉由反演風場及群集分析結果探討此個案中影響鋒面滯留、至災主要之中尺度-α和中尺度-β關鍵動力因素，結果顯示地形噴流對於極端降水為重要的前導因素，近一步利用模式環境場檢視發現槽與雨帶間存在著一定的相關性，隨著北方短波槽東移接近台灣，台灣西側氣壓梯度力增加，進而影響西南季風之增強，而在風場與地形交互作用下形成更強之噴流，並控制著鋒面強度及雨帶位置，使得短波槽移出之時間間接影響強降雨位置。總結來說，利用觀測及反演場除了能分析梅雨動力結構，更可進一步檢視模式模擬的表現，而在系集綜觀環境場的輔助下，有助於了解鋒面表現及其不同尺度之動力特徵。

Abstract

During 01-02 June 2017, a Mei-Yu front with accumulated rainfall over 550 mm in 8 hours occurred and stagnated at northern Taiwan in the early morning. The study examined the main features of extreme rainfall event through both observational data and numerical model simulations. Based on the observations of radar data and infrared satellite images, the lifetime of the frontal system is divided into three stages when investigating the characteristic of this event, and they are southward moving stage, MCS merging stage, and back-building stage. Three-dimensional wind fields are retrieved at 1-km horizontal resolution by the Wind Synthesis System using Doppler Measurements (WISSDOM) through two radar sites, and the synthetic winds are used as reference when comparing to model simulations. To fully comprehend the characteristics caused this event, the 128-member ensemble simulations, which were obtained and perturbed from National Centers for Environmental Prediction (NCEP) Final operational global analysis (FNL), are generated. The K-means clustering analysis is applied to classify the 128-ensemble into five groups by a threshold of 100 mm/8-hr. These five clusters illustrated different locations of extreme rainfall: some were over the ocean, and some were inland near west coast or northeast of Taiwan. Through retrieved wind field and cluster analysis, the dynamic features in both meso-α and meso-β scales are discussed to identify the key factors that can make the front stagnate and produce such heavy rainfall in northern Taiwan. The result shows that the barrier jet stands as a significant lead in the extreme rainfall process. Further inspection of large-scale simulations reveals a connection between the trough and the spatial distribution of rainbands. When the short-wave trough at north gets close to Taiwan, the intensification of pressure gradient force at west would strengthen the southwesterly flow and

result in a stronger jet which could control the strength and position of the frontal system. The movement of the trough would affect the rainband position indirectly. In conclusion, the observations not only can help us analyze the dynamic structure of Mei-Yu front but also to inspect the performance of model simulations. Further, the overview of the Mei-Yu process in different scales is revealed through the clustered ensemble simulations.

Acknowledgment

自大學期間受老師們教育薰陶下，使我毅然決然踏進研究所這個難關，但同時也是在碩士班這兩年讓我反觀到自己的成長，這兩年由衷感謝兩位指導老師鍾高陞老師及廖宇慶老師，謝謝鍾老師一直給予充足的發揮空間、資源、即時的建議與鼓勵，使我漸漸在研究道路上發現自己的價值，謝謝廖老師在口頭報告(報告 13 條要點)、分析研究上的提點，使我每次與老師討論都能修正報告上的不足，謝謝洪景山博士、林沛練老師、陳宇能老師願意撥空擔任我的口試委員，給予我寶貴的建議，讓我自己知道在研究上何處的細節需多加注意，並在口試過後中反思更多研究道理。謝謝柯緁盈大柯學姊，在博士學位最後兩年不斷被我打擾、接納我大大小小的問題，並在各種報告前給予我當頭棒喝，在我迷茫的時候給予建議。謝謝雷達實驗室的大家在這兩年的建議及支持，實驗室中的歡樂氣氛總默默地減輕研究上的壓力，在談笑歡愉過後更有動力的去完成研究。

感謝我的家人一直以來地支持我，成為我最大的避風港，讓我能無後顧之憂的努力，謝謝元瀚在這兩年包容我在各種大大小小壓力下的情緒，雖常要求我控管飲食、多運動，但必要時還是會妥協陪我吃各種美食。感謝我的朋友們，Home 群組的大家、曉明好朋友們，在疫情下並且在研究壓力下我們雖能見面、聊天的時間不多，但屈指可數的出遊與散心都成為我們這兩年無可獲缺的養分，吹翻的帳篷、去不成的畢業旅行、無止盡的逛街吃美食都深深烙在我心。謝謝我羽球的好球友們，瑋庭、容瑩、萍宜還有大氣系隊隊員們，謝謝你們總在我多次拒絕後仍熱情邀約，上研究所後就算因各種雜事、研究，使我們打球的時間越來越無規律，但每次的上場都是認真揮灑汗水，最後也要謝謝同屆的同學們，在研究的路上有大家才顯得不孤單，不論是研究上的討論或是研究、報告間的聚餐、狂歡，都是我們在碩士班短短兩年卻深刻的連結。

Outline

List of Tables

List of Figures

Chapter 1 Introduction

From May to July, namely the seasonal transition, a frequent weather system that usually brings extreme rainfall and significant damage over southern China and Taiwan, is called the Mei-Yu front. With the warm and moist southwesterly wind from East Asia Monsoon trough against the cold northeasterly wind enhanced by East Asia trough, the frontal system stays quasi-stationary and usually occurs with several types of mesoscale convective systems (MCSs), such as squall line, back-building cells or multicell thunderstorms, and provides strong instability and uplifting flow around Taiwan. Not only the frontal favorable environment would enhance the heavy rainfall, the interaction between low-level jet, the terrain, and the characteristic of the front are also keys to the weather disaster events in past studies (Chen et al., 2018; Ke et al., 2019; Tu et al., 2014; Tu et al., 2017; Tu et al., 2022; Wang et al., 2016). In the early summer, the low-level jet near Taiwan can be defined three types: the synoptic-system-related low-level jets (SLLJs), the marine boundary layer jet (MBLJ), and the barrier jet (BJ) (Chen et al., 2005; Chen & Yu, 1988; Ke et al., 2019; Kuo & Chen, 1990; Li & Chen, 1998; Li et al., 1997; Tu et al., 2017; Tu et al., 2022; Yeh & Chen, 2003). The SLLJ usually occurred as part of the secondary circulation of the frontal system at 900-700hPa by Coriolis force and enhancing the large-scale updraft motion. The MBLJ with maximum wind speed at 925hPa stands as an indicator of late monsoon period was triggered by the local scale pressure gradient effect. With terrain blocking of the prevailing wind, the BJ occurred at the downstream of the windward ridge which was at northwestern Taiwan and always appeared with wind speed over 14 m/s and at about 1 km.

Previous studies showed that LLJ, as part of secondary frontal circulation in the baroclinic system, plays a crucial and positive role to enhance the unstable environment and extreme rainfall (Chen et al., 2005; Chen & Yu, 1988; Chen et al., 2018; Chen & Li, 1995; Du & Chen, 2018; Ke et al., 2019; Kuo & Chen, 1990; Li & Chen, 1998; Li et al., 1997; Yeh & Chen, 2003; Zhang et al., 2014). In Chen and Yu's study (1988), 35 cases were chosen from May to June during 1965-1984 to study the connection between the onset of LLJ and the arrival of heavy rainfall. Through four rawinsonde stations (at Taipei, Taoyuan, Makung, and Tungkong) in Taiwan, they found the LLJ usually formed at south of the heavy rainfall and appeared 12 hours before the extreme rainfall. Then, the strength of LLJ and wind shear would decrease dramatically, and reveal the fact that LLJ is the reason rather than the result. To focus on the effect of barrier jet (BJ, defined from Chen and Li (1995) with over 14 m/s between 1-1.5 km height) at northern Taiwan, the fifth-generation Pennsylvania State University-National Center for Atmospheric Research (NCAR) Mesoscale Model (MM5) is applied by Yeh and Chen (2003) to simulate the Mei-Yu case in May 1987. Analyzing through the horizontal momentum equations, they found that the low-level jet was mainly from the horizontal advection effect and the pressure gradient effect (Chen & Li, 1995; Li et al., 1997). A pressure ridge at southwestern Taiwan was found and provided a strong dynamic force to induce the LLJ. Nevertheless, a couple of sensitivity tests revealed that changes of southwesterly wind speed, the angle of southwesterly flow, or the effect of latent heat release were correlated to the strength and location of the barrier jet. To realize the connection between rainfall and LLJ, Chen et al. (2005) investigated the relation between the LLJ and 36 heavy rainfall events at northern Taiwan by Panchiao sounding data and separated these cases with different LLJ characteristics, such as height (barrier jet and LLJ), type (single jet and double jet) and migration (migratory jet and non-migratory jet), which suggested that the weakening LLJ may be a cause of strong convection in extreme rainfall which supported the result from Chen and Yu (1988).

With the high-resolution radar data and the variational-based algorithms from Liou and Chang (2009) and Liou et al. (2012), Ke et al. (2019) focused on the detailed evolution of the 2012 Mei-Yu case on June 11-12, and analyzed the feature of barrier jet at the pre-frontal region through the high spatial (1-km) and high temporal (30-min) retrieved 3-dimensional wind field and thermodynamic field that close to reality. These algorithms not only were an efficient way to study the interaction between barrier jet and frontal system but also provided us a better understanding of the unknown region out of the observational coverages.

Nowadays, with the high-resolution progress of model simulation, many studies had focused on different cases through numerical weather prediction (NWP) model performances, and the regional ensemble forecasts have gradually become a novel method to study the model uncertainty and feature of each case (簡等, 2005; 李等, 2014; Du et al. 2018; Lin et al. 2020; Wang et al. 2021; Chung et al. 2021). Lin et al. (2020) clustered the tropical cycle (TC) track ensemble simulations of Typhoon Fanapi (2010) into the north-biased and south-biased rainband types through the accumulated rainfall pattern and landfall position which found that the topography effect played a significant role in the intensity and the track when passing through Taiwan. Considering the efficiency of getting quantitative results from the ensemble-based analysis, Du and Chen (2018) used the ensemble forecasts from European Centre for Medium-Range Weather Forecasts (ECMWF) to investigate the key factors of the rainfall event on 10-11 June in 2014. Through the linear correlations between accumulated rainfall and other variables (wind, pressure, temperature, etc.) and the subsets of good and bad members, the inland frontal rainband is found closely related to the cold front and SLLJ, while the coastal (warm-sector) rainband is mainly contributed by BLJ and low-level vortex. An ensemble-based sensitivity test (ESA) based on the 45 ensemble forecasts from different initial times, grid resolutions (2.5, 3, and 2.5-km), and Cloud-Resolving Storm Simulator (CReSS) model versions from Wang et al. (2021) indicated that some factors would affect the forecast results, which are 1) the position and moving speed of the front; 2) the position and moving speed of the low-level wind shear; 3) the moisture amount; 4) the mesoscale low-pressure along the front; 5) the frontal intensity. Especially for the former two conditions.

For the progress of the quantitative precipitation forecast (QPF), Central Weather Bureau (CWB) dedicated themselves to building a WRF Ensemble Prediction System (WEPS) (李 and 洪, 2011, 2014) and trying to find a key factor of forecasts through the system. Twenty members were used with different perturbations, planetary boundary schemes, and microphysics schemes in WEPS and hoped to cover all the forecast uncertainty. By statistics, some meteorology factors, such as equivalent potential temperature, low-level jet, moisture, that are sensitive to the frontal forecast are chosen for further analyzed. With the experience of building the ensemble typhoon quantitative precipitation forecast (ETQPF) and the knowledge of cluster analysis, they tried to apply the self-organizing map (SOM;(Kohone, 2001)) method to the 22 June 2021 Mei-Yu ensemble forecasts. Further, four scenarios, clustered from twenty members by SOM method, could diagnose the dominated meteorology factors or different background causes, e.q. the strong equivalent potential temperature axis in one while the other with high moisture flux, in a weather system. These scenarios then provide different explanations and aspects to the operational forecasts than the information only from deterministic forecast.

Considering the atmospheric physics in several scales, the atmospheric dynamic reveals highly nonlinear in both reality and modeling. Those nonlinear effects would enhance the large diversity in the forecasts; thus, the ensemble forecasts stand for an important role to increase the predictability of forecasts and capture the truth among the uncertainties. Through getting perturbations from statistics or spread of initial conditions, microphysics conditions, or the physical options in models, previous studies dedicated themselves to investigate the sources of the predictability and those impacts on the nonlinear atmospheric process (Chen et al., 2021; Du & Chen, 2018; Wang et al., 2021). With model simulations, the results might follow certain development laws controlled by some dominated factors that is sensitive to the forecast results, that is, several key conditions may lead to specific forecast results. Data mining, based on artificial intelligence (AI), machine learning and statistics, is an efficient way to find useful information from big data, such as hidden connections between some data or the certain trends. Clustering method is a technique in data mining that could cluster the similar patterns or data to same group by similarity. A requirement of the clustering in meteorology is to get the similar atmospheric trend information through members in the same cluster and the dissimilar scenarios from different sensitive factors, dynamic structure, microphysics contribution, moisture content, etc.

Previous studies gave us a better understanding of how the frontal system formed and how the jet and the front interacted by applying the observational data, reanalysis data, or deterministic model forecasts. However, most of the discussions were based on the optimal and single model simulation to investigate the frontal process. On 01-02 June 2017, a Mei-Yu front stagnated and produced rainfall with over 550 mm within 8 hours at northern Taiwan which was not well captured in model forecasts in 2017, especially the extremum north of Yang-Ming Mt.. In fact, ensemble scheme of model simulation could create different scenario of realities and capture the uncertainty of the prediction. In addition, the cluster analysis could be used to classify the members. In the current study, we would like to take the retrieved 3-dimensional wind from WISSDOM as truth and try to study the mechanism of the jet-front system. Furthermore, with the advantages of bringing a quantitative and large spread forecast by the ensembles and giving a brief classification through the cluster analysis, we try to cluster ensemble members and find the main factors of the extreme rainfall among all clusters during the Mei-Yu season by both the observation and the ensemble simulations of the 2017 Mei-Yu case. In Chapter 2, the data and methodology of the retrieved results, model simulation, and K-mean clustering are presented. The overview of the 01-02 June 2017 case is shown in Chapter 3. The result part is separated into two parts the retrieval of the 2017 case is presented in Chapter 4, while the K-mean cluster analysis of 128 ensemble simulations is presented in Chapter 5. Summary and future works of this study are mentioned in Chapter 6.

Chapter 2 Data and Methodology

2.1 Data

The observational data used in this study included the weather maps, rainfall data, and the composited radar reflectivity images from Central Weather Bureau. For the weather maps, the maps at 200hPa, 500hPa, and 850hPa were to overview the synoptic pattern of 2017 case. The rain-gauge data from surface stations, satellite imagery and composited radar reflectivity images were utilized to capture the process of the frontal system.

With the advantages of high- spatial and temporal resolution of radar data, two radars, RCWF and NCU C-Pol (Fig. 1), were chosen from the Taiwan radar network for the retrieval work (Liou et al., 2014). The S-band (10.7cm) Wu-Fen-Shan radar (hereafter RCWF, at 25.07°N, 121.77°E, 766 m) operated from Central Weather Bureau with 9 elevation angles (0.5°, 1.5°, 2.4°, 3.4°, 4.3°, 6.0°, 9.9°, 14.6°, 19.5°), and had the max scanning range to 300 km. The Nyquist velocity of RCWF was 31.0 m/s. The C-band (5.3cm) dual-Polarimetric doppler radar (hereafter NCU C-Pol, at 24.97°N, 121.18°E, 196 m) from National Central University is usually scanned with 9 elevation angles (0.5°, 1.5°, 2.4°, 3.4°, 4.3°, 6.0°, 9.9°, 14.6°, 19.5°) as the CWB operational radar with maximum distance to 250 km in the horizontal direction. The Nyquist velocity was 31.9 m/s.

A chain of radar data quality control is applied in this study, and two radars (RCWF, and NCU C-POL) are selected (Fig. 1). For RCWF and NCU C-Pol, the terrain effect and ground clutter are removed when the cross-correlation coefficient (RhoHV) < 0.8 and when the situation that high reflectivity (>40dBZ) and low radial wind speed (<2m/s) occurred simultaneously. According to the WISSDOM retrieval algorithm, the radar variables, reflectivity (ZH) and radial velocity (VR), at two analysis times that were close to each top of the hour were used and provided the hourly analysis results. The retrieved results would be shown in Cartesian coordinates with 1-km horizontal resolution and 500-m vertical resolution in Chapter 4.

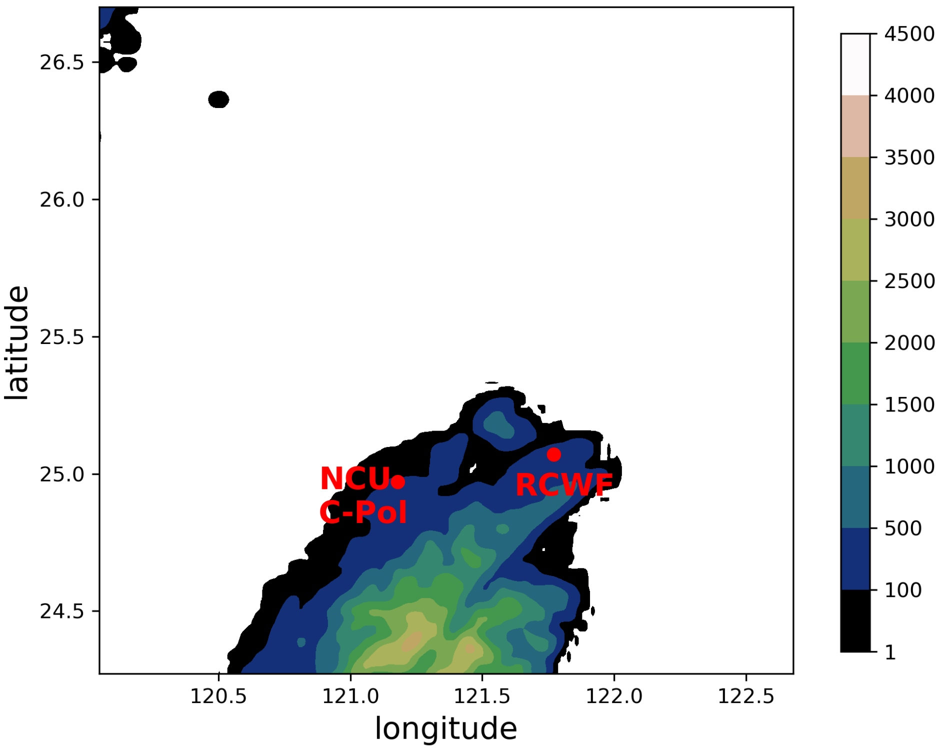

Fig. 1 The terrain height in D04. The red dots show the location of two radar sites, RCWF and NCU C-Pol.

2.2 Wind Synthesis System using Doppler Measurements (WISSDOM)

Wind Synthesis System using Doppler Measurements (WISSDOM,(Liou et al., 2014)), a variational algorithm (Liou et al., 2012; Liou & Chang, 2009), is used to combine radar data and model simulations and further retrieves the 3-dimensional wind field through the variational method. In WISSDOM, a series of weak constraints are set to make the 3-dimensional wind closer to reality. Hence, this method tries to adjust the wind field and get the best solution with 7 weak constraints in the cost function, which are (1) radial wind (2) continuity (3) vertical vorticity (4) background term (5) Laplacian smoothing filter (6) vertical velocity constraint at upper boundary and (7) at lower boundary terms.

The formula can be written as follows,

$$J_i = \sum_{M=1}^{7} J_M \tag{2-1}$$

The first term shows the correlation between the 3D wind field and radial wind observed by radar with t for two consecutive scan times, N for the number of radars, and $\alpha_{1\sim4,i}$ for the weighting coefficients of the first term which usually is set to 100 for all levels. (P_x^i, P_y^i, P_z^i) represents the location of the radar site, while (x, y, z) is the certain position in the 3-dimensional wind field. To get the final (u_t, v_t, w_t) retrieval, the terminal velocity $W_{T,t}$ is also considered. During the variational adjustment, the retrieval wind would decrease the error $(T_{1,i,t})$ between the observed radial wind and close to the observation.

$$J_1 = \sum_{t=1}^{2} \sum_{x,y,z} \sum_{i=1}^{N} \alpha_{1\sim4,i} \left(T_{1,i,t}\right)^2 \tag{2-2}$$

$$T_{1,i,t} = (V_r)_{i,t} - \frac{x - P_x^i}{r_i} u_t - \frac{y - P_y^i}{r_i} v_t - \frac{z - P_z^i}{r_i} \left(w_t + W_{T,t}\right) \tag{2-3}$$

$$r_i = \sqrt{(x - P_x^i)^2 + (y - P_y^i)^2 + (z - P_z^i)^2} \tag{2-4}$$

The second term is derived from the anelastic continuity equation. With this constraint, the solution of wind field would satisfy the incompressible fluid theory which is close to the true atmospheric state. ρ_0 is the air density constant (kg m^{-3}) usually gets from the radiosonde data or the height-averaged background data from model output, and the weighting coefficients $\alpha_{5\sim6}$ are set to 4×10^8.

$$J_2 = \sum_{t=1}^{2} \sum_{x,y,z} \alpha_{5\sim6} \left[\frac{\partial(\rho_0 u_t)}{\partial x} + \frac{\partial(\rho_0 v_t)}{\partial y} + \frac{\partial(\rho_0 w_t)}{\partial z}\right]^2 \tag{2-5}$$

The third term is the vertical vorticity term which includes the tendency term, advection term, stretching term, and tilting term in the vertical vorticity equation. The bar shows the averaged result of two analysis times. In the equation, the relative vorticity is noted as ξ, and f is the Coriolis parameter. The weighting coefficient α_7 is set to 4×10^{13} generally.

$$J_3 = \sum_{x,y,z} \alpha_7 \left\{\frac{\partial \xi}{\partial t} + \overline{\left[u\frac{\partial \xi}{\partial x} + v\frac{\partial \xi}{\partial y} + w\frac{\partial \xi}{\partial z} + (\xi + f)\left(\frac{\partial u}{\partial x} + \frac{\partial v}{\partial y}\right) + \left(\frac{\partial w}{\partial x}\frac{\partial v}{\partial y} - \frac{\partial w}{\partial y}\frac{\partial u}{\partial z}\right)\right]}\right\}^2 \tag{2-6}$$

$$\frac{\partial \xi}{\partial t} = -[u\frac{\partial \xi}{\partial x} + v\frac{\partial \xi}{\partial y} + w\frac{\partial \xi}{\partial z} + (\xi + f)\left(\frac{\partial u}{\partial x} + \frac{\partial v}{\partial y}\right) + \left(\frac{\partial w}{\partial x}\frac{\partial v}{\partial y} + \frac{\partial w}{\partial y}\frac{\partial u}{\partial z}\right)] \tag{2-7}$$

$$\xi = \left(\frac{\partial v}{\partial x} - \frac{\partial u}{\partial y}\right) \tag{2-8}$$

Due to the radar data shortage at some grid points, the background wind field from the model simulation is applied to compensate for the region without observation. Therefore, the fourth term is the background term which can support a 3D wind structure ($V_{B,t}$) and be adjusted by radial wind (V_t). The background wind is usually from the sounding data, reanalysis data, or model simulations. In the current study, the background term is chosen from a specific time of WRF model simulations that have the minimal root-mean-square error (RMSE) to the observation.

$$J_4 = \sum_{t=1}^{2} \sum_{x,y,z} \alpha_{8\sim13} (V_t - V_{B,t})^2 \tag{2-9}$$

The fifth term is the Laplacian smoothing filter term. When minimizing the cost function, there always exists an extreme value either at the high-resolution terrain region or at the grid that has a large difference between observation and background. ∇^2 is the Laplacian operator that can remove the bad signal or extremum and smooth the solutions.

$$J_5 = \sum_{t=1}^{2} \sum_{x,y,z} \alpha_{hh,hv,vh,vv} [\nabla^2 (u_t + v_t + w_t)]^2 , \nabla^2 = \frac{\partial^2}{\partial x^2} + \frac{\partial^2}{\partial y^2} + \frac{\partial^2}{\partial z^2} \quad (2\text{-}10)$$

The last two terms are the constraint of vertical velocity. Through O'Brien (1970) study, with concepts of the mass conservation theory and the friction near surface, the vertical velocity at the upper and lower boundary can be assumed to be zero in a large region. Accordingly, the summation of $(w_t)_{top}$ and $(w_t)_{bottom}$ in the domain should be minimized to zero. The following equations are:

$$J_6 = \sum_{t=1}^{2} \alpha_{17,19} \left[\frac{1}{N_x N_y} \sum_{x,y} (w_t)_{top} \right]^2 \quad (2\text{-}11)$$

$$J_7 = \sum_{t=1}^{2} \alpha_{18,20} \left[\frac{1}{N_x N_y} \sum_{x,y} (w_t)_{bottom} \right]^2 \quad (2\text{-}12)$$

To get well-retrieved frontal wind field pattern, the lower and upper boundary are set to 0-km and 15-km height and some cost function coefficients are adjusted, such as J_1 or damping terms, than previous studies (鄭, 2019; 陳, 2019). In this study, the values for the first constraint, radial wind observations, are set at 100 for the first layer and 10 for the other layers. The horizontal wind at both the bottom and the top of the fluid region is usually non-zero, and the vertical wind usually shows near zero. Because the 15-km height level in this study is near top of the troposphere, the damping terms of horizontal wind, including u and v components, are turned off, but the damping terms of the vertical axis are set to 100. Through the above settings, the WISSDOM results reveal that the maximum vertical velocity to 8 m/s and the spatial correlation coefficients (SCC) between the observed radar data and the final variational solutions reach over 0.97. The WISSDOM version in this research is the parallel execution version.

2.3 Model configuration

In this study, the simulations from the Advanced Research WRF Model version 4.2.1 were used for both the retrieval algorithm and the ensemble analysis. The physical parameterizations are chosen as: the Goddard Cumulus Ensemble (GCE) 4-ice microphysics scheme in WRF version 4 (Lang et al., 2014; Tao et al., 2003; Tao et al., 1989; Tao et al., 2016); the Yonsei University (YSU) planetary boundary layer scheme (Hong et al., 2006); the Dudhia shortwave scheme (Dudhia, 1989) and Rapid Radiative Transfer Model (RRTM) longwave scheme (Mlawer et al., 1997) in the WRF model. The National Centers for Environmental Prediction (NCEP) (0.25 x 0.25) Final operational global analysis (FNL) provided the initial condition and boundary condition to initialize the simulations. The nesting domains were set to 27, 9, 3, and 1-km horizontal resolution in domain 1 (D01), 2(D02), 3(D03), and 4(D04). The initial time of simulations was chosen from 00 UTC 01 June 2017 and with a total 30-hr simulations.

In WISSDOM, the 1-km resolution wind field results were applied as the background term ($V_{B,t}$) in (2-9) and further retrieved a 3-D wind structure at northern Taiwan with 1-km horizontal resolution and 0.5-km vertical resolution (31 levels, top to 15 km). For the ensemble, the CV3 background error covariance from three-dimensional variational (3DVAR) systems were used to simulate and produce ensemble members (Table 1). By updating some control variables, such as the stream function (ψ), unbalanced velocity potential (χ_u), unbalanced temperature (T_u), mixing ratio (q), and unbalanced surface pressure ($P_{s,u}$) in the D01 domain, 128 ensemble members were perturbed from the best deterministic forecast of the 2017 case by 3DVAR CV3 system and kept transferring the perturbations through nesting down to D02, D03, and D04.

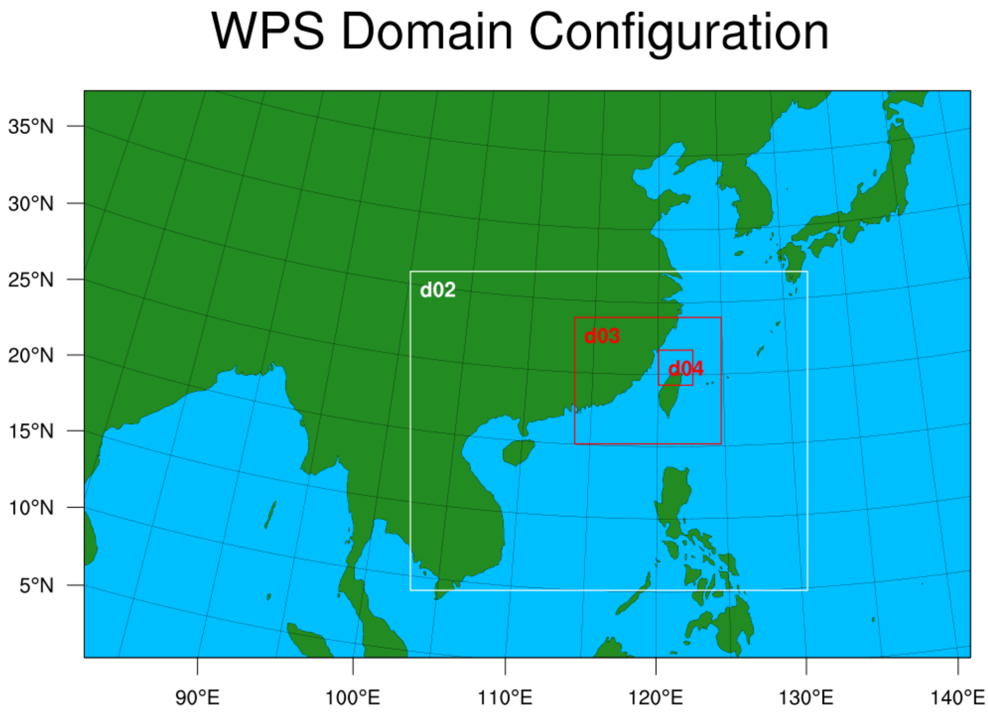

Fig. 2 The WRF domains for both WISSDOM background term and the ensemble simulation. D01 for 27km, D02 for 9km, D03 for 3km and D04 for 1km.

	settings
Model	WRF v4.2.1 (**WISSDOM BG / Ensemble**)
Initial condition	NCEP FNL (0.25°x 0.25°) Operational Global Analysis data
Initial time	2017/06/01 0000 UTC
resolution	27km / 9km / 3km / 1km
Vertical level	52 levels with 10 layers below 1km
MP scheme	Goddard Cumulus Ensemble scheme (GCE)
Grid	D01 (251*261); D02 (337*271) D03 (373*322); D04 (262*268)
Ensemble perturb	WRF 3DVAR CV3 background error covariance
Ensemble number	128 in total

Table 1 Model configuration of both WISSDOM background term and ensemble simulations.

2.4 Cluster analysis

Cluster analysis is widely used to classify a similar dataset into several homogeneous subgroups in meteorology, such as the rainfall distribution from rainfall stations, the pressure pattern among different seasons, etc., which can easily quantify the difference and similarity of variables and group them into several subgroups. Traditional clustering can be defined in two types, hierarchical method and non-hierarchical method. For the prior one, the hierarchical clustering, e.g., the single linkage method, separates the data from top to bottom until there's only one object in each subgroup which spends more time and is subjective. In contrast, the non-hierarchical method was a more efficient method that a chosen criterion is set to realize the maximum and minimum error among all members. One of the most famous is K-mean clustering which was applied in many studies, especially for the climatology, by classifying the rainfall region in Turkey (Turgu & Kömüşcü, 2019) or understanding the characteristic of the 22-year rainfall pattern (Raut et al., 2012).

The concept of K-means clustering method can be referred from the 1960s and was firstly used by MacQueen in 1967. Through previous studies, the K-means method was frequently applied on climatological studies or seasonal analysis (蘇, 2016; Teng et al. 2019). K-means clustering is a method that can separate all members into K clusters. Members in the same group are identical in characteristics, while the performance of the centroid in each group shows a large difference. The similarity between clusters is defined through the squared error. The concept can be written as: (McQueen, 1967)

$$minimize\ J1 = \sum_{i=1}^{k}\sum_{j=1}^{n}\left(x_j - \mu_i\right)^2$$

$$maximize\ J2 = \frac{1}{2}\sum_{i=1}^{k}\sum_{m=1}^{k}(\mu_m - \mu_i)^2$$

The x_i means the ith member in jth cluster, and the μ_i is the center of the ith cluster. The goal of the K-means clustering is to minimize the intra-cluster distance and maximize the mean distance between each cluster.

There are four steps to classify all samples into the best clusters (Fig. 3):

(1) Select the number of K and get 3 samples randomly from all samples as the initial centroids.

(2) Separate all members into K clusters through the min squared error between the sample and each centroid.

(3) Reset the center of each cluster which is the samples' mean of each cluster.

(4) Repeat step (2) and (3) until the centroids are immovable. Get the final clusters.

In the K-mean clustering algorithm, the number K is set by the user; therefore, it may not be the best-fit K for certain samples. The Silhouette coefficient is a way to calculate and identify the classification quality. The formula is as follows:

$$\text{Silhouette coefficient}\ \ s = (b - a)/\max(a, b)$$

a is the mean intra-cluster distance, while b is the mean nearest-cluster distance. According to variational thinking, $J1$ and $J2$, the bigger the value b and the smaller the value a, the better the clustering. Thus, when s is close to 1, the clustering result is the best. If s is close to -1, it can be said that some members are missorted. With a series of calculations in K-means clustering and silhouette coefficient, the best K that choosing from certain K values is decided. In addition, the randomly selected initial centroids may be a key error of this method, so a repeating procedure is operated to confirm that the solution is under all possibilities.

In the study, a certain period of accumulated rainfall at D04 with the constraint of 100-mm accumulated rainfall threshold as the extreme rainfall data is used to do the K-means clustering, and the center grids of the 128-ensemble determined rainfall data are set as the K-means samples. The x-axis (longitude) and y-axis (latitude) are the two variables for clustering.

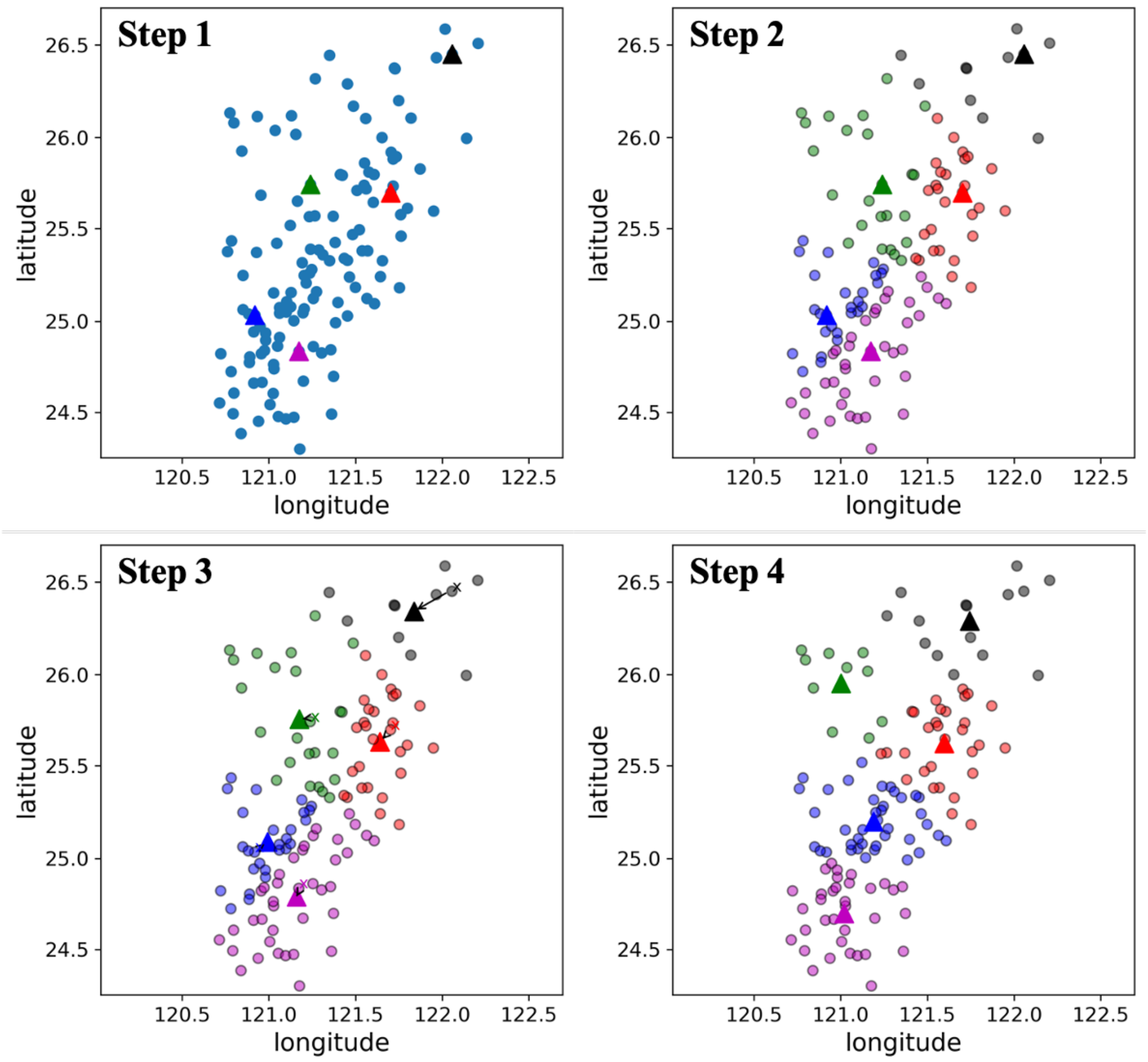

Fig. 3 The flow chart of the K-mean clustering.

Chapter 3 Case overview

3.1 2017/06/01-02 Mei-Yu case

During 01-02 June 2017, a Mei-Yu front stagnated at northern Taiwan and triggered the heavy rainfall with over 550 mm accumulated rainfall within 8 hours occurred in the early morning. For the synoptic pattern, the 500-hPa trough was over northeastern China, and Taiwan was at the pre-trough region on 1 June 0000 UTC. After 12 hours, the trough moved eastward and passed through Taiwan. Followed the 500-hPa trough, the 850-hPa trough (Mei-Yu front) kept moving southward and eastward (Fig. 4b, c), pushing the surface front to reach the north edge of Taiwan. The onset of prevailing southwesterly wind provided abundant moist warm air to the baroclinic system and enhanced the low-level convergence of frontal system. The upper-level diffluence also played a role in the favorable and unstable environment and maintained the strength of the mesoscale system (Fig. 4a).

Through the surface weather map, satellite imagery and composited radar reflectivity patterns on 1st June, a quasi-stationary front is located north of Taiwan and correlates to the eastward-moving MCSs(Fig. 4d, Fig. 5 and Fig. 6). Without the frontal effect, the rainfall on the first day mainly accumulated at the prevailing windward region, southwestern Taiwan (Fig. 7a). The surface frontal position, defined by surface wind shear line and thermal gradient from NCEP FNL reanalysis data, indicated that the surface front was blocked at north of Yang-Ming Mt. for about 8 hours in the early morning and was inconsistent to the mid-level wind shear line which displayed more south and enhanced heavy rainfall at prefrontal region (Fig. 6). With the movement of the mid-level trough and the blocking effect of the low-level jet, the system moved southward in the early morning of 2 June 2017 and then oscillated at the middle of

Taiwan during 2-3 June 2017, producing extreme rainfall at the northern coastline, middle and southwestern windward region of Taiwan (Fig. 6, Fig. 7b). For this study, we would mainly focus on the system progress from the pre-frontal period to the landfall of the front (1 June 0000 UTC to 2 June 0200 UTC).

Recently, many studies have focused on the extreme rainfall Mei-Yu case during 01-04 June 2017 (施, 2019; Tu et al., 2017; Chung et al., 2020; Wang et al., 2021; Tu et al., 2022) and found different reasons to explain the process and mechanism of this extreme rainfall.

Tu et al. (2022) studies the 2017 case through a high-resolution (1-km for D04) WRF model. Due to the shallow cold air of this case, they found the front hard to pass through the Yang-Ming Mountains and triggered heavy rainfall in the Taipei Basin as the 11-12 June 2012 Mei-Yu case but just stagnated at the north of the terrain. With the analysis of the Automatic Rainfall and Meteorological Telemetry System (ARMTS) data, there were two temperature drops discovered in some sites and might be resulted from the evaporative cooling in two river valleys, the Tamsui River and Keelung River valleys, and second, the arrival of the Mei-Yu front. After The evaporative cooling effect would then strengthen and thicken the cold air and make it able to move southward inland. In Wang et al. (2021)'s study, 45 ensemble members are utilized to investigate the predictability of the 2017 extreme rainfall event and the factors that are sensitive to the forecast results within 6 hours at northern Taiwan. The complicated precipitation process in model simulations was found sensitive to the surface front movement, low-level wind shear line, moisture content, mesoscale low, and the strength of front.

In this study, similar to the previous studies, our target is to find the main dynamic factors that may induce the northern Taiwan extreme rainfall, so the frontal landfall period (01-02 June 2017) is chosen for further examination. Further, through the different forecast possibilities provided by ensembles, we tried to understand what factors dominated the most the in different stages of the procedure.

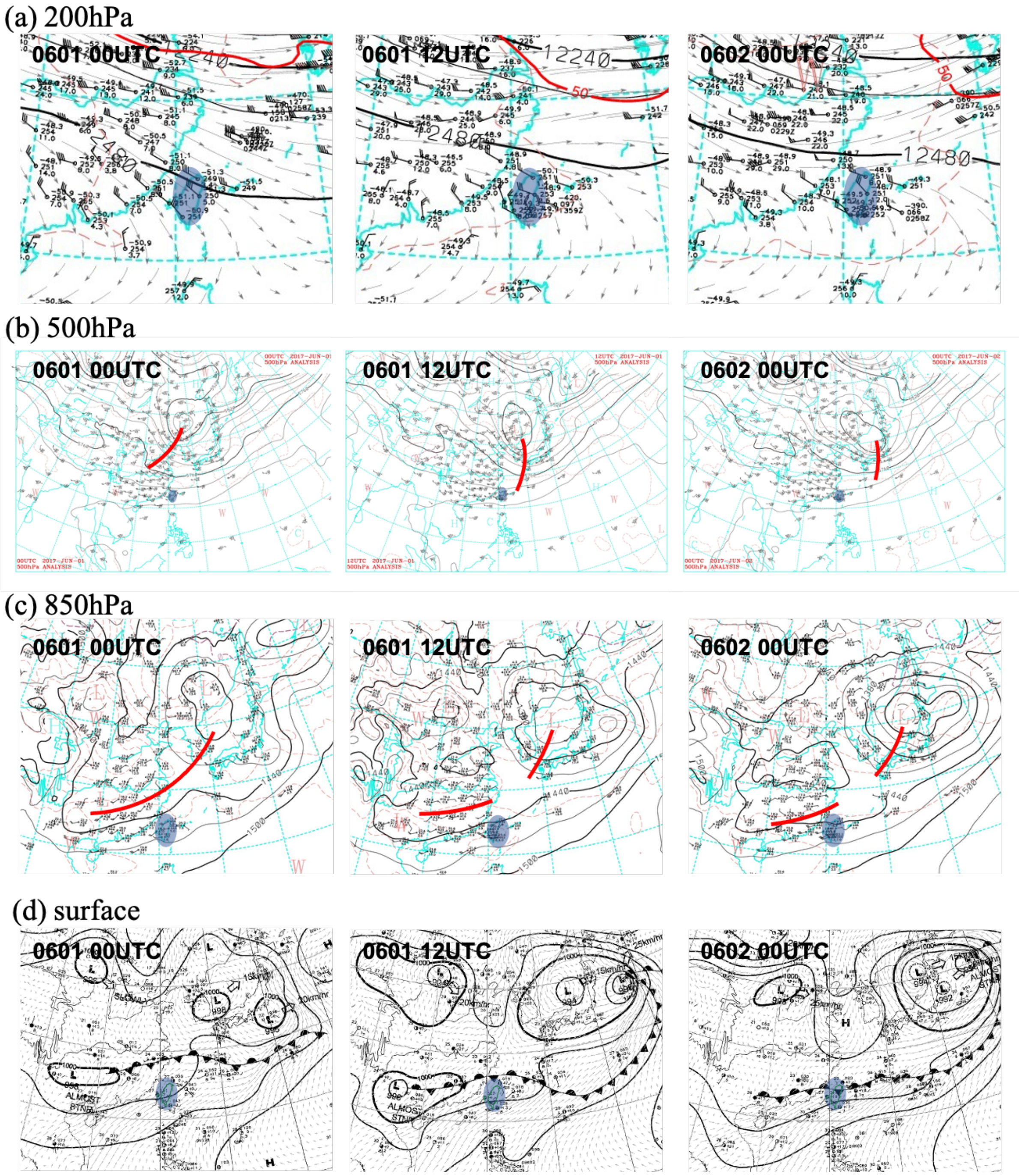

Fig. 4 Weather map (a) at 200 hPa (b) at 500 hPa (c) at 850 hPa (d) at surface from 0000 UTC 01 June to 0000 UTC 02 June 2017 with interval 12 hours from Central Weather Bureau (CWB). The blue shaded regions indicate Taiwan location, and the red contours are the trough positions.

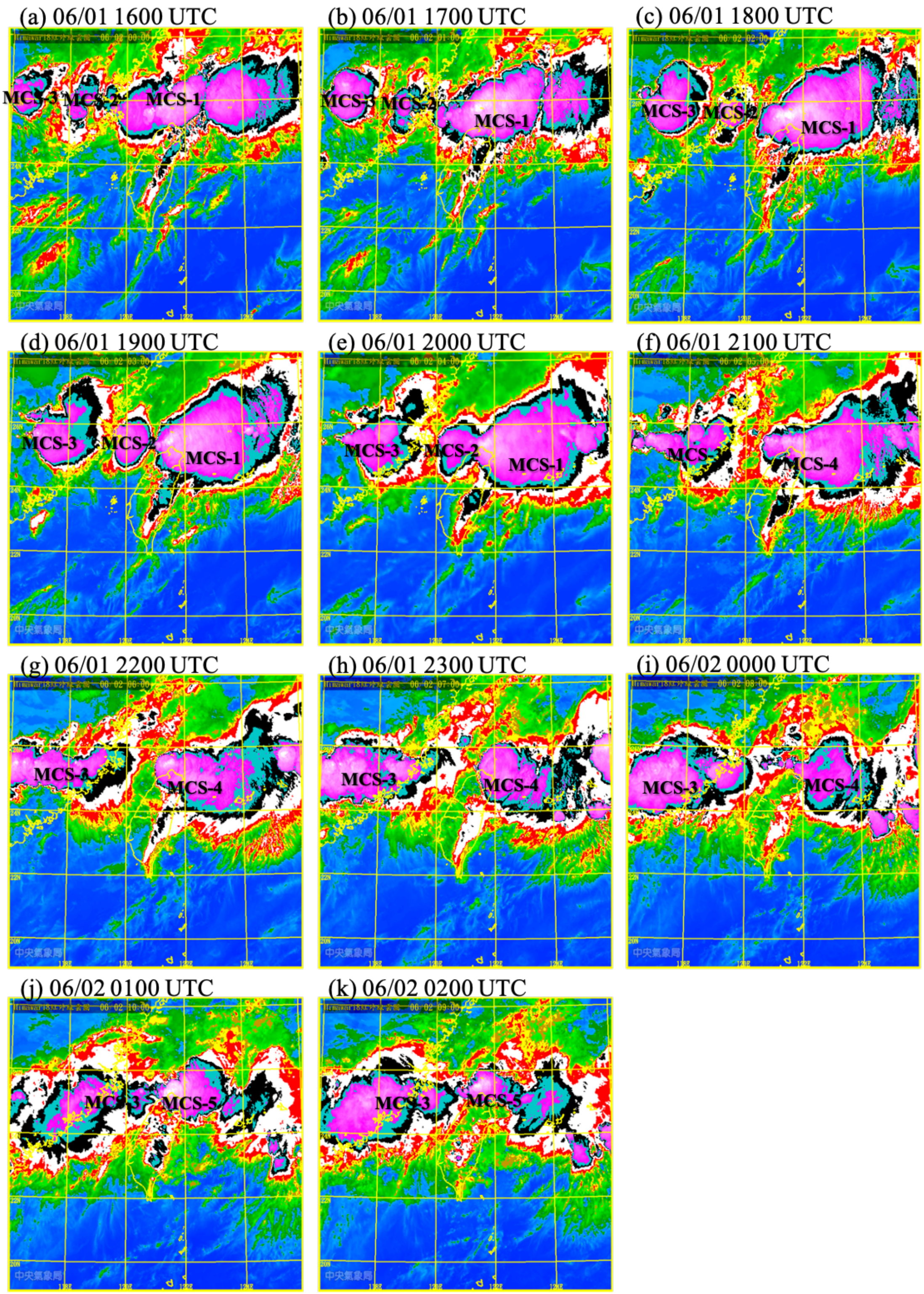

Fig. 5 Color-enhanced infrared satellite images from 01 June 1600 UTC to 02 June 0200 UTC.

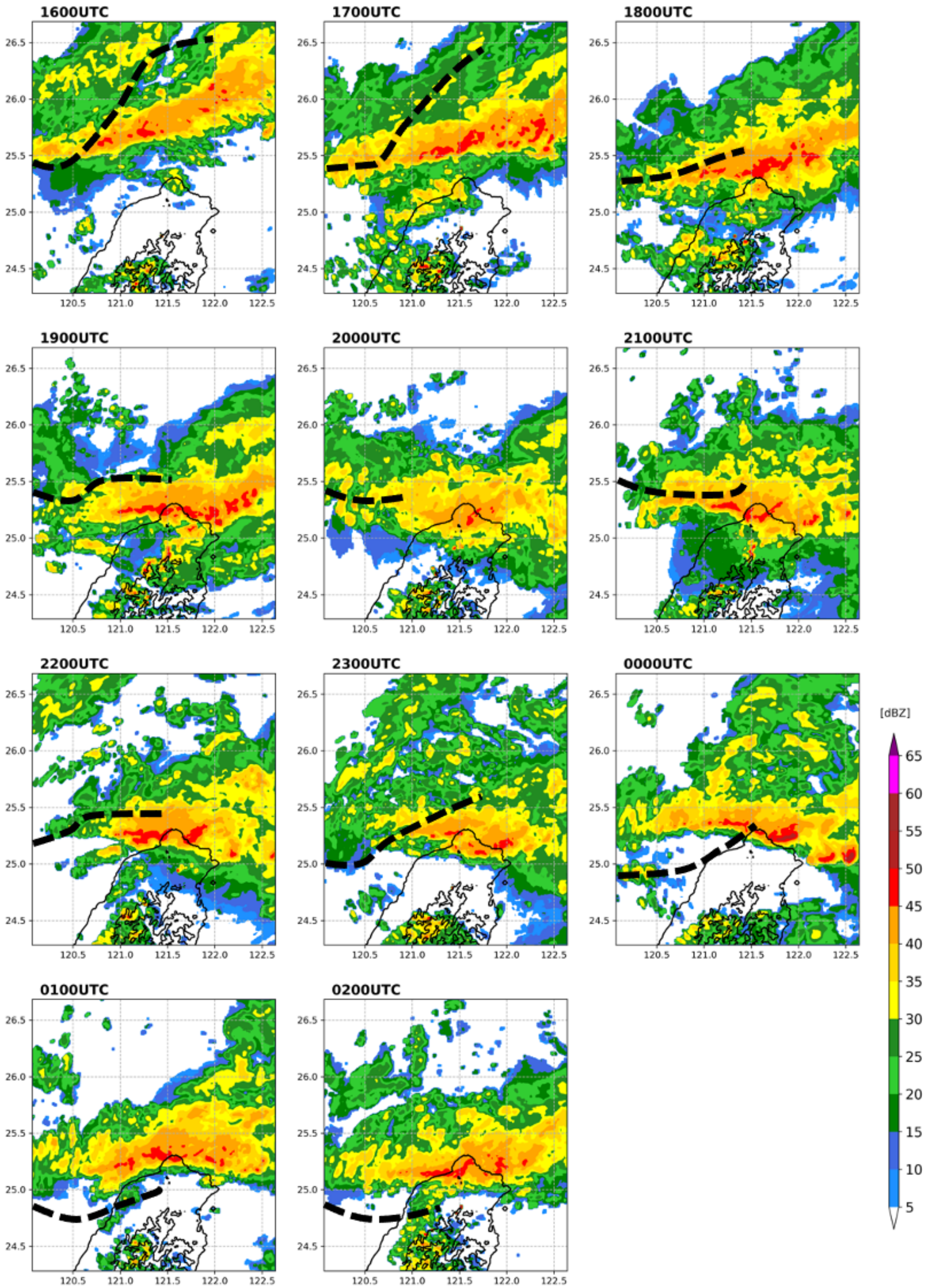

Fig. 6 The composited radar reflectivity of RCWF and NCU C-Pol and surface front defined by NCEP FNL reanalysis data (dashed line) from 01 June 1600 UTC to 02 June 0200 UTC.

(a) (b)

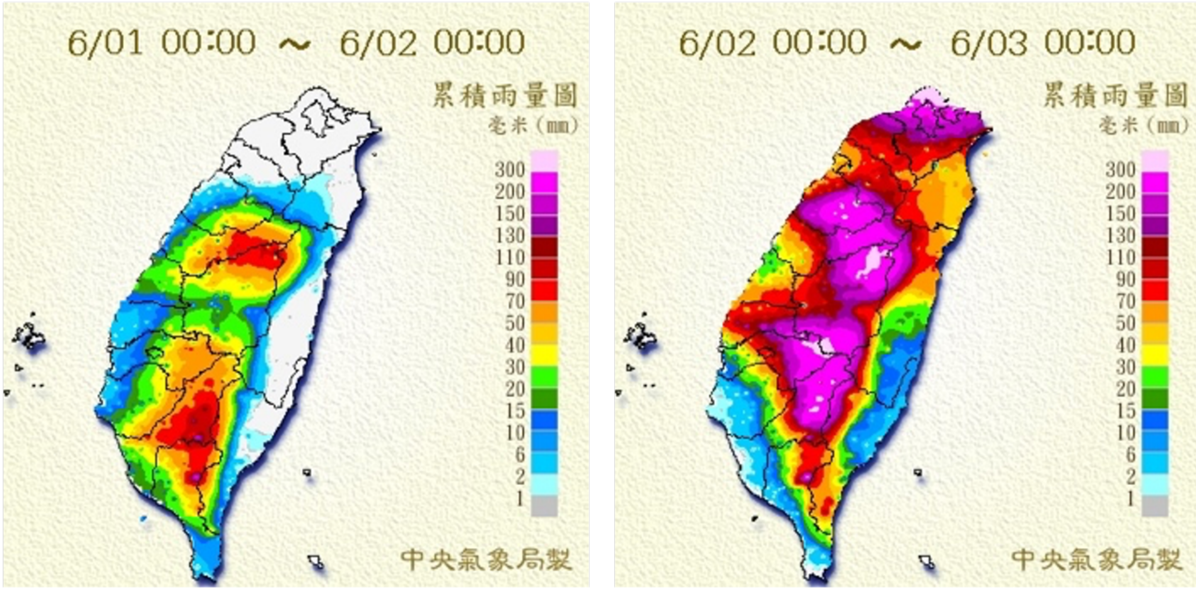

Fig. 7 The daily accumulated rainfall on (a) 01 June 2017 and (b) 02 June 2017.

Chapter 4 Result: Part I -WISSDOM

In this part, the variational algorithm (Liou et al., 2012; Liou & Chang, 2009), Wind Synthesis System using Doppler Measurements (WISSDOM, (Liou et al., 2014)), is used to analyze the 3D wind fields of the Mei-Yu case in 2017 through the high temporal and spatial resolution resources.

4.1 Retrieval of 2017 Mei-Yu case

The lifetime of the frontal system from 16UTC June 01 to 02UTC June 02 is divided into three stages when investigating the characteristic of this event, and they are southward moving stage, MCS merging stage, and back-building stage.

4.1.1 Stage 1: Southward moving stage

At 1600 UTC on 1 June, three eastward-moving MCSs are aligned in an east-west direction in the north of Taiwan (Fig. 5a). In the first stage (Fig. 8a–d), the MCS-1 is northwest of Taiwan while the front is located at about 26°N by the vertical motion and the wind shear line, and the prevailing southwesterly wind is over the Taiwan Strait and extends north of Taiwan. With time, the MCS-1 moves eastward and enhances the front moving southward until reaching the north edge of Taiwan (Fig. 10a, b). In response to the terrain blocking, the speed of the system's southward movement decreases, and the southwesterly turns along the mountain ridge, forming a local maximum at the pre-frontal area, which is the barrier jet area (Fig. 10a, and Fig. 11a). During this period, the pre-frontal convections with rapid growth bring a slight vertical motion at the north of the Snow Mountains (Fig. 10b, and Fig. 11b). With the effects of the frontal instability, the other positive vertical motion displays at the front position at 1800 UTC and

1900 UTC (Fig. 10c, and Fig. 11c). Between two of the updrafts, a downward motion forms due to the secondary circulation that blocks the barrier jet and weakens the connection of the convective system and low-level wind. At 18 UTC, the strength of the front reaches its maximum in the first stage when the MCS-1 is closest to northern Taiwan and results in a downdraft motion (cold pool) behind the front in the next hour (Fig. 5c, d, and Fig. 11d).

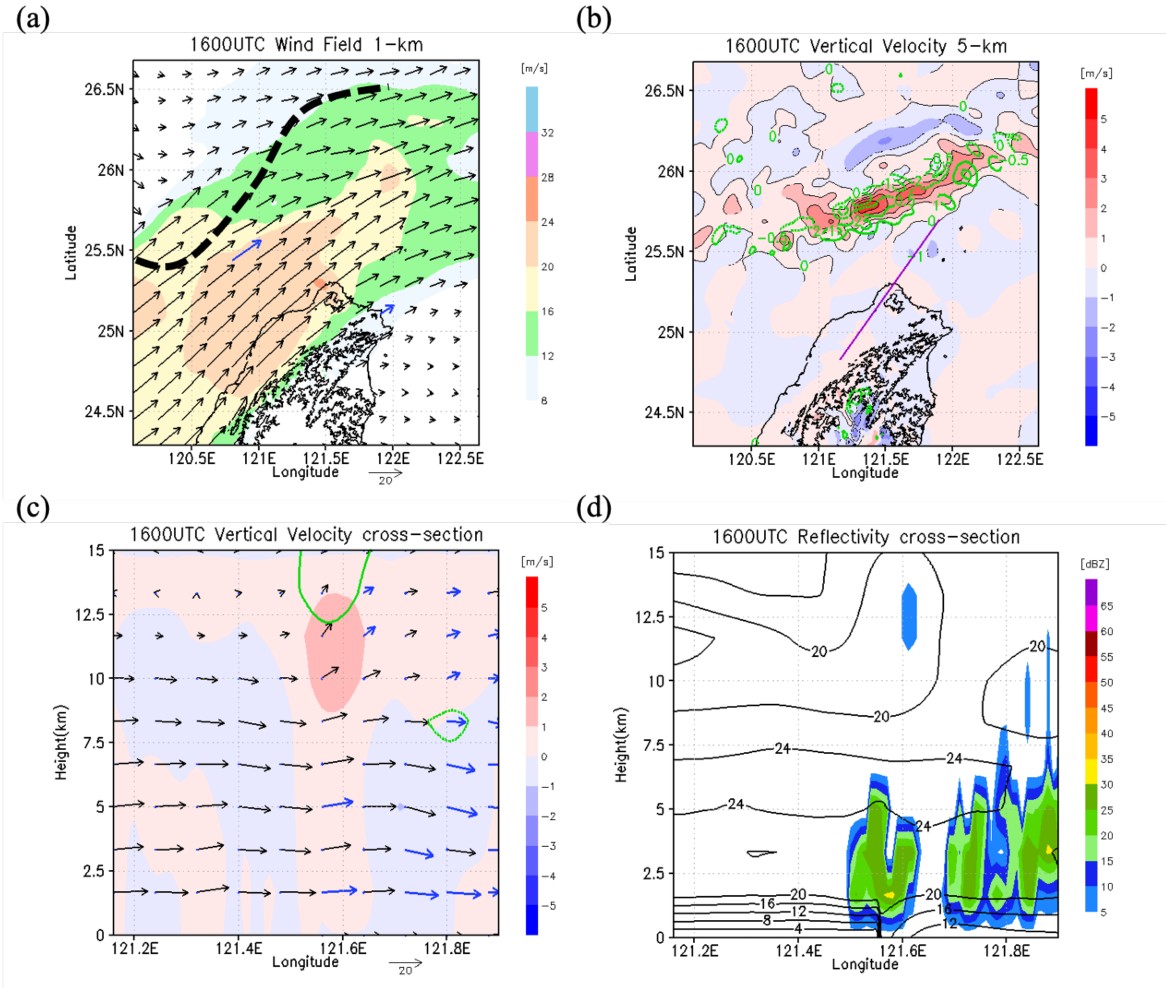

Fig. 8 Retrieved result at 1600 UTC 01 June 2017. (a) The horizontal wind direction (vector) horizontal wind speed (shaded, unit: m s^{-1}) at 1km, and the blue vectors indicate the retrieved wind. The thick dashed line reveals the surface front defined by NCEP FNL reanalysis data. (b) The vertical velocity (shaded, unit: m s^{-1}; black contour represents the radar coverage region) at 5km and the divergence region (green contour, unit: 0.5×10^{-3} s^{-1}) at 4.5km. (c) Vertical cross section (see purple line from b) of vertical velocity (shaded, unit: m s^{-1}), wind direction (vector,

blue vector for radar coverage region) and divergence region. (d) Vertical cross section (see purple line from b) of radar reflectivity (color shaded, unit: dBZ) and horizonal wind speed (contour, unit: m s^{-1})

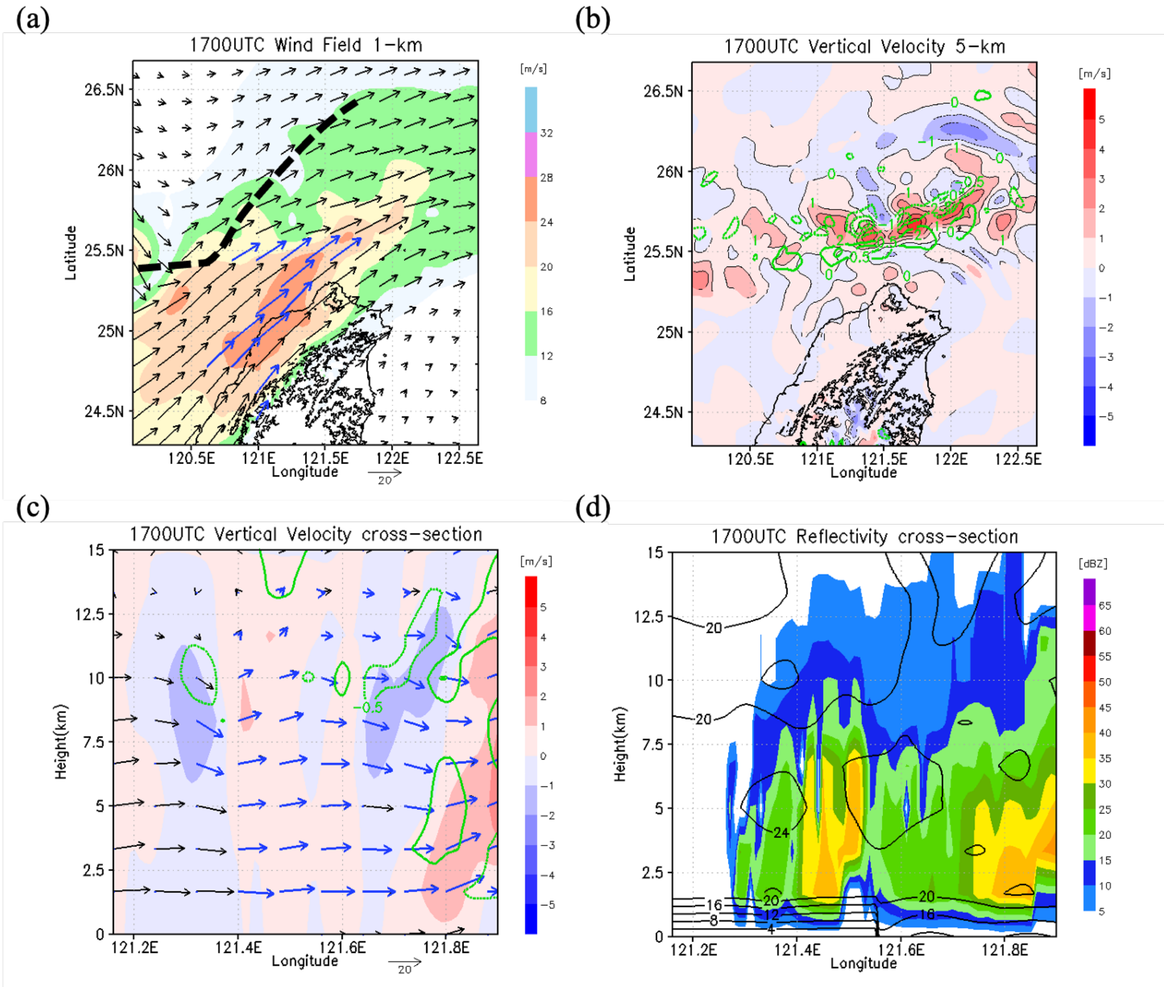

Fig. 9 Same with Fig. 8, but for 1700 UTC 1 June 2017.

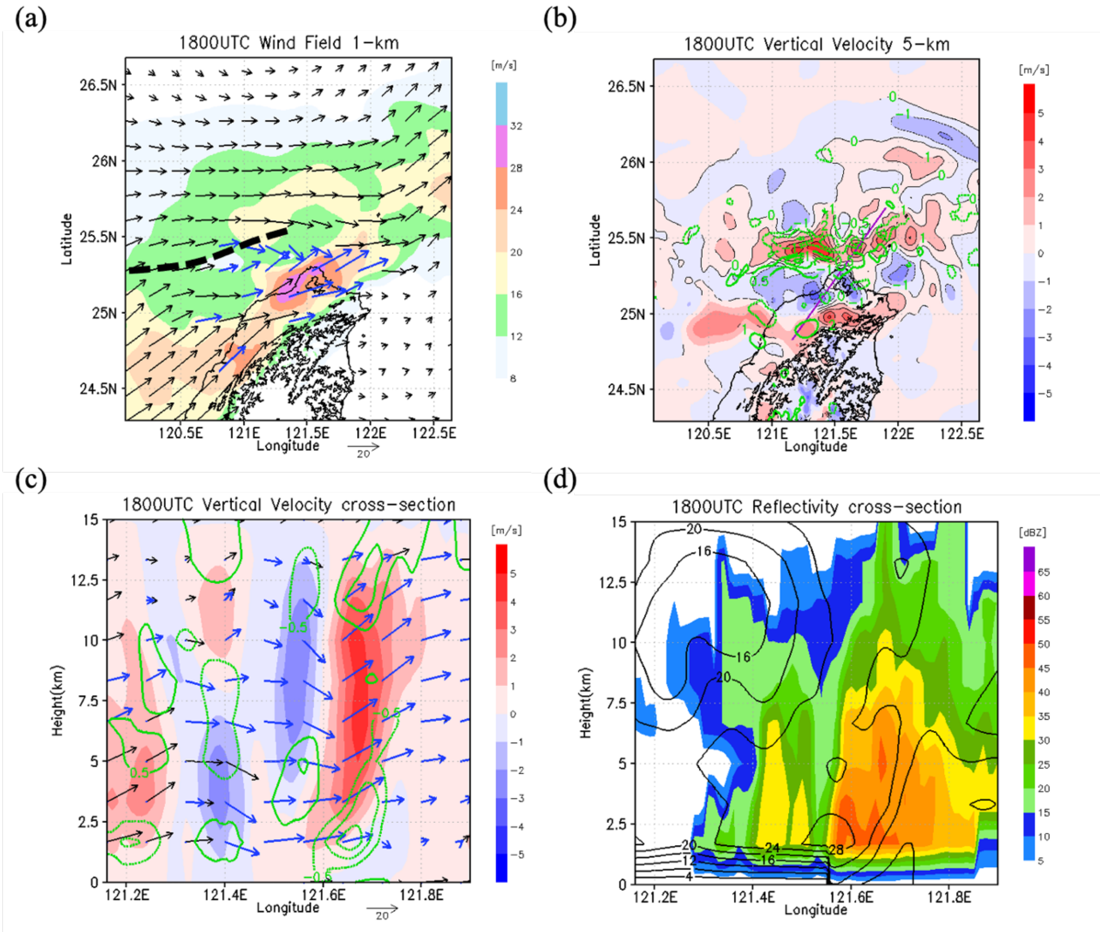

Fig. 10 Same with Fig. 8, but for 1800 UTC 1 June 2017.

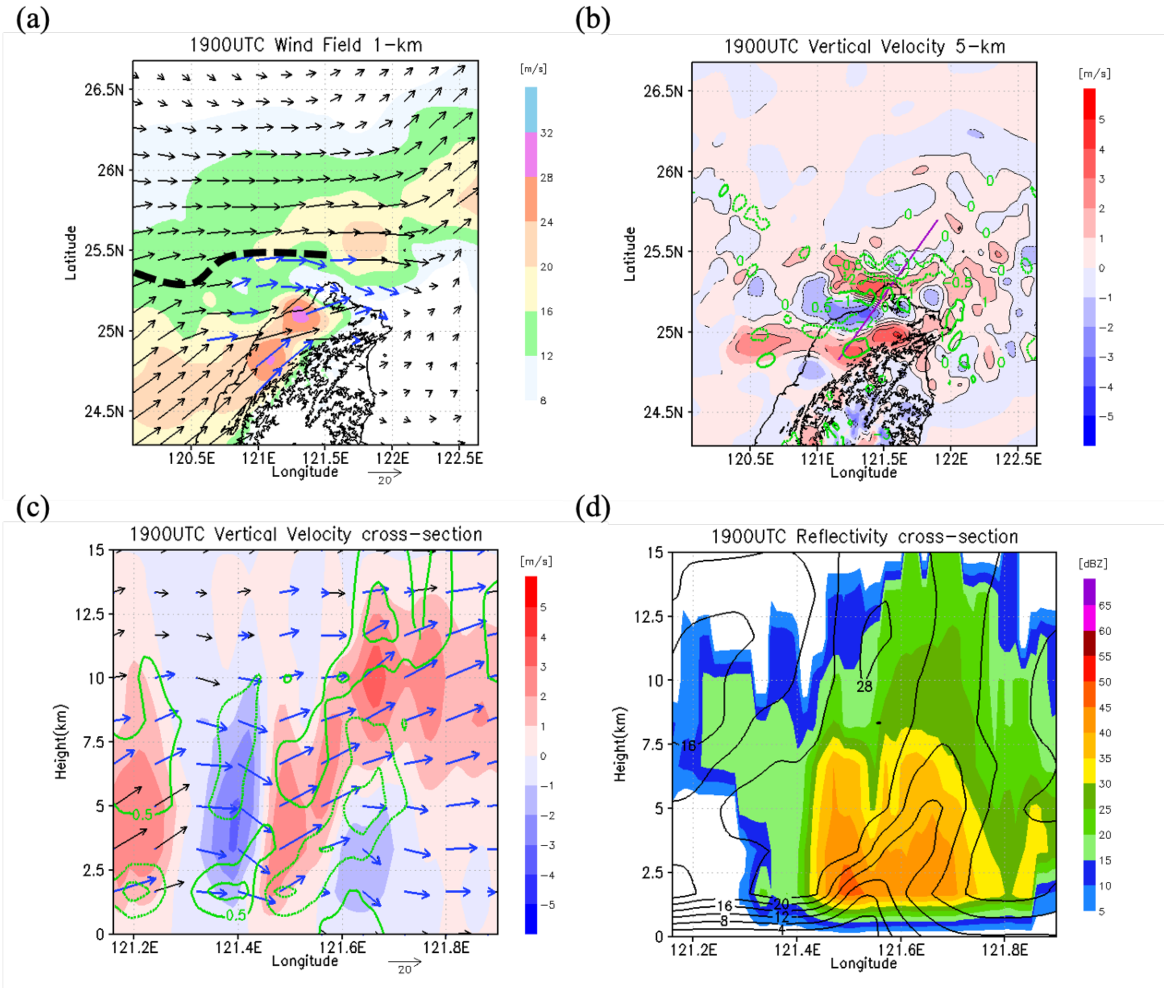

Fig. 11 Same with Fig. 8, but for 1900 UTC 1 June 2017.

4.1.2 Stage 2: MCSs merging stage

During Stage 2, at 2000 UTC, the MCS-2 proceeds further eastward and starts to merge with the quasi-stationary MCS-1 (Fig. 5e–f), while the front with strong vertical velocity is in northern Taiwan. The southwesterly wind prevails in the pre-frontal region, while the wind at the north remains westerlies and provides enough convergence and instability to the front (Fig. 12a, b). A tilted structure, similar to the vertical cross-section of vertical velocity at 1900 UTC, is shown at around 121.5ºE, and the mid-to-low-level downward motion behind it may result from the precipitation process (Fig. 11c, and Fig. 12c). In the 1-km horizontal wind pattern, in response to the weakening of secondary circulation, a widespread extreme low-level wind speed exists in northwestern Taiwan during the reorganization period of two MCSs at 2100 UTC (Fig. 5f, Fig. 13a). For the next hour (2200 UTC), the contributions of both the MCSs merge (into MCS-4) and the barrier jet are factors in forming the strongest and the most tilted frontal structure (Fig. 5g, and Fig. 14). Being pushed against by the jet, the front stalls at the north edge of Taiwan as the result of jet-front interaction; in addition, pre-frontal line convections also play a role in the extreme rainfall, as Ke et al. (2019).

During the next two hours (6/1 2300 UTC to 6/2 0000 UTC), the MCS-3 reaches its mature stage and then decays northeastward (Fig. 5h–i, Fig. 15, and Fig. 16). In response to the northward motion of front, the inland pre-frontal strong wind decreases and, meanwhile, results in a much weaker vertical motion. The wind direction north of the system turns clockwise to northwesterly wind and maintains the strength of convection.

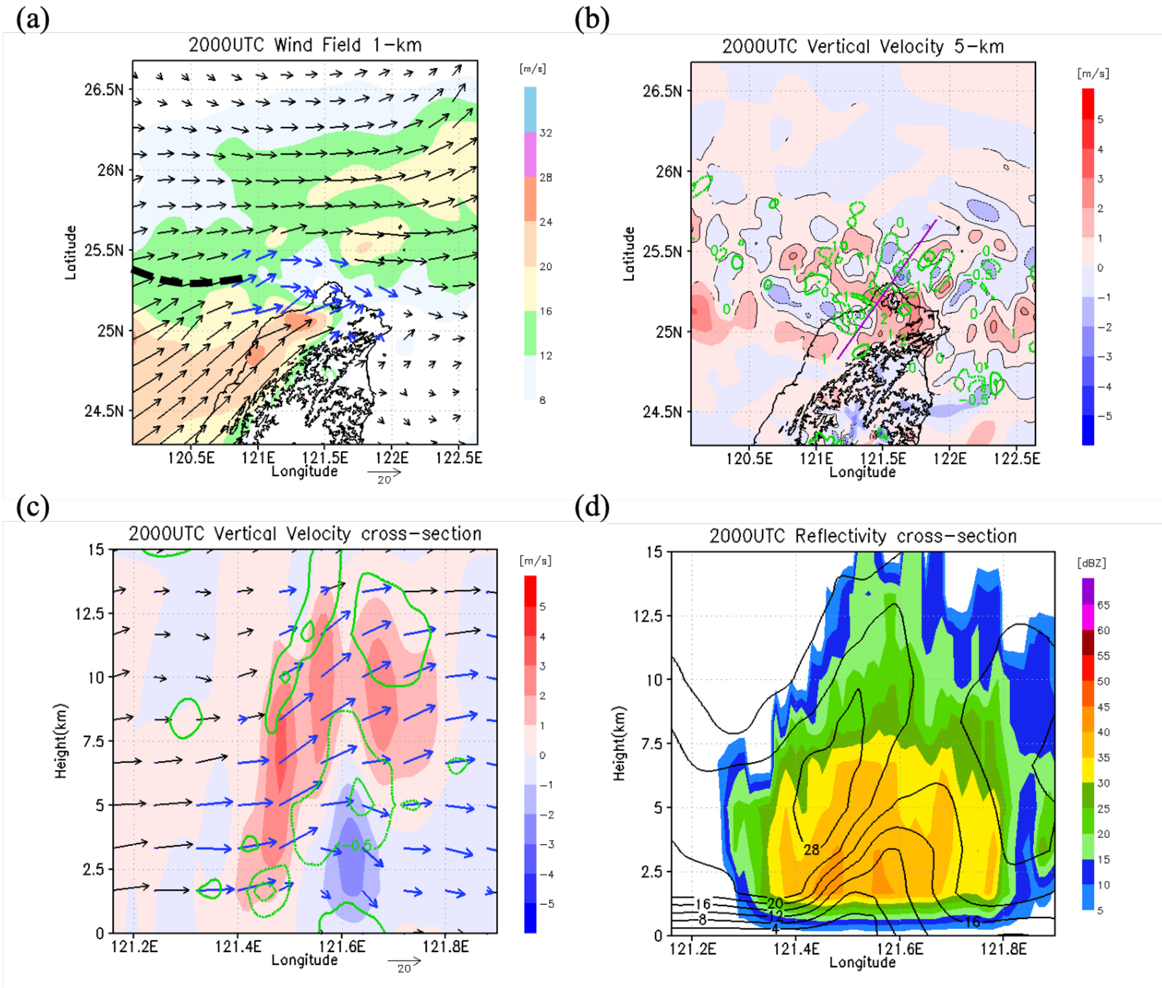

Fig. 12 Same with Fig. 8, but for 2000 UTC 1 June 2017

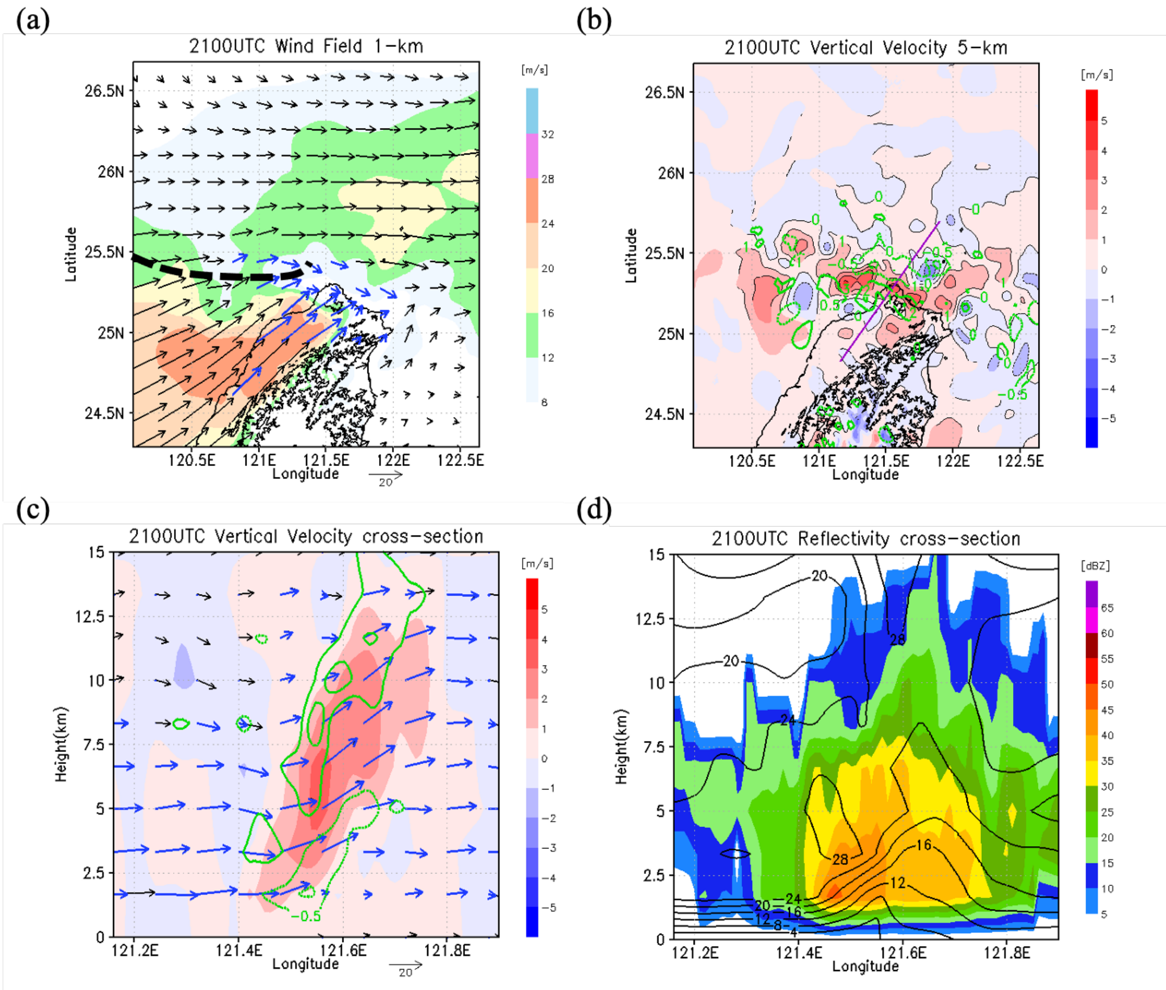

Fig. 13 Same with Fig. 8, but for 2100 UTC 1 June 2017.

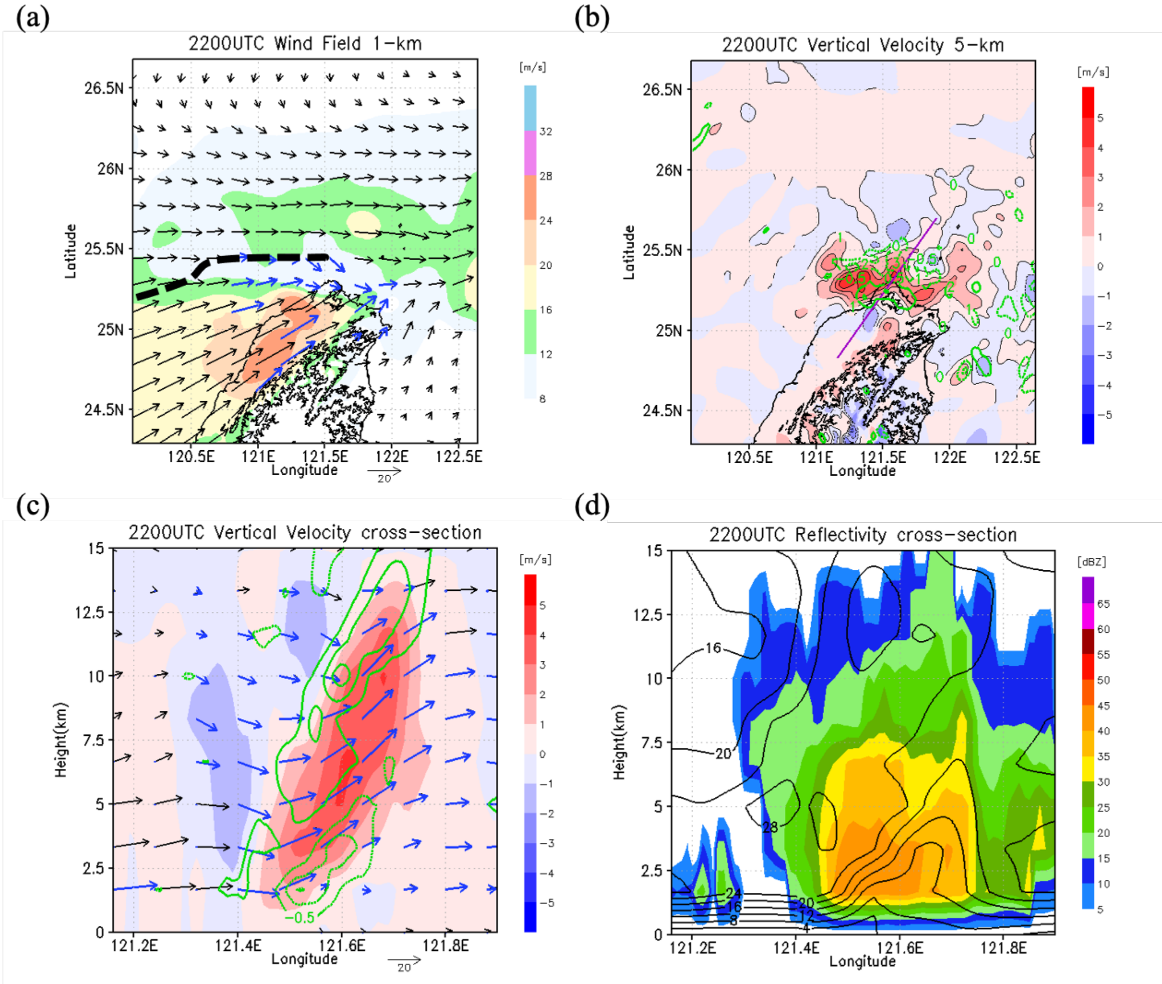

Fig. 14 Same with Fig. 8, but for 2200 UTC 1 June 2017.

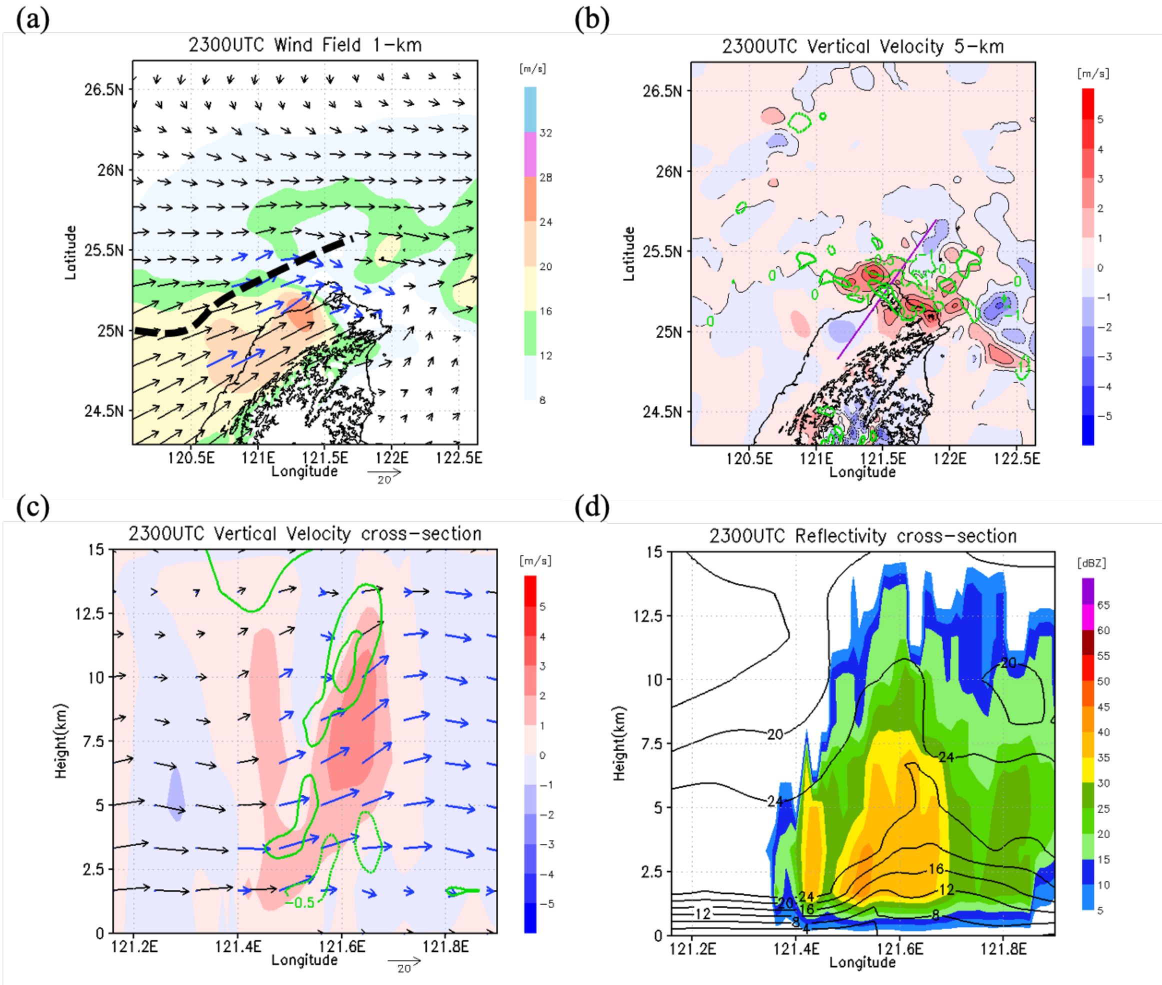

Fig. 15 Same with Fig. 8, but for 2300 UTC 1 June 2017.

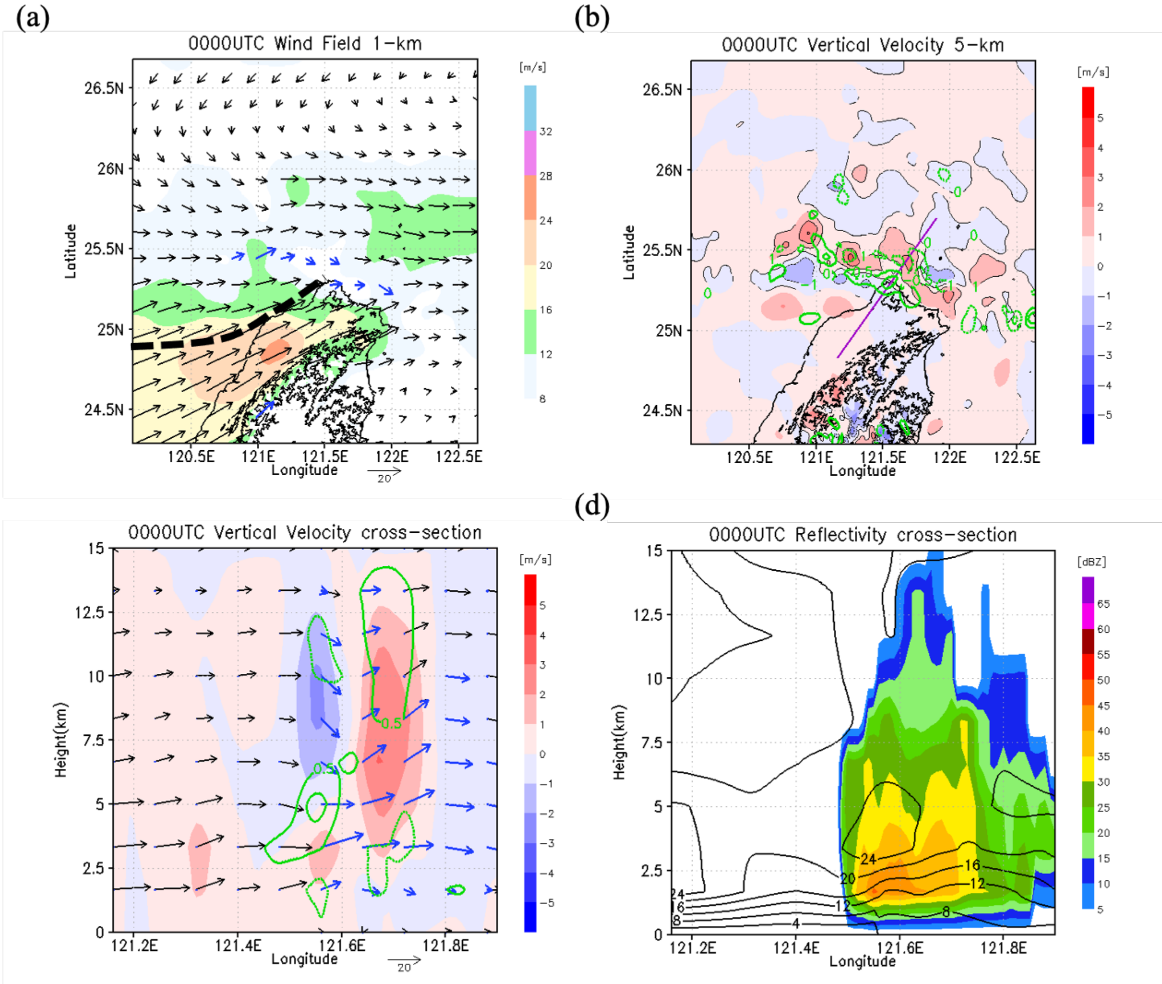

Fig. 16 Same with Fig. 8, but for 0000 UTC 2 June 2017.

4.1.3 Stage 3: Back-building stage

Similar to the back-building process, a new development occurs at west of the weakening MCS-4, which is named the MCS-5 (Fig. 5i–k). New cells form at the west of the front and propagate eastward, thus resulting in repeated system growth and southward movement. The system starts to move southward at 0100 to 0200 UTC on 02 June, and the vertical velocity increases and becomes more non-tilted against the strong pre-frontal low-level flow and terrain blocking (Fig. 17, and Fig. 18). With the contribution of a strong barrier jet (~27 m s^{-1}) at 0100 UTC (Fig. 17a), the closer the Mei-Yu front shifts, the narrower and stronger the convections form. As a result, the frontal system can cross the Yang-Ming Mountains and keeps moving southward, and thus proving the tight connection between the barrier jet and the frontal system.

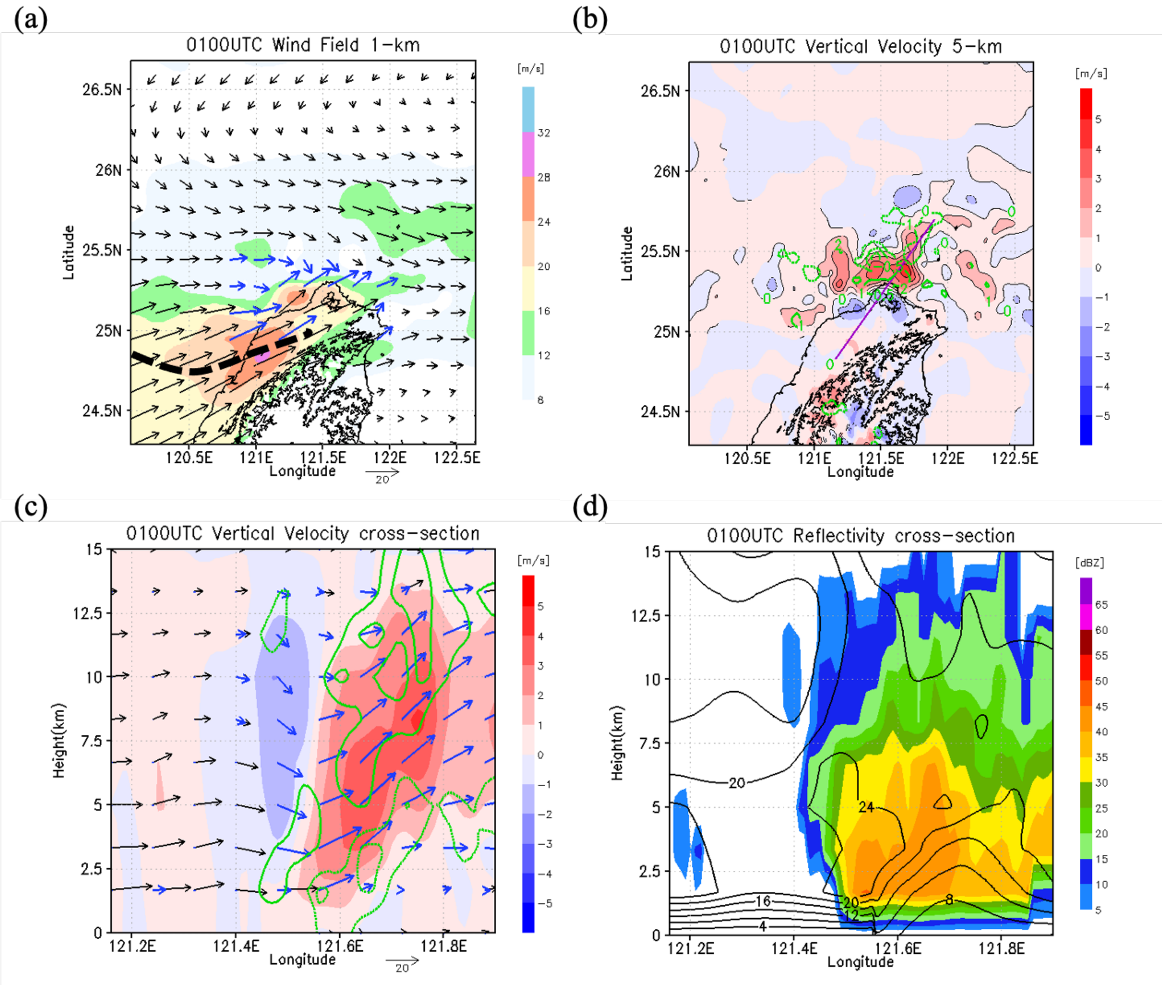

Fig. 17 Same with Fig. 8, but for 0100 UTC 2 June 2017.

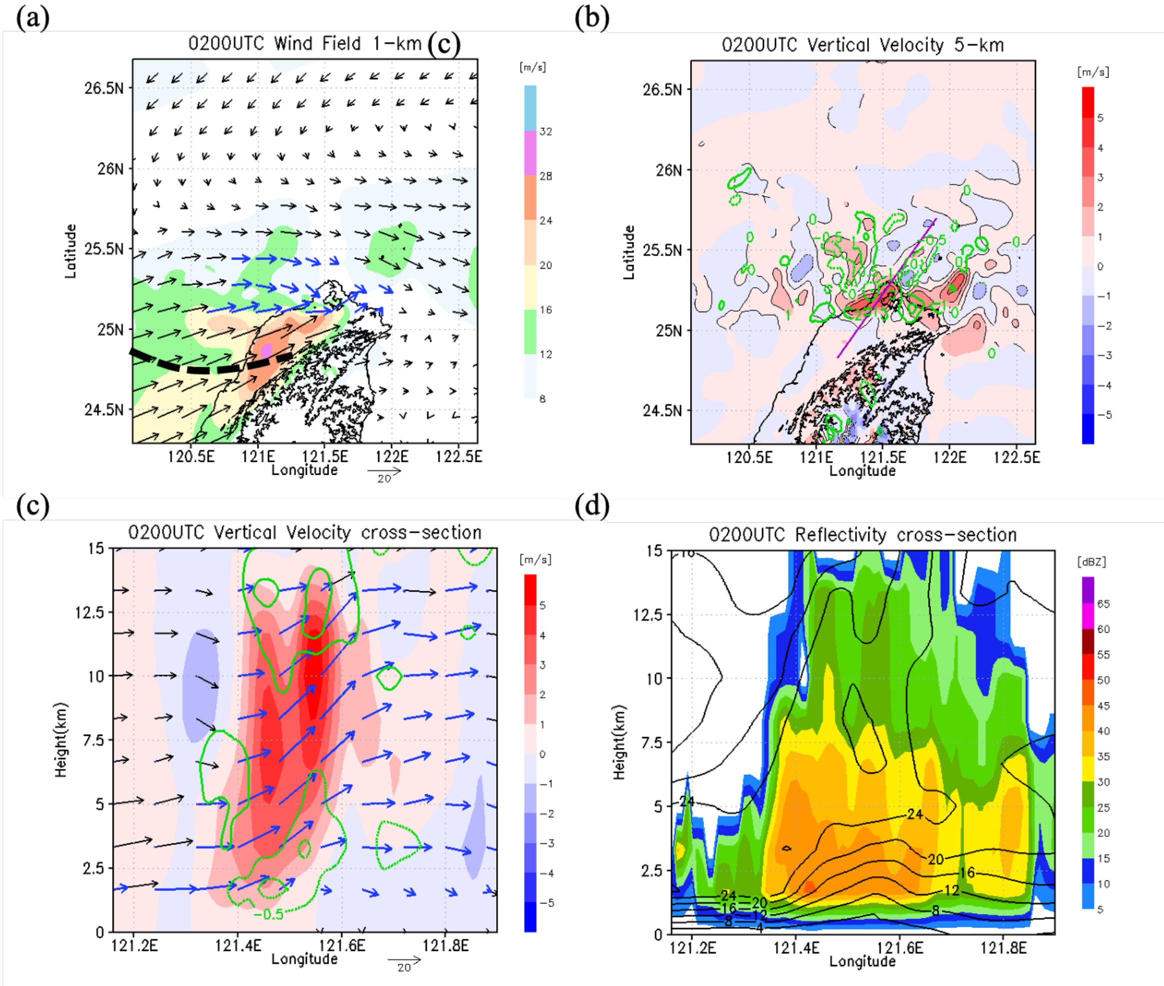

Fig. 18 Same with Fig. 8, but for 0200 UTC 2 June 2017.

4.1.4 Hovmöller diagram

The Hovmöller diagram of composited radar reflectivity (RCWF and NCU C-Pol) when Mei-Yu front landfall would be shown in this section to understand the evolution of the front and wind field and also their relationship. The time interval from 1800 UTC 1 June to 0200 UTC 2 June is 30 minutes. Both the Hovmöller longitude- and latitude-time diagrams of radar reflectivity reveal that the frontal system is in a quasi-stationary state, centered at about 121.5°E and 25.2°N (Fig. 19). The wind speed at the east of 121.5°E is not considered due to the turbulent flow from complex terrain. Due to the MCS-1 eastward movement (Fig. 5), the system gets weaker and southward during the southward moving stage (1800 UTC to 1900 UTC) but with the maintenance of a strong barrier jet (1 km) at south of the front. During the next period (MCSs merging stage, 2000 UTC to 0000 UTC), the rainband stalls at north of the Yang-Ming Mountains for about 3 hours and accompanies by the strengthening northerlies and the weakening jet. Furthermore, the southerly wind reaches its maxima (over 18 m/s) at 2100 UTC and minima at 0000 UTC on 02 June and moves slightly inland as in Ke et al.'s study (2019). This experience supports the previous research that the barrier jet is not the effect but the cause (Chen and Yu,1988; Chen et al., 2005). As a result, the strong wind provides sufficient dynamic force to compete with the change of northerly flow and enhances even stronger vertical motion in the next hour (Fig. 14c). In response to the eastward-propagating of the merging MCS to about 25.3°N in the second stage, the frontal system becomes weaker and moves even northward. After the new MCS-5 getting closer and the reorganization of the northerly wind and southerly jet in the back-building stage, the front keeps moving southward after 0100 UTC and indirectly makes the jet strengthen.

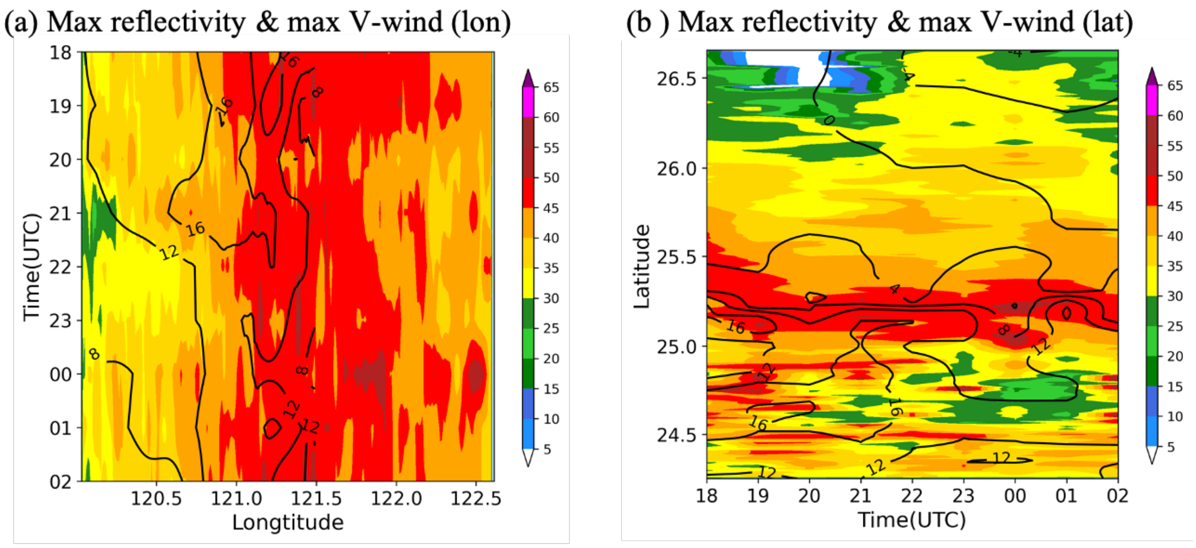

Fig. 19 (a) The Hovmöller diagram of max reflectivity (shaded, interval is 5 dBZ) and max meridional wind at 1 km at west of 121.5°E (black contour, interval is 4 m/s) along longitude, and (b) along latitude in the WISSDOM retrieval domain.

Chapter 5 Result: Part II – Cluster analysis

With the WISSDOM retrieval wind field as the truth in Chapter 4, in this section, the 128 ensemble results would be further investigated and compared to retrieval results through mean patterns and the cluster analysis of which. The factors that may result in extreme rainfall will also discuss during the frontal progress.

5.1 Performance of ensemble simulations

For the 1-2 June 2017 case, the 8-hr heavy rainfall is selected from 1 June 1800 UTC to 2 June 0200 UTC when the wind shear line and max radar reflectivity in WISSDOM trigger at the edge of northern Taiwan. Through the repeating K-means clustering and Silhouette score calculation, the best result we got was when K equaled 5. These 5 clusters are located in 1) the inland region, 2) the north edge of Taiwan, and 3) 4) 5) the offshore region at the north of Taiwan (Fig. 20). The members in each cluster are 37, 46, 22, 13, and 10 in sequence.

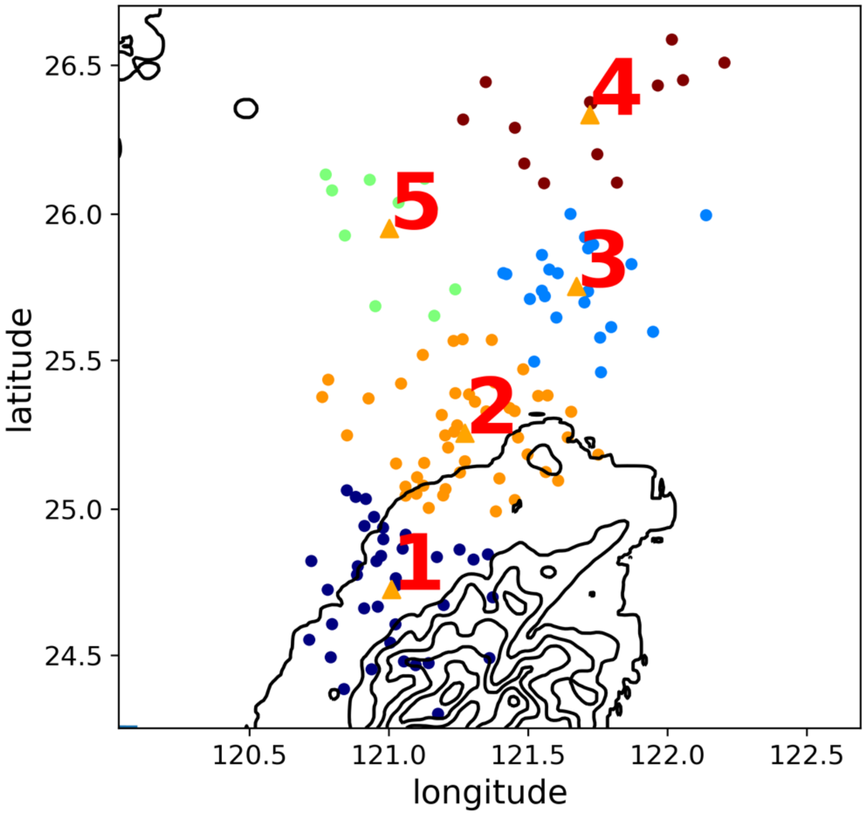

Fig. 20 K-means clustering results for 1 June 2017 case.

The ensemble mean of 8-hr rainfall is shown in Fig. 22, while the mean precipitations of 5 clusters are shown in Fig. 24. Compared to the observed rainfall data from CWB (Fig. 21), the ensemble mean rainfall appears a similar E-W extreme value at the north of the Yang-Ming mountains and decreases southward. A large spread of rainfall pattern is along with the west coast of Taiwan with north-northeast – south-southwest orientation and has the maxima at northwestern coast (Fig. 23).

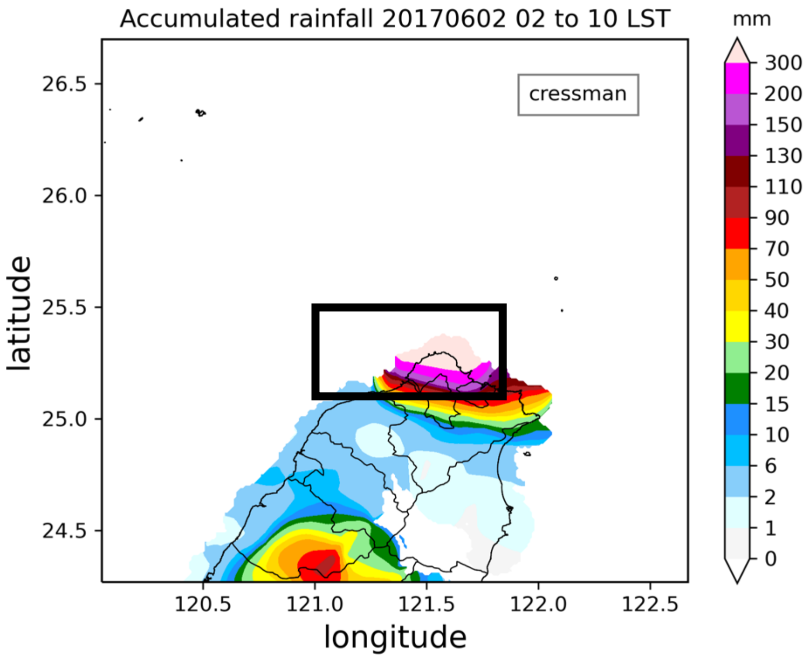

Fig. 21 The observed 8-hr accumulated rainfall from CWB during 1800 UTC 01 June 2017 to 0200 UTC 02 June 2017 which is interpolated by Cressman method with setting minimum neighbors to 3 and radius to 0.15.

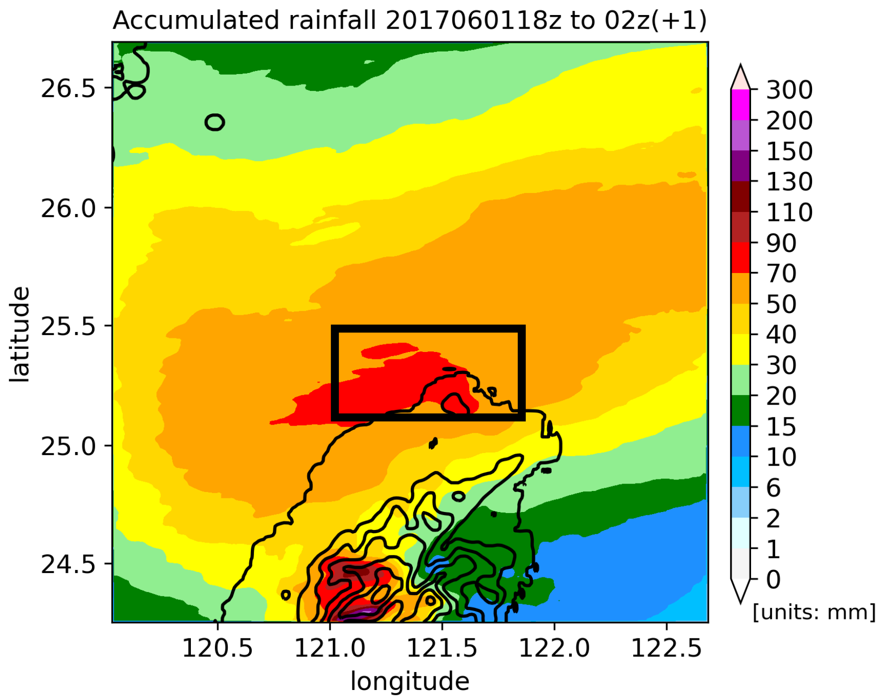

Fig. 22 The 8-hr ensemble mean rainfall during the rainfall period from 1 June 1800 UTC to 2 June 0200 UTC in 2017.

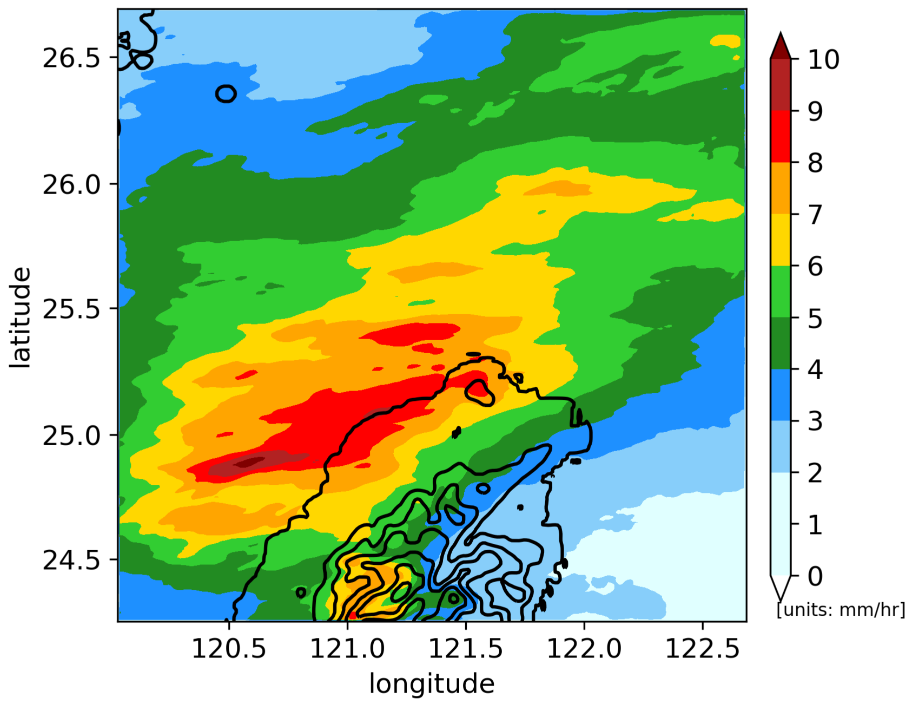

Fig. 23 The 8-hr ensemble spread of rainfall (per hour) during the rainfall period from 1 June 1800 UTC to 2 June 0200 UTC in 2017.

The centroids of K-means clustering (ensemble mean of each group) exhibit different characteristics and locations in the 8-hr rainfall period through the mean and spread; in addition, due to the deviation of heavy rainfall position, the more the accumulated rainfall, the larger the ensemble spread for clusters (Fig. 24, and Fig. 25). With the most members (about 36% of 128 members), cluster 2 has the corresponding distribution to the 128-mean rainfall but with larger values. For cluster 1, the accumulated rain is mainly on the windward side of Central Mountain Range and Snow Mountain. Both cluster 1 and 2 show a separated spread at the northeast of the domain which indicates the frontal system in some members breaks into two parts, with the eastern part moving slowly and the western part moving southward rapidly. The mean rainfall in cluster 3 is stalled at 25.75°N; however, the large spread centers are at 25.5°N and 26°N. Finally, clusters 4 and 5 are further northeastward and westward than cluster 3, indicating that there might be other reasons for these identifiable patterns.

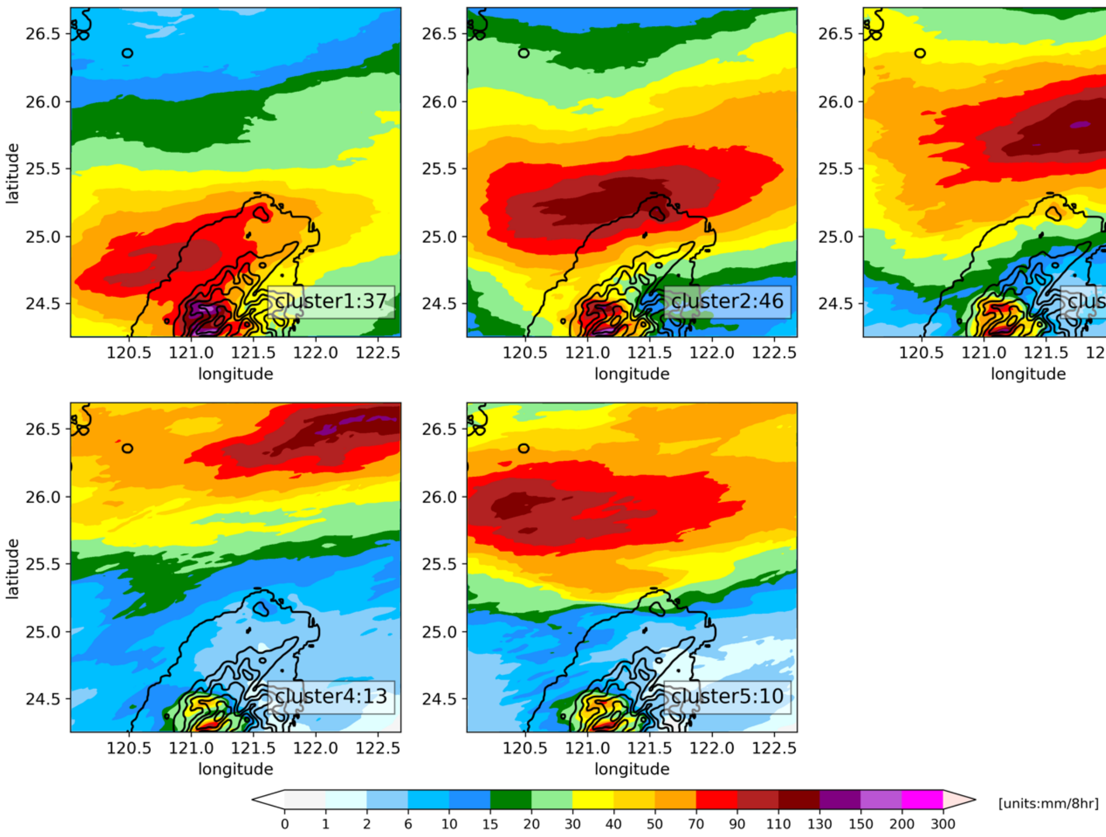

Fig. 24 The 8-hr ensemble mean rainfall of 5 clusters during the rainfall period from 1 June 1800 UTC to 2 June 0200 UTC in 2017, and the boxes indicate the number of members in each cluster.

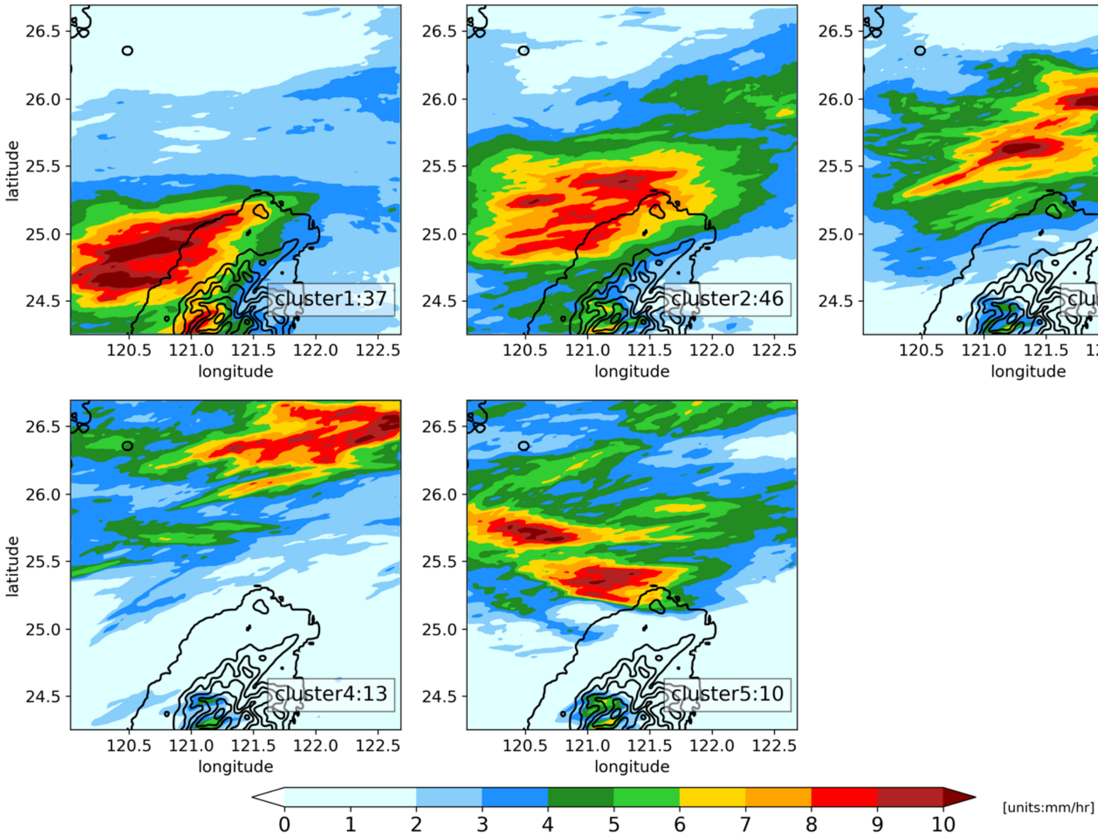

Fig. 25 The 8-hr ensemble spread of 5 cluster rainfall (per hour) during the rainfall period from 1 June 1800 UTC to 2 June 0200 UTC in 2017.

The time evolution of each variable is further discussed in this section (Fig. 26, Fig. 27, Fig. 28, Fig. 29, and Fig. 30). Through the patterns of hourly-cluster rainfall, both cluster 1, cluster 2, cluster 3, and cluster 5 reveal similar southward motion and are correlated to the cyclone north of which. Different from the others, cluster 4 is under the prevailing strong southwesterly wind effect for almost 9 hours. A similar rainfall pattern exists in both 1900 UTC 01 June in cluster 1 and 0000 UTC 02 June in cluster 2 that the rain is mainly accumulated at the northwest coast of Taiwan (Fig. 26) and related to the strongest jet (Fig. 27). However, this similar precipitation result is formed by different wind field structures. Compared to cluster 1, cluster 2 is found a much stronger wind speed from the more powerful easterly wind and slight southerly wind, and an obvious northerly at the post-front, in addition, results in a more wide-spread updraft motion in cluster 2 (Fig. 28, Fig. 29, and Fig. 30).

Far from the terrain, clusters 4 and 5 bring heavy rainfall to the northwest and northeast of Taiwan, and the significant difference between the two is from the strength of the U-wind (Fig. 28). Interacting with a larger U-wind at 1800 UTC, the rainband in cluster 4 can be pushed further northwestern with time. In contrast to cluster 4, cluster 5 rainfall remains further west because of the weaker U-wind contribution and induces west which moves southward earlier than the fourth cluster. The phenomenon also corresponds to the statistic of frontal horizontal tilt that cluster 5 has the most tilted frontal pattern among all clusters (not shown).

The convergence zone enhances the wind speed at both pre- and post-frontal regions, the terrain blocking effect, and also the secondary circulation, and brings a notable 5-km vertical motion (about 2100 UTC to 0000 UTC) (Fig. 30). Among all clusters, cluster 3 has the most accumulated hourly cluster-mean rainfall at 2200 UTC. The strong meridional wind across the Mei-Yu front and horizontal wind shear strengthens the low-level convergence and induces severe updrafts, resulting in the heavy rainfall duration.

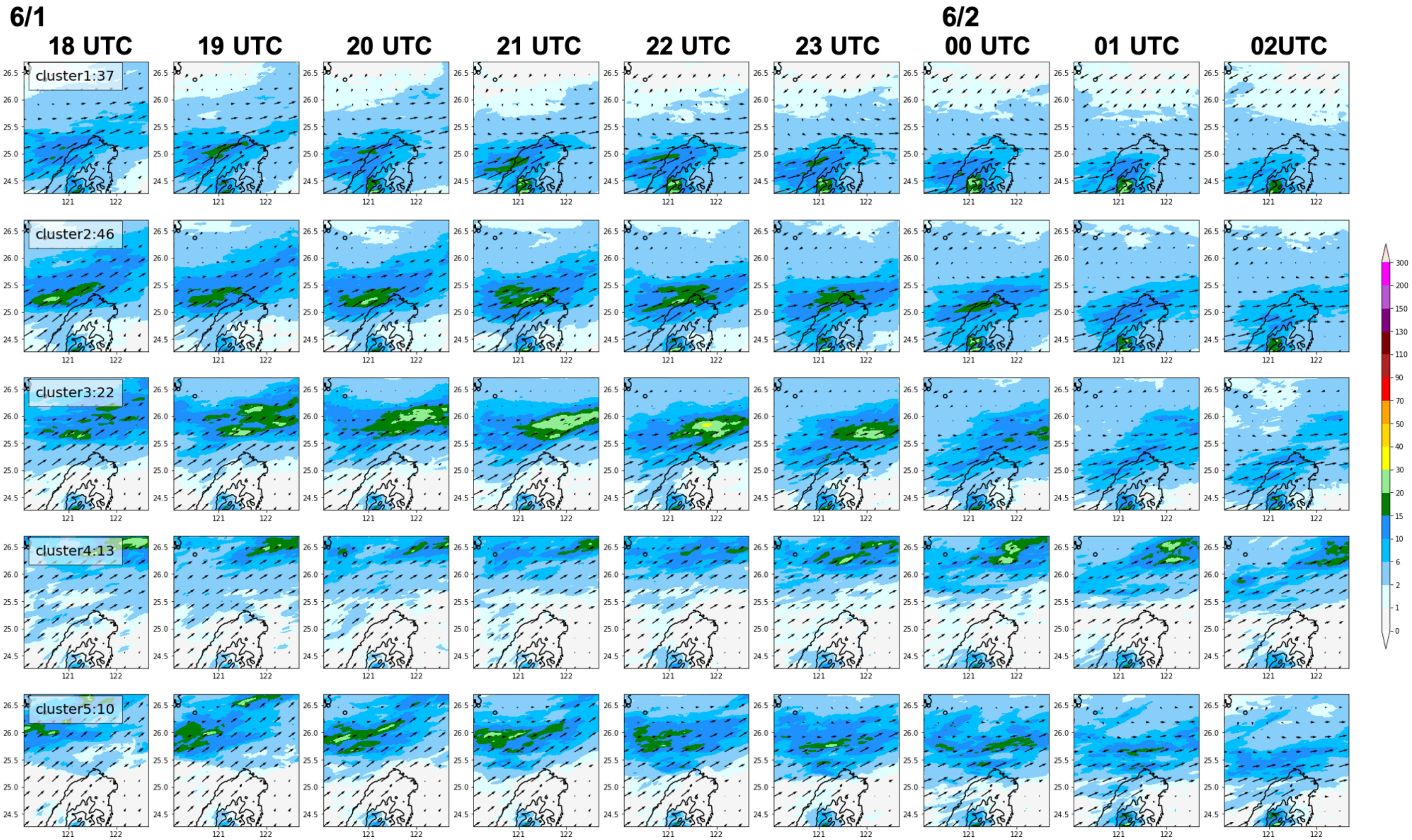

Fig. 26 Time series of 5-cluster accumulated rainfall (shaded; unit: mm/hr) and 1-km wind (vector) from 1800 UTC 01 June 2017 to 0200 UTC 02 June 2017.

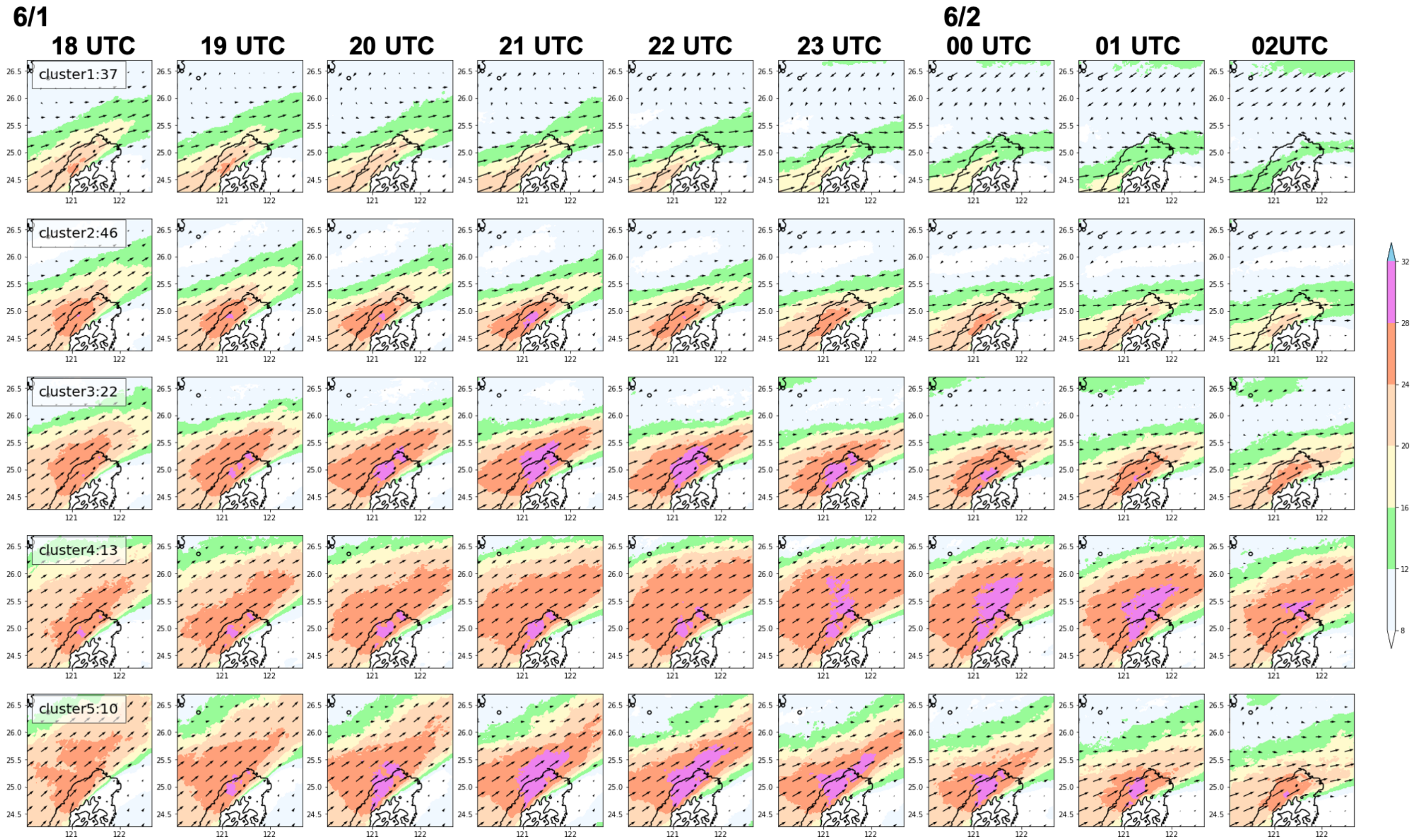

Fig. 27 Time series of 5-cluster 1-km wind speed (shaded; unit: m/s) and 1-km wind (vector) from 1800 UTC 01 June 2017 to 0200 UTC 02 June 2017.

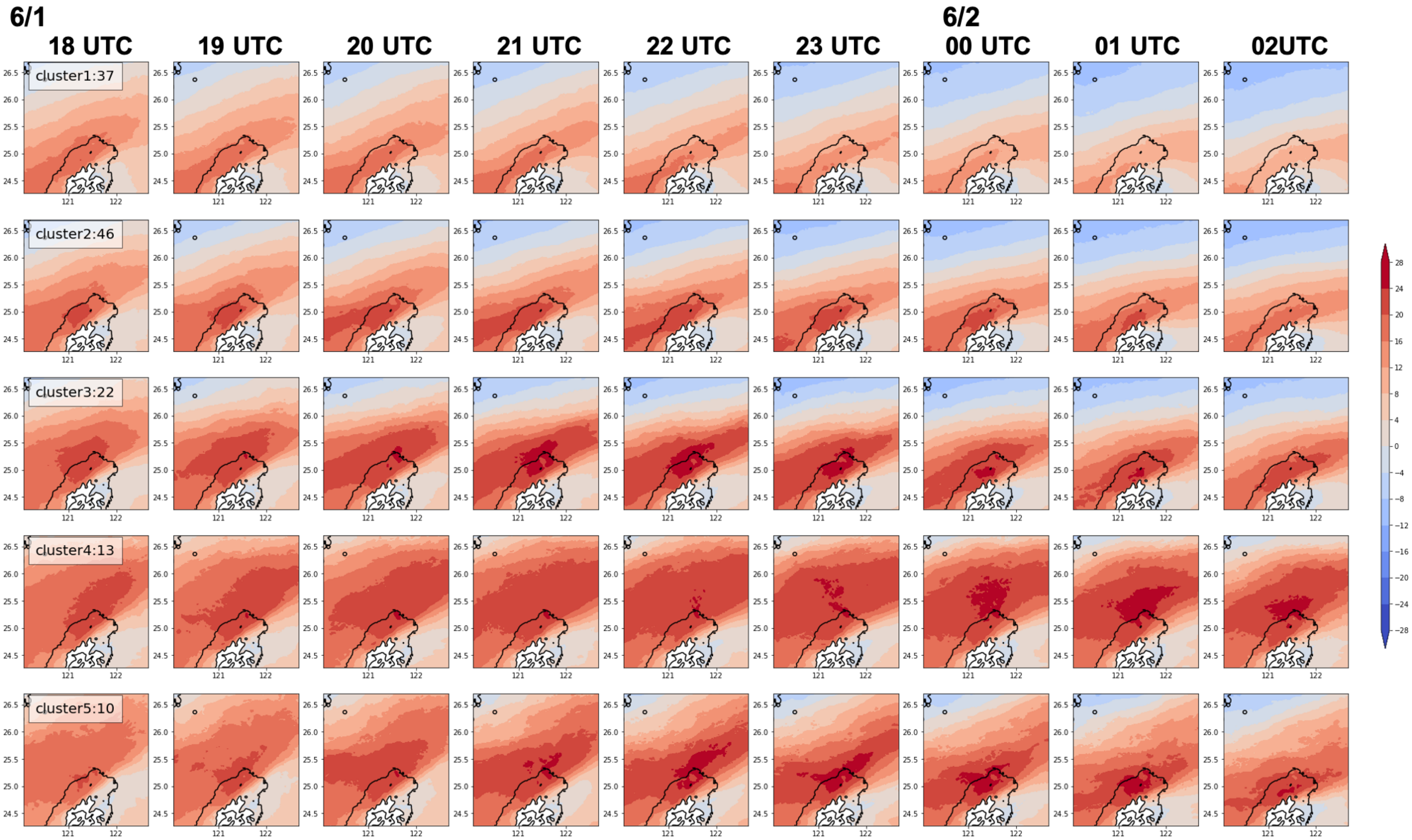

Fig. 28 Time series of 5-cluster 1-km zonal wind speed (shaded; unit: m/s) from 1800 UTC 01 June 2017 to 0200 UTC 02 June 2017.

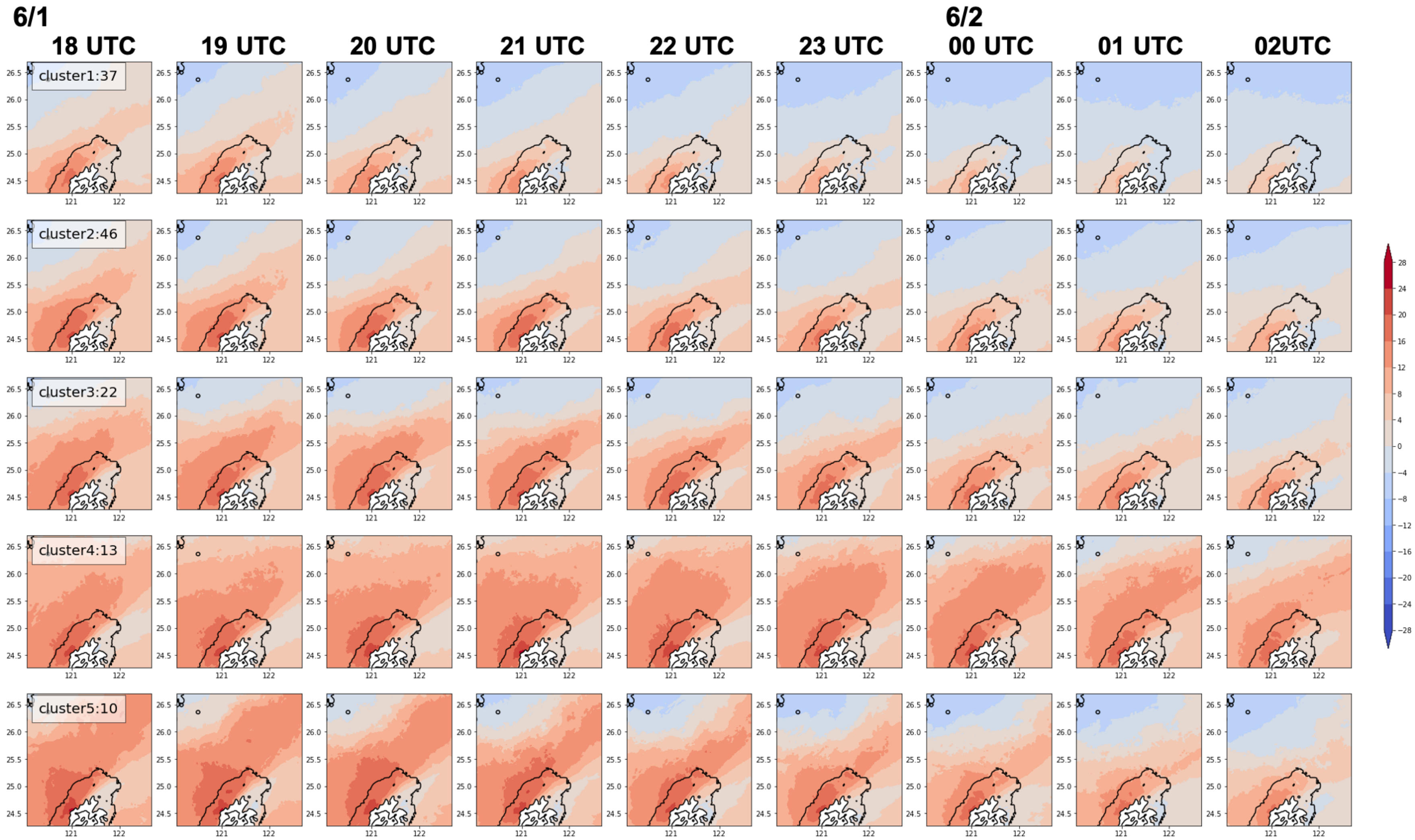

Fig. 29 Time series of 5-cluster 1-km meridional wind speed (shaded; unit: m/s) from 1800 UTC 01 June 2017 to 0200 UTC 02 June 2017.

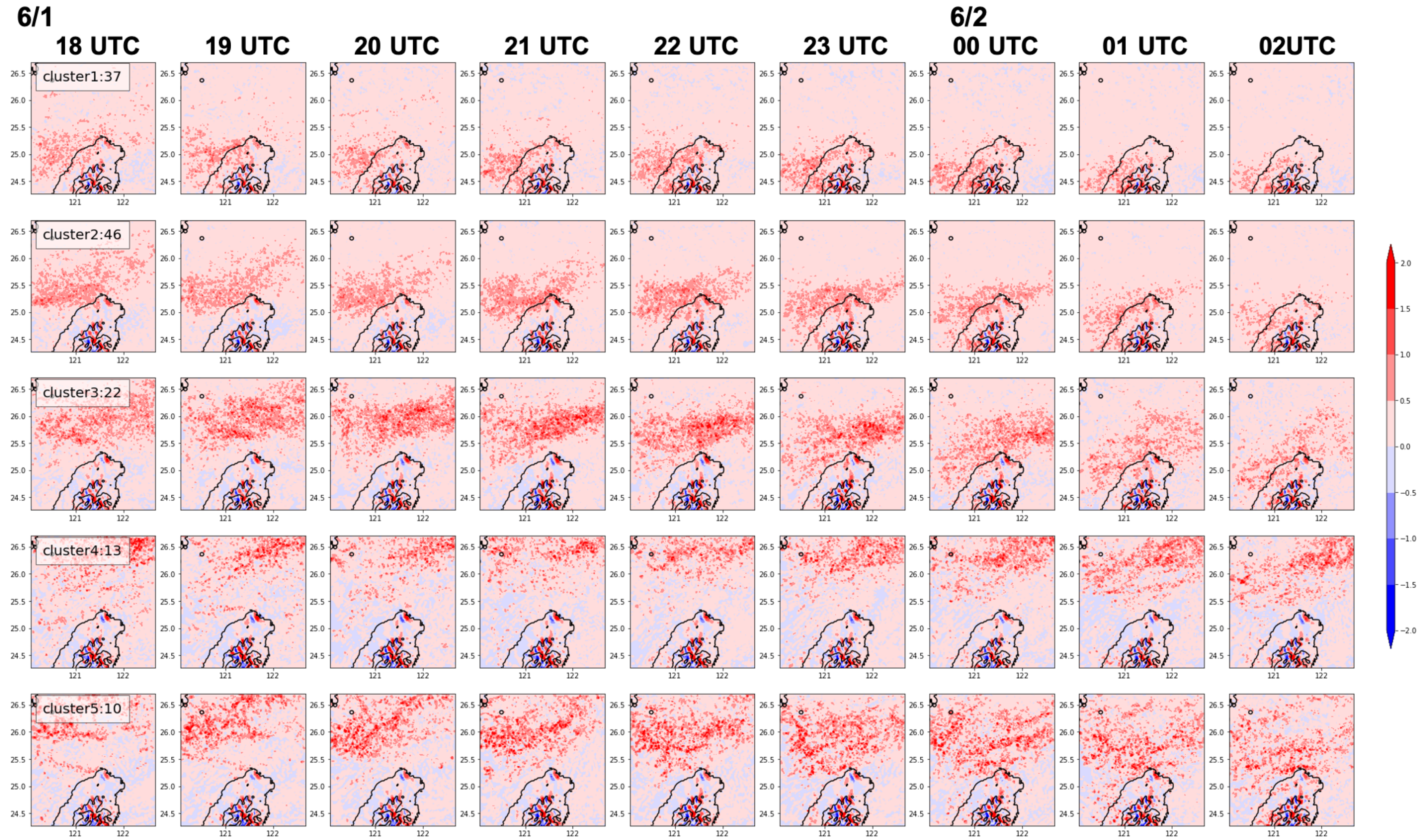

Fig. 30 Time series of 5-cluster 5-km vertical velocity (shaded; unit: m/s) from 1800 UTC 01 June 2017 to 0200 UTC 02 June 2017.

To understand the horizontal distribution of rainfall in each cluster member, a particular region with extreme observed rainfall is chosen for further calculations. In Table 2, the percentages indicate the proportion of members in clusters that reach the threshold. Among all 5 clusters, cluster 2 shows the highest value and has the most similar pattern to the observation as the 8-hr accumulated rainfall pattern in Fig. 21, and Fig. 24. Through analyzing other dynamic performances (Table 3), with better simulated frontal position, the rainband center and low-level convergence of cluster 2 reveal the largest similarity to the truth. The stronger simulated V-wind enhances the larger statistical frontal axis with more NW-SW orientation (not shown). The strength and range of barrier jet are also similar to the retrieved wind field. Statistically, the performances of the ensemble clusters would be correlated to the Gaussian-based initial perturbations by 3DVAR CV3; therefore, cluster 2 is the one that displays the closest to the mean pattern of 128 ensemble members.

Threshold \ Cluster	Cluster 1	Cluster 2	Cluster 3	Cluster 4	Cluster 5
8-hr rainfall > 100mm	56.76%	95.65%	72.73%	0.00%	30.00%
8-hr rainfall > 100mm and grids > ¼ of box	27.03%	78.26%	18.18%	0.00%	30.00%
8-hr rainfall > 200mm	16.22%	63.04%	13.64%	0.00%	30.00%

Table 2 The rainfall performance of 5 clusters with 3 different extreme rainfall thresholds. The rainfall values are chosen the grids in Fig. 21 and Fig. 22 boxes.

	Obs/ WISSDOM	cluster1	cluster2	cluster3	cluster4	cluster5
Rainband center	25.3°N	24.8°N	25.2°N	25.8°N	26.5°N	26.0°N
Frontal position	25.3°N	25.1°N	25.3°N	25.8°N	26.2°N	26.0°N
Convergence field (1.5km)	25.4°N	24.7°N	25.3°N	25.8°N	26.4°N	26.0°N
Vertical velocity(W)	25.4°N	24.7°N	25.3°N	25.8°N	26.3°N	26.0°N
Mean zonal wind (U)	22.1m/s	16.9m/s	23.0m/s	24.8m/s	25.5m/s	23.0m/s
Mean meridional wind (V)	15.1m/s	13.6m/s	20.0m/s	20.6m/s	22.9m/s	22.2m/s
Mean frontal axis	5°	11°	12°	10°	12°	19°
Barrier jet speed	25.7m/s	17.9m/s	27.2m/s	28.3m/s	29.7m/s	28.5m/s
Grids points of Barrier Jet > 12.5m/s	25192 grids	6257 grids	21210 grids	30431 grids	50075 grids	35898 grids

Table 3 The comparison between WISSDOM and observation to 5 ensemble clusters by several dynamic patterns, such as rainband position, frontal position and axis, wind field performance.

To investigate the cluster difference at both the pre-frontal and heavy rainfall periods, the 850-hPa cluster-mean anomaly wind and cluster-mean relative vorticity from D03 are utilized (Fig. 31, Fig. 32, Fig. 33, and Fig. 34). During the pre-frontal period, all clusters are under prevailing southwesterly wind with a vortex (wind shear line) in the north of Taiwan (Fig. 31). On the lee side of Taiwan terrain, there is also a lee trough in eastern Taiwan because of the detour flow, and supports the previous studies (Li and Chen, 1998; Yeh and Chen, 2003; Tu, 2014). For western Taiwan, in response to the orographic blocking effect, the wind speed decreases on the windward side and accelerates in the downwind region, resulting in the formation of a barrier jet. In comparison, cluster 5 has the weakest wind speed at the source region of prevailing wind; in addition, the wind is mainly contributed by the meridional component (Fig. 33). With similar meridional wind strength to cluster 5, cluster 4 shows the most powerful dynamic condition in the southwestern region among all clusters which indicates that the pre-storm wind may be a reason of the cluster-mean rainband locations. At the heavy rainfall stage (Fig. 32), the difference in clusters becomes visible. The frontal systems, defined by wind shear line and relative vorticity, are at different positions and result in the different areas of pre-frontal strong wind. The wind shear lines of meridional wind in each cluster correspond to the accumulated rainfall (Fig. 24, and Fig. 34).

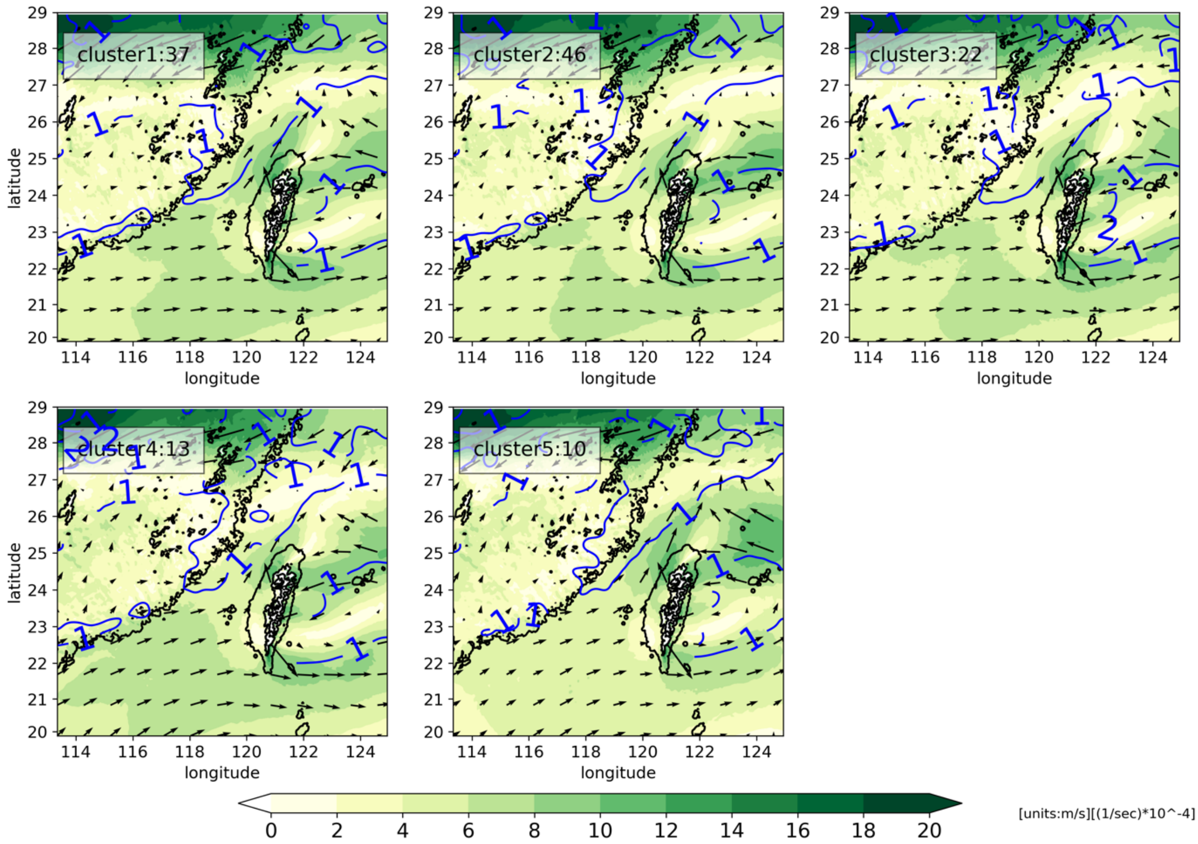

Fig. 31 The 850-hPa mean anomaly wind (shaded; vector) and mean relative vorticity (blue contour, interval is 1×10-4) of 5 clusters during 12-hr pre-frontal rainfall period (from 0500 UTC 01 June to 0700 UTC 01 June).

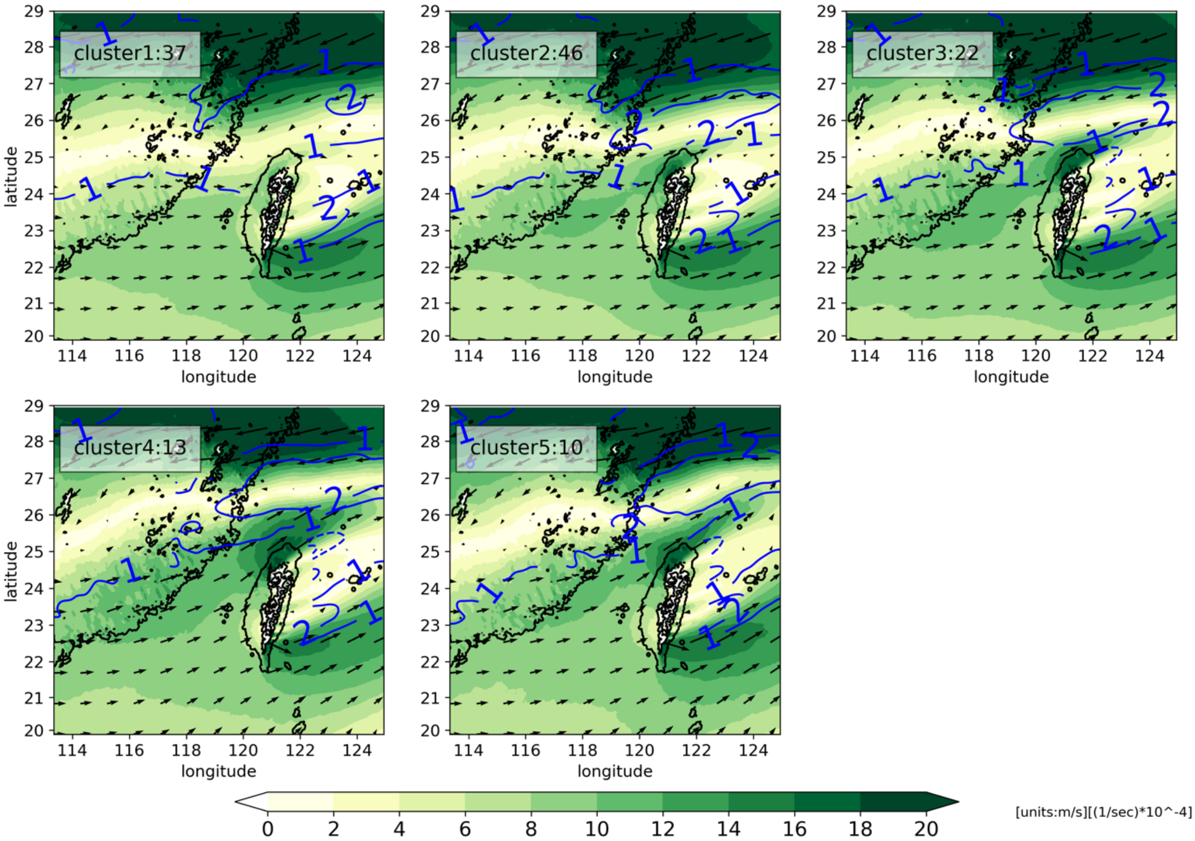

Fig. 32 Same as Fig. 31, but during 8-hr heavy rainfall period (from 1800 UTC 01 June to 0200 UTC 02 June).

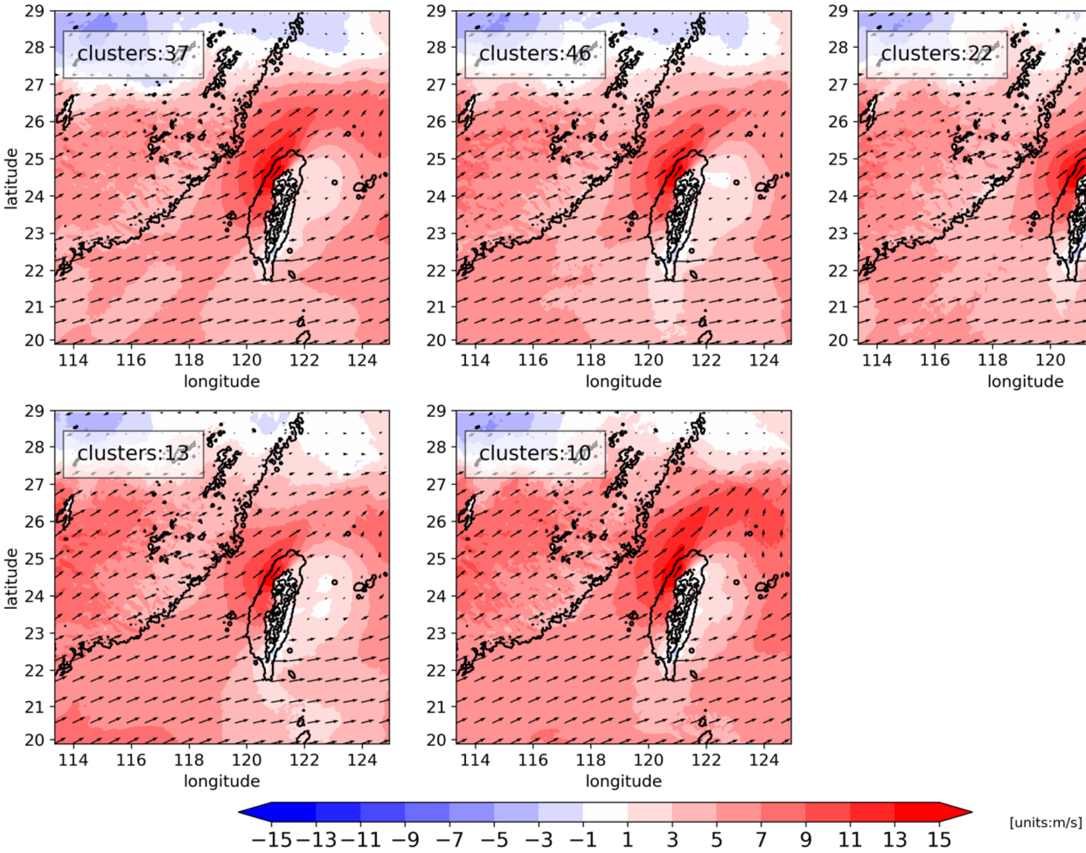

Fig. 33 The 850-hPa mean anomaly meridional wind (shaded) and mean anomaly meridional wind (vector) of 5 clusters during 12-hr pre-frontal rainfall period (from 0500 UTC 01 June to 0700 UTC 01 June).

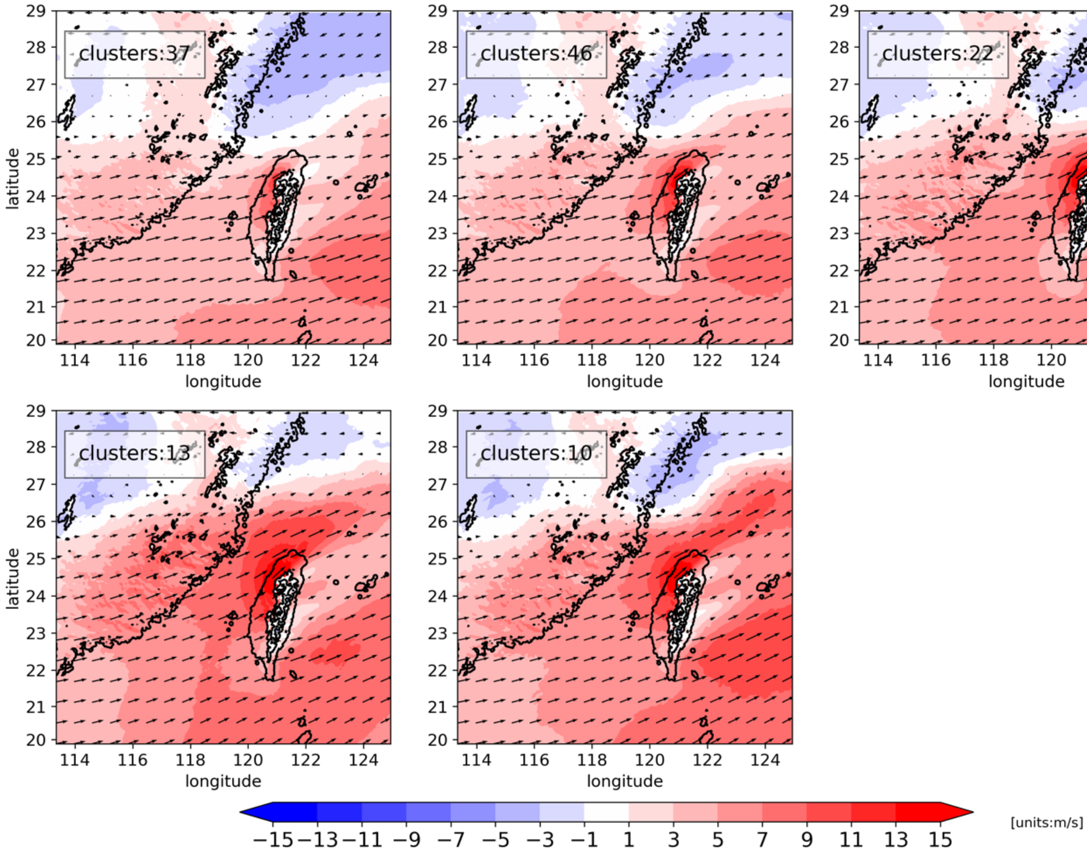

Fig. 34 Same as Fig. 33, but during 8-hr heavy rainfall period (from 1800 UTC 01 June to 0200 UTC 02 June).

Apart from the dynamic contribution of southwesterly wind, moisture and temperature from the warm southern area are also key factors of "heavy" rainfall. Therefore, in Fig. 35, five mean equivalent potential temperature patterns are shown. Taiwan is beneath the high equivalent potential temperature (over 350 K) axes, indicating an unstable environment occurs in each group.

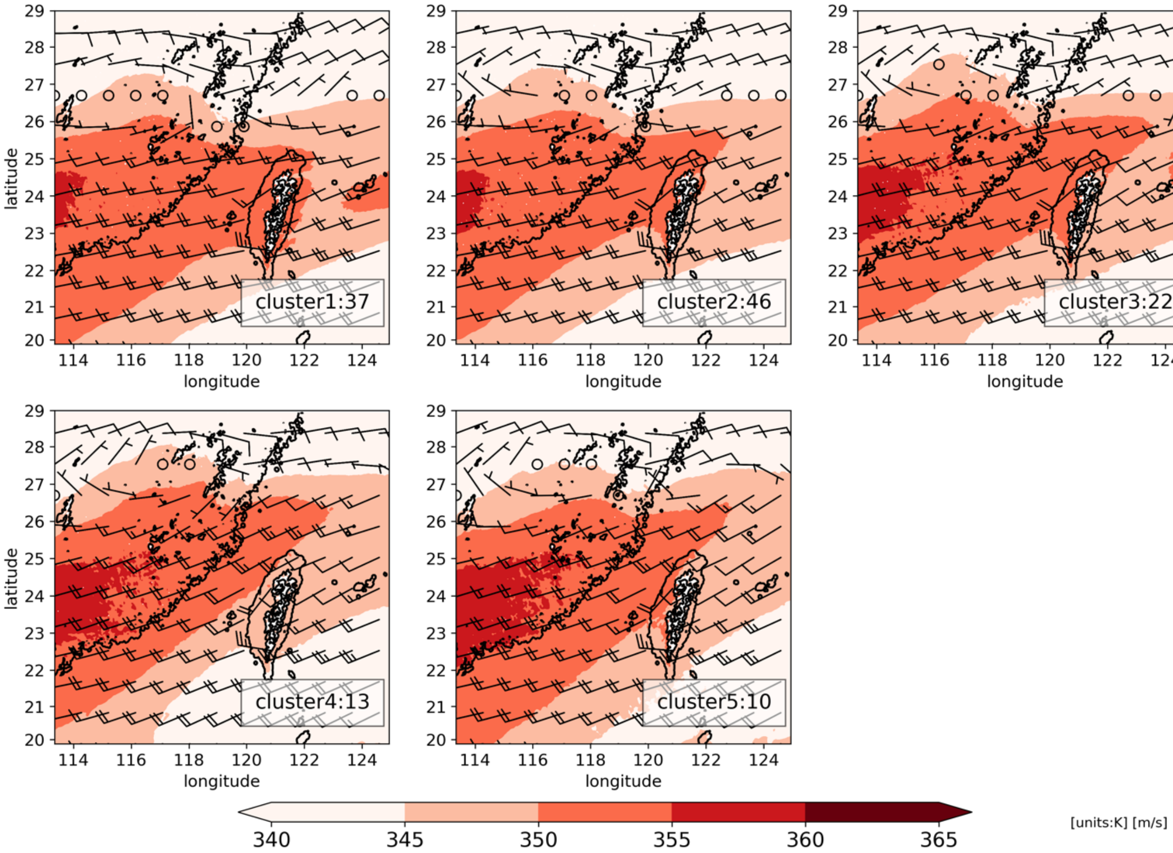

Fig. 35 Mean equivalent potential temperature (shaded) and 850-hPa mean wind (barb) during rainfall period in each K-means cluster.

In Fig. 36, the 500-hPa pressure anomaly during the 8-hr heavy rainfall period (from 1800 UTC 1 June 2017 to 0200 UTC 2 June 2017) is obtained from the pressure error between the ensemble mean and 5 clusters that the positive value reveals an anomaly high pressure. The 850-hPa wind anomaly is also from the difference between both, with the larger the vector, the wider the variation. In cluster 1, the pressure anomaly pattern appears an inverse at east and west of Taiwan, while the anomaly high is inside China and the low is over the ocean. In response to this structure, a stronger northeasterly wind forms in the end and forces the system to move southward to central Taiwan. In contrast, cluster 4 exhibits an opposite structure to cluster 1 and results in an even stronger southwesterly flow than the mean state. Therefore, the northernmost cluster forms. Between the characteristic of these two extreme patterns, cluster 2, similar to cluster 1, presents an anomaly east-northerly but ends north of Taiwan due to the anomaly high north of Taiwan, and cluster 3 with an anomaly weaker low at south produces a weaker southwesterly the fourth cluster. Although the wind anomalies display a strong correlation between clusters 4 and 5, the anomaly wind direction increases with latitude and ends up with a westerly anomaly. The primary reason for the rotation is a strong pressure anomaly on the western coast of China. Overall, the pressure pattern and wind field are strongly related to the frontal position.

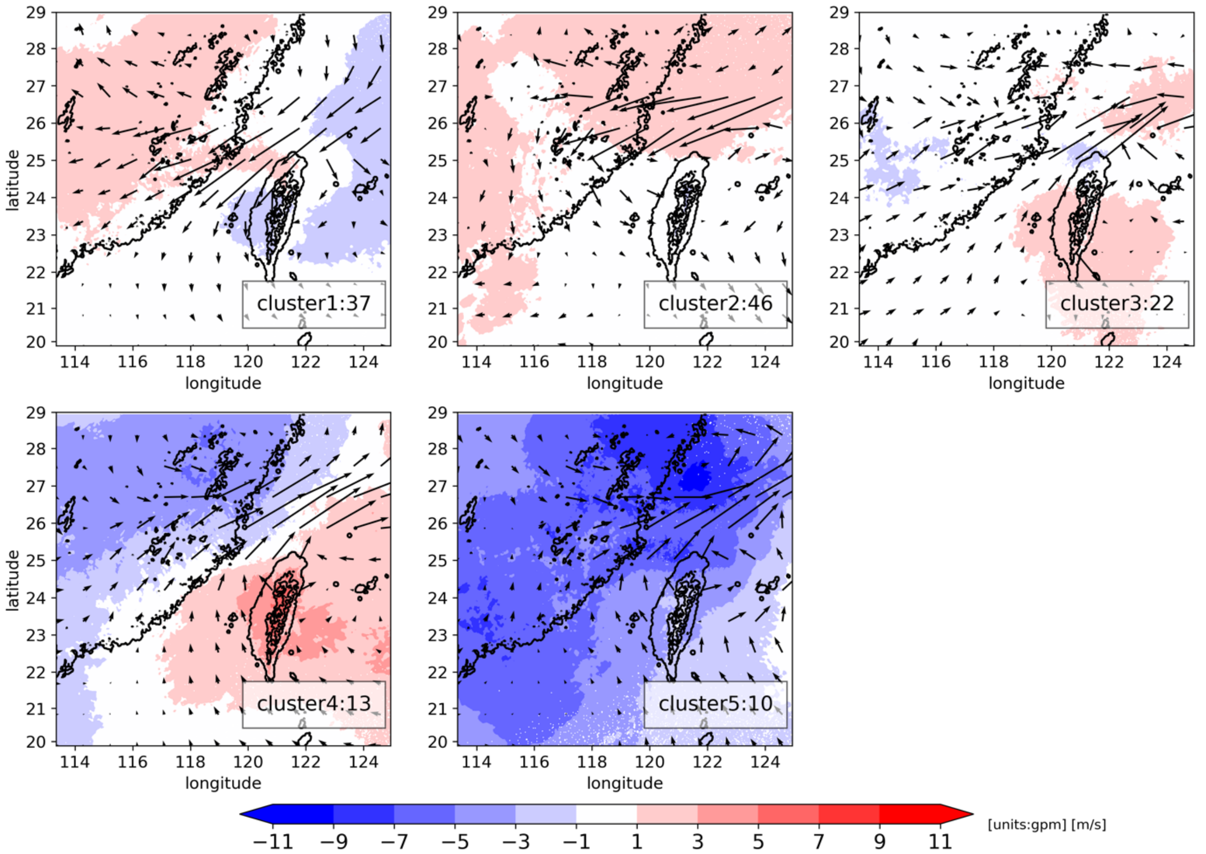

Fig. 36 500-hPa pressure anomaly (shaded) and 850-hPa anomaly wind (vector) during rainfall period in each K-means cluster from 1800 UTC 1 June 2017 to 0200 UTC 2 June 2017.

5.2 Dynamic characteristic of clustering result

5.2.1 Pressure gradient effect

Through previous studies, a pressure ridge at the windward side of the southwesterly wind was found in both model simulations and observations, such as sounding, aircraft, ground-based observations (Chen, 1995b; Li et al., 1997, Yeh and Chen, 2003) and was in response to the split prevailing onshore airflow. In the sub-synoptic scale, with the opposite pressure pattern at southeast of Taiwan (west Pacific subtropical high) and northwest of Taiwan (trough from China), the MBLJ blows perpendicular to the pressure gradient due to geostrophic effect (Fig. 37). With the windward ridge developing by terrain blocking and the frontal cyclone or low-level trough moving southeastward, the pressure gradient at the west of Taiwan increases dramatically and induces a powerful BJ that parallel to terrain locally and the dominated term is the inertial advection term (Yeh & Chen, 2003). As the BJ and the northerly encounters at northern Taiwan, the strong convergence would then form and affect the local rainfall pattern.

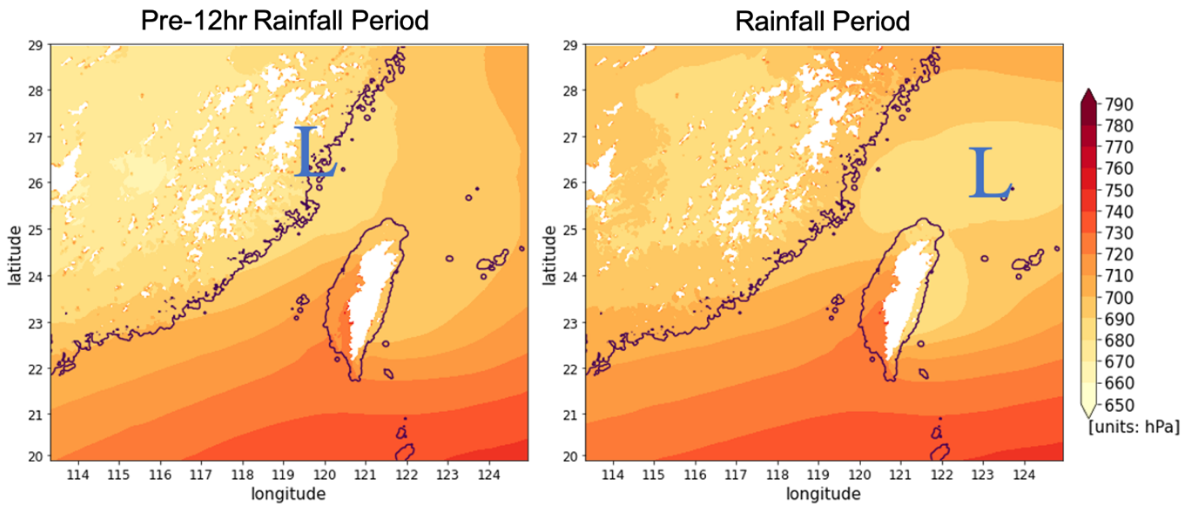

Fig. 37 The mean 925-hPa geopotential height pattern (shaded, unit: gpm) of the pressure gradient effect at pre-12hr rainfall period (from 0500 UTC 01 June to 0700 UTC 01 June) and rainfall period (from 1800 UTC 01 June to 0200 UTC 02 June).

In Fig. 38, the evolution of the mean 850-hPa geopotential height is shown. The position of the low-level trough at 1200 UTC and 1800 UTC on 1 June reveals a strong connection between the rainband position and the movement of the low-level trough. For the initial time (0000 UTC 1 June), there is a slight difference in pressure patterns which increases northward between clusters (Fig. 39). After time passes, a result shows that the faster the movement of the low, the more south the accumulated rainfall pattern during 1800 UTC 1 June to 0200 UTC 2 June. Cluster 4, with a stronger Pacific subtropical High in southern Taiwan and the slowest short-wave trough, produces an even norther pressure gradient force than others and results in the farthest rainband among all clusters. Although the trough in cluster 5 reveals a similar position to clusters 1, 2, and 3, the rainfall is located near the southeastern coast of China and is in response to the deeper trough. As a result, a stronger pressure gradient in a north-northeast-south-southwest direction toward the trough is triggered. Compared to the reanalysis data, the position of the short-wave trough validates why cluster 2 has the closest performance to the truth (Fig. 40).

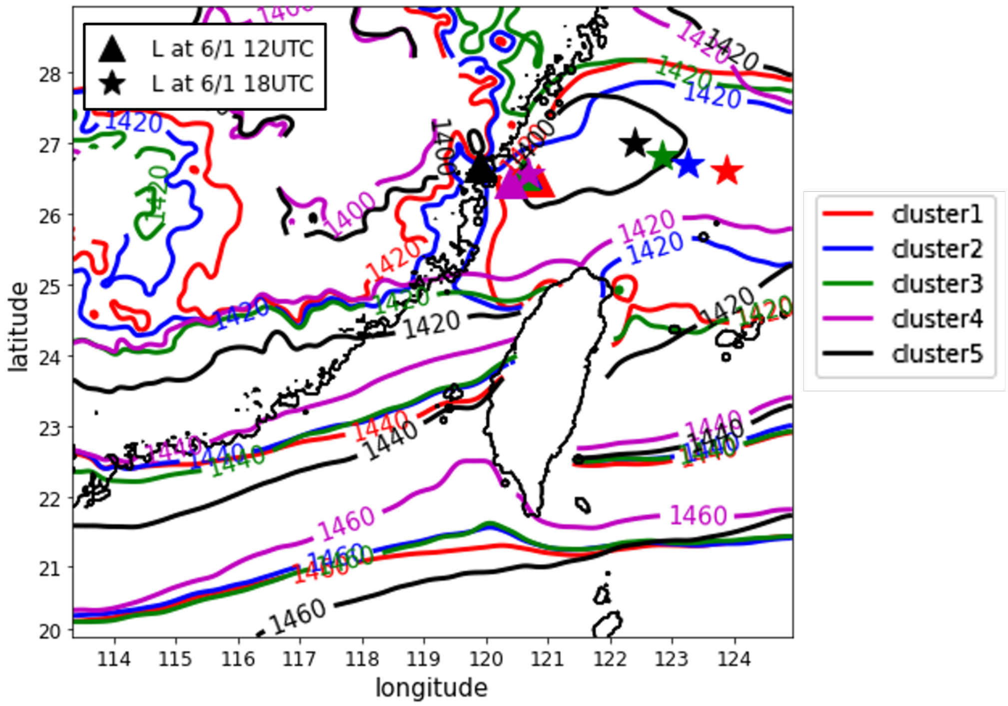

Fig. 38 The contour lines reveal the averaged 850-hPa geopotential height (contour, unit: gpm) in each cluster, with cluster 1 in red, cluster 2 in blue, cluster 3 in green, cluster 4 in purple and cluster 5 in black. The triangle sign indicates the trough center at 1200 UTC 1 June 2017, while the star sign indicates at 1800 UTC 1 June 2017.

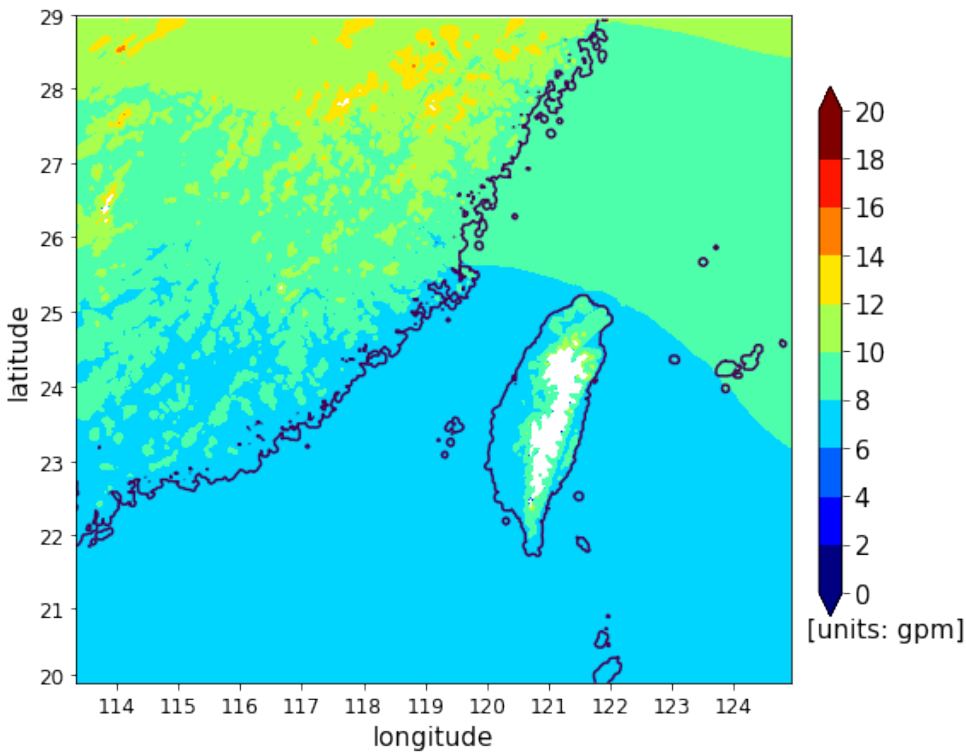

Fig. 39 The standard deviation of 850-hPa geopotential height (shaded, unit: gpm) at model initial time (0000 UTC 1 June).

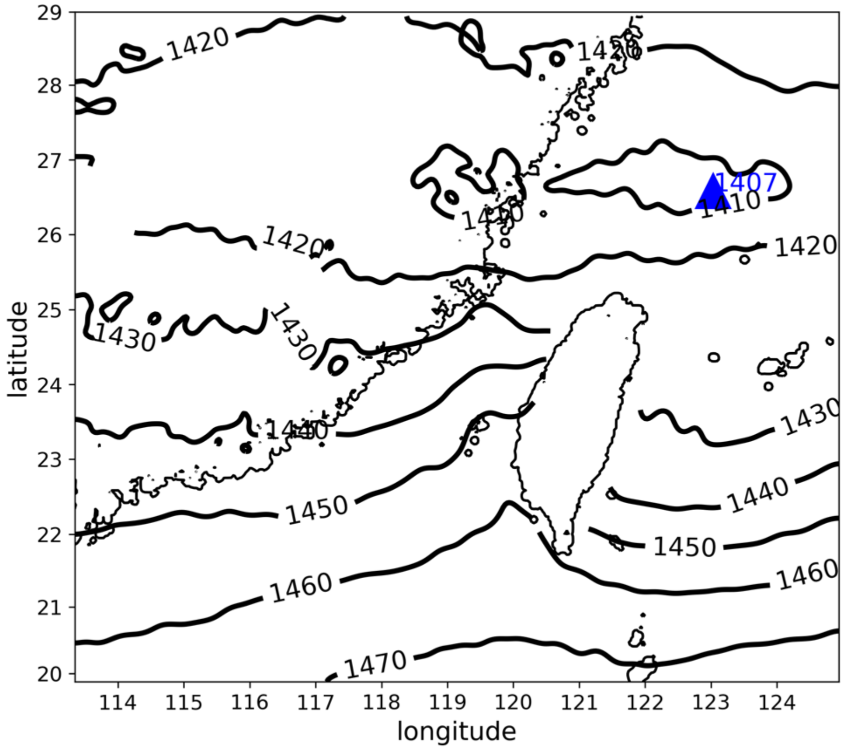

Fig. 40 The National Centers for Environmental Prediction (NCEP) (0.25 x 0.25) Final operational global analysis (FNL) 850-hPa geopotential height data at 1800 UTC 1 June 2017. The blue triangle indicates the center of short-wave trough.

In Fig. 41 and Fig. 42, there shows the short-wave trough eastward movements and hourly rainfall patterns at both 850hPa and 925hPa from 1200 UTC to 2000 UTC 01 June 2017 with an interval of 2 hours. With the fast-moving trough as in cluster 1, the rainband reaches Taiwan at 1400 UTC; in contrast, the slow-moving troughs in cluster 2,3, and 4 correspond to the large increments of rain rate at 1800UTC and 2000 UTC. Further, this reveals that the rainband is related not only the movement of the trough but also the strength and position of the low. Through the two best performance clusters, cluster 2 and cluster 3, the maxima hourly rainfall occurs when the 850hPa trough is located at northeastern Taiwan and the 925hPa trough is located at northwestern Taiwan which echo the results in Wang et al. (2021) that the rainfall is sensitive to the frontal position and movement and the mesoscale low-level low.

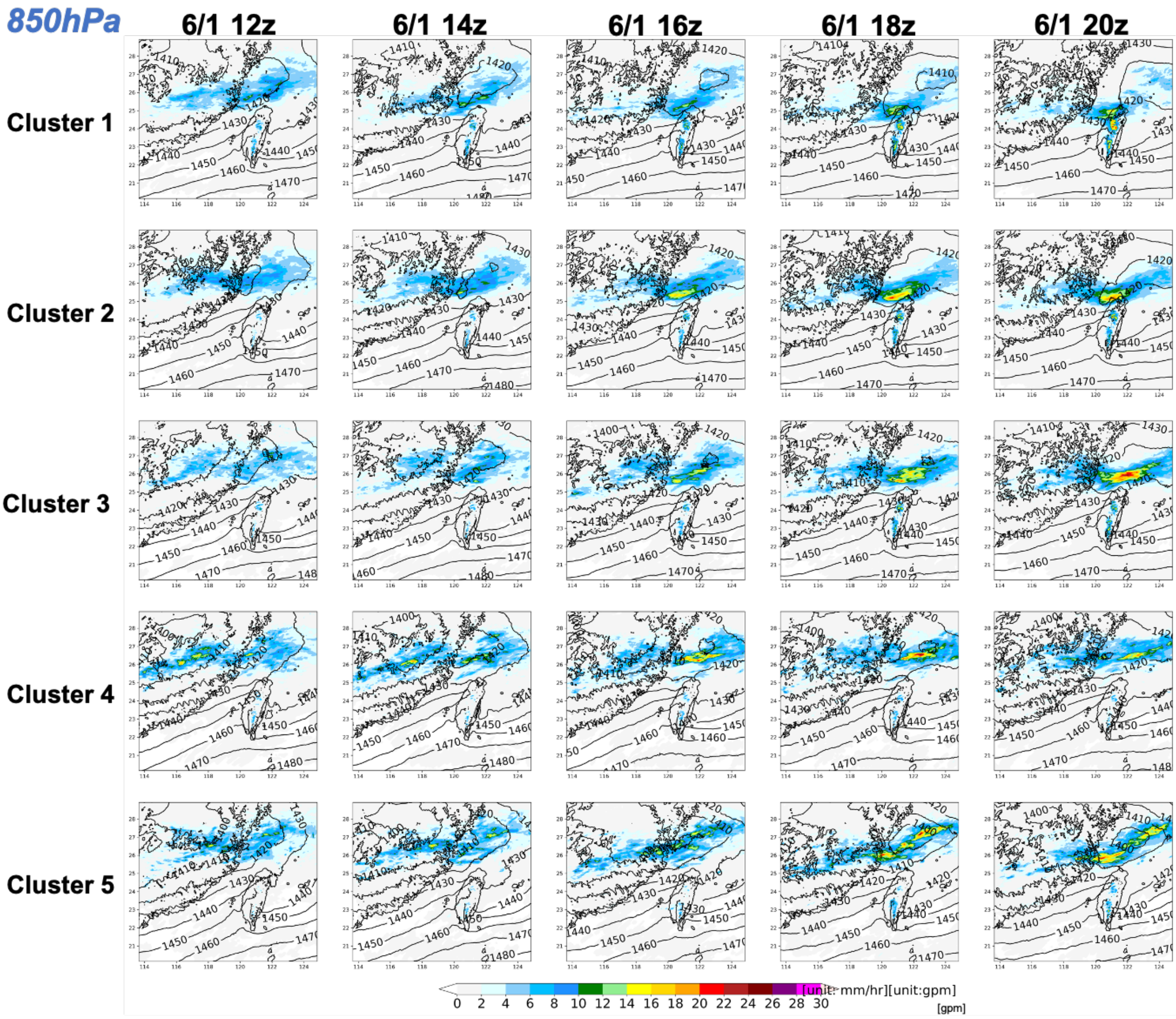

Fig. 41 The simulated clustered hourly rainfall pattern (shaded, unit: mm/hr) and geopotential height (contour, unit: gpm, interval is 10 gpm) at 850hPa from 1200 UTC to 2000 UTC 01 June 2017.

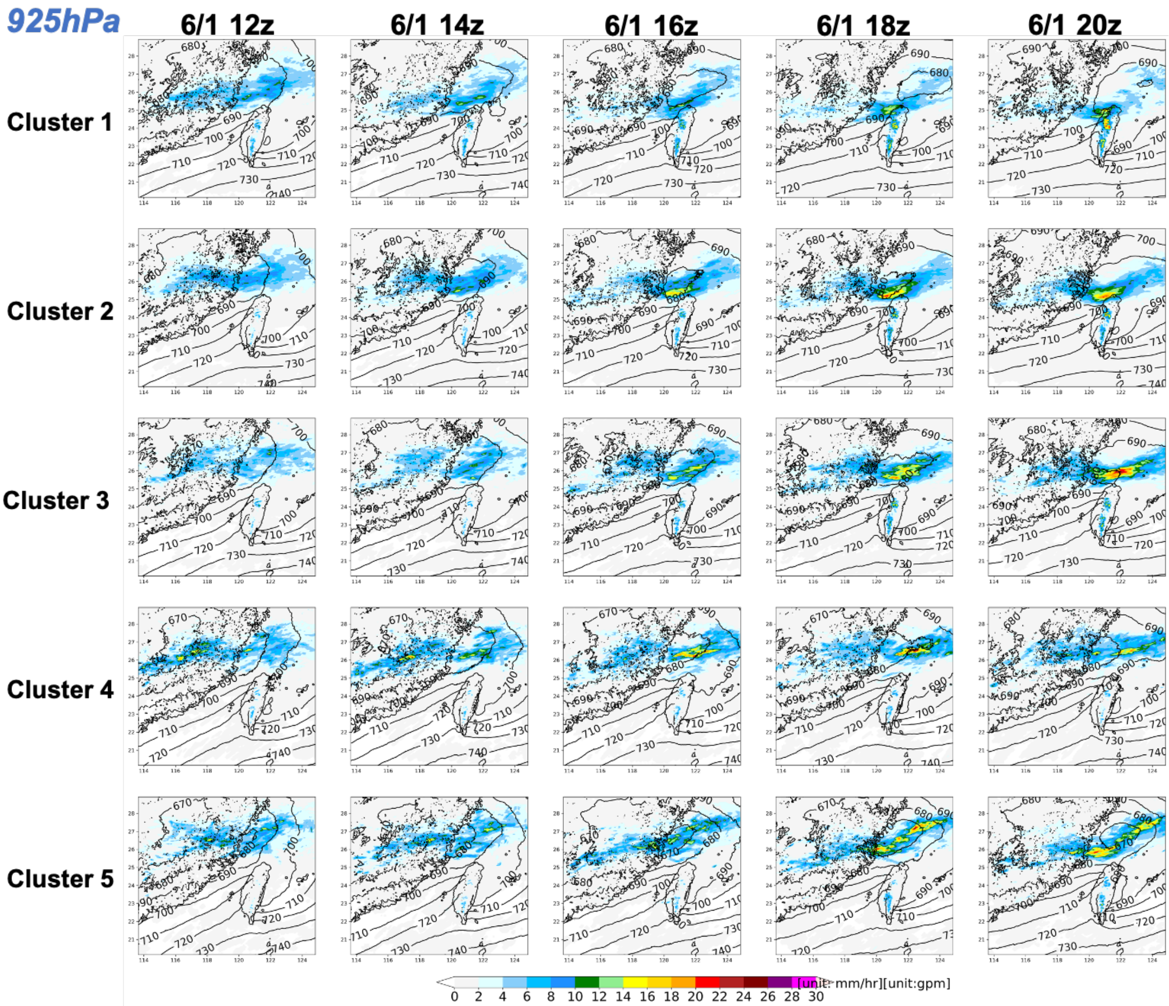

Fig. 42 Same with Fig. 41, but for the geopotential height at 925hPa (contour, unit: gpm, interval is 10 gpm).

5.2.2 The performance of cluster-averaged wind

To further understand the change under the development of short-wave trough and the strength of convergence, the hodographs of barrier jet domain (BJ domain, red box), northeastern domain (NE domain, blue box), and southwestern domain (SW domain, black box) are displayed (Fig. 43, Fig. 44, Fig. 45). According to the extreme value of simulated wind along cross-sections in boxes, the 1-km maximum wind in the BJ domain and the 925-hPa mean wind in the NE domain and SW domain of five cluster-averaged wind patterns are selected for the hodograph analysis.

For the BJ domain, the prevailing southwesterly flow dominates the Taiwan Strait at first. Due to an increment in speed in southwestern Taiwan (Fig. 43b), the wind speed at the north edge of the Snow Mountains keeps increasing with a slight change of direction. After 1000 UTC, five wind patterns start to be controlled by the passage of a low-level trough and the wind shear line moving toward Taiwan, leading to the zonal wind component accretion. When the wind shear line reaches northern Taiwan, more members would be affected by the post-frontal wind, resulting in a meridional wind reduction in each cluster.

(a)

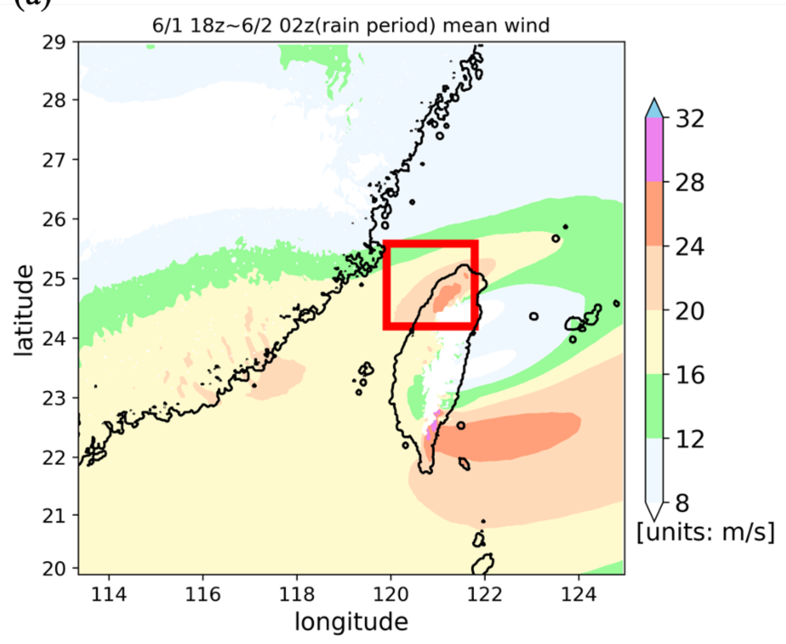

(b) Max 1km U,V wind at BJ domain

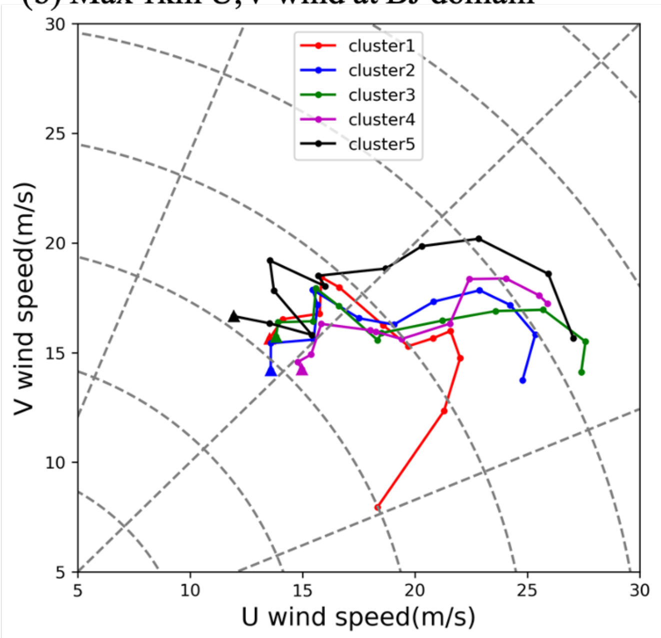

Fig. 43 (a) The simulated mean 1-km wind speed during rainfall period (1800 UTC 1 June to 0200 UTC 2 June) and the red box is the barrier jet domain (BJ domain). (b) The cluster-averaged hodograph of simulated 1-km max wind in the BJ domain from 0200 UTC 1 June to 0000 UTC 2 June (dots, interval is 2 hours) with the first time (0200 UTC 1 June) marked in triangle.

During the frontal oscillated period, the heavy rainfall is dependent on the strength of convection, regarded as the contribution of both northerly and southerly wind. Therefore, the origin of the wind, the NE domain, and the SW domain, are set and further discussed (Fig. 44a, and Fig. 45a). Because the frontal system is still far from Taiwan, the prefrontal southwesterly wind prevails in the NE domain (Fig. 44b). When the front keeps propagating southward, the meridional wind speed decreases faster than the zonal wind and increases inversely after the shear line passes. Nevertheless, the wind shear that goes through this NE domain whose strength is much weaker than that near Taiwan (BJ domain) with a much weaker zonal performance.

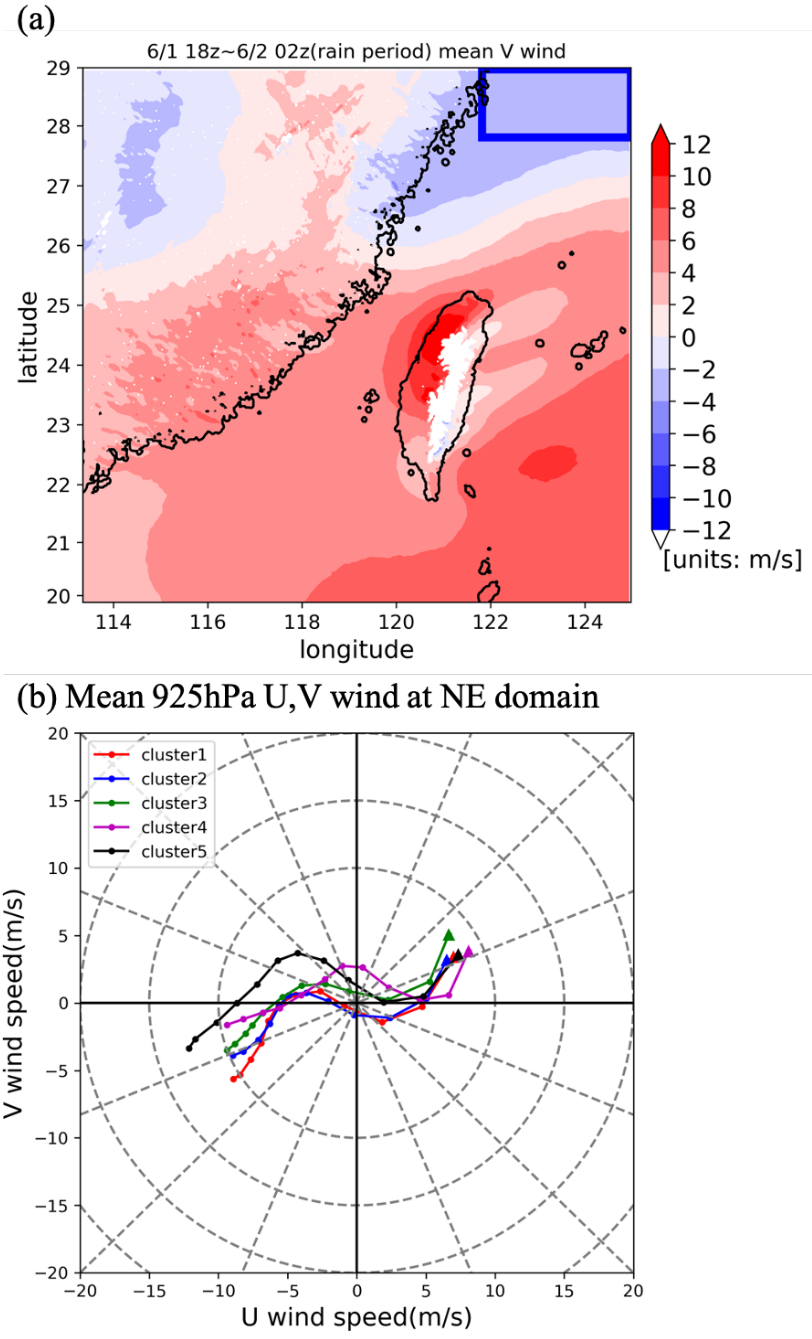

Fig. 44 (a) The simulated mean 925-hPa meridional wind speed during rainfall period (1800 UTC 1 June to 0200 UTC 2 June) and the blue box is the northeastern domain (NE domain). (b) The cluster-averaged hodograph of simulated 925-hPa mean wind in the NE domain from 0200 UTC 1 June to 0000 UTC 2 June (dots, interval is 2 hours) with the first time (0200 UTC 1 June) marked in triangle.

For the source region of southwesterly wind, SW domain, the winds of 5 clusters strengthen to over 15 m/s before 0800 UTC and turn counterclockwise consistently. At about 1800 UTC, all clusters reach their maximum meridional wind when the short-wave trough is offshore from China and reorganized in the north of Taiwan. After the trough keeps moving eastward, the pressure gradient effect reduces and results in the weakness of the V-wind which is much weaker than the prefrontal period but with an even stronger value in zonal axis. As a result, the increment of northeasterly flow in the north and the decrement of V-wind in the south promote the southward propagating frontal system after the analysis period.

(a)

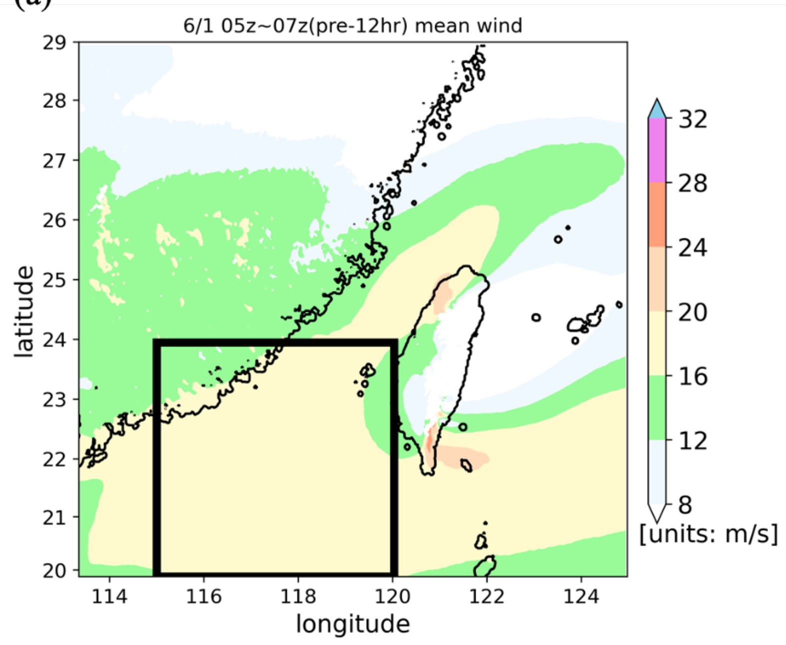

(b) Mean 925hPa U,V wind at SW domain

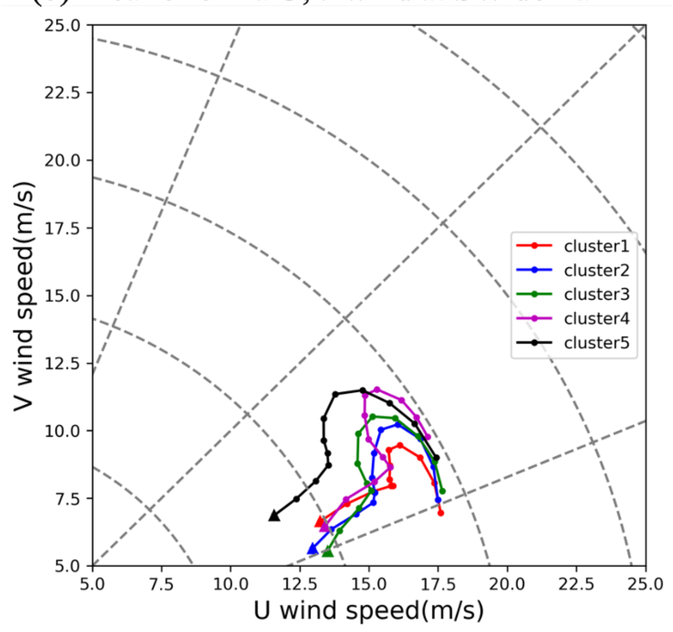

Fig. 45 (a) The simulated mean 925-hPa wind speed during pre-12hr rainfall period (0500 UTC 1 June to 0700 UTC 1 June) and the black box is the southwestern domain (SW domain). (b) Same as Fig. 44b but for the SW domain.

The characteristics of 8-hr accumulated rainfall in each cluster are further investigated through a time-series diagram (Fig. 46, and Fig. 47). As mentioned in 5.2.1, rainfall patterns are mainly affected by the evolution of the short-wave trough. The rainfall in clusters 1, 2, 3, and 5 all reveals a southward shift with time but within a slight time difference corresponding to the location of minimum low in Fig. 38. Different from the others, cluster 4 remains north of Taiwan due to the slower and northern eastward short-wave trough and ends up with max rainfall at about 26.5°N. The time series also show that both the mean and maximum rainfall evolutions reach an extreme value when the frontal system gets close to Taiwan, resulting from the topography effect and the short-wave trough effect (Fig. 47). For the model error in ensembles, the simulated members in each cluster display a similar feature on hourly rainfall at first and are apart from others through model integration (Fig. 47c). Previously, the positive contributions of a low-level jet or barrier jet to the convective system are proved in many studies (Chen and Yu 1988; Kuo and Chen 1990; Li et al., 1997; Li and Chen 1998; Chen 2005; Chen 2018; Ke 2019) that the magnitude of the jet in the prefrontal region is highly related to the vertical motion and convergence at the interface. In addition, the heavy rain occurs at which the trough passes, around 1200 UTC to 1500 UTC (cluser1,2,3, and 5) and after 1800 UTC (cluster4) (Fig. 47b). As a result, there shows sudden increments in rain and rainfall standard deviation when the two favorable conditions above are satisfied.

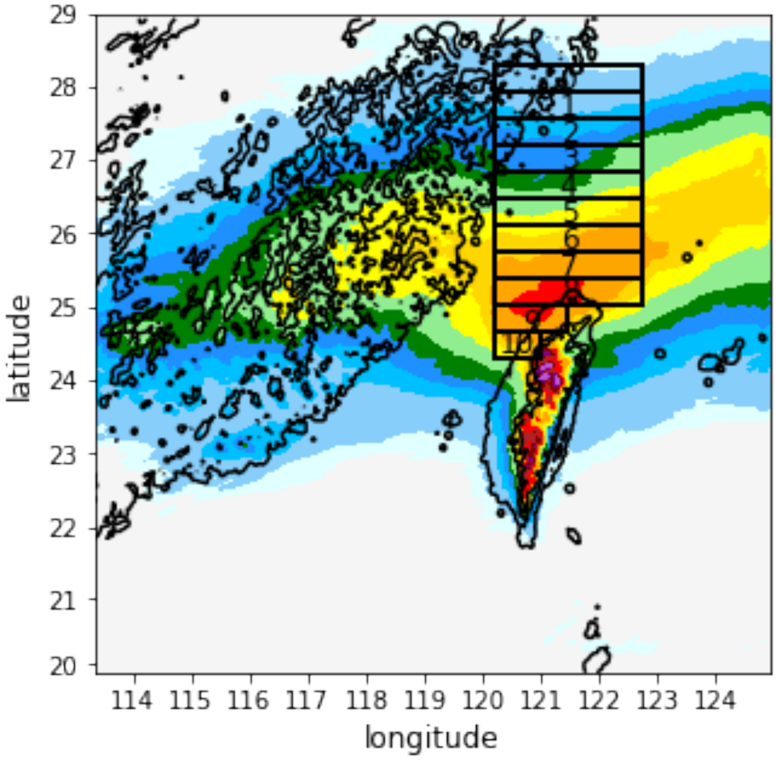

Fig. 46 The simulated accumulated rainfall within 8-hr from 1800 UTC 1 June to 0200 UTC 2 June at D03.

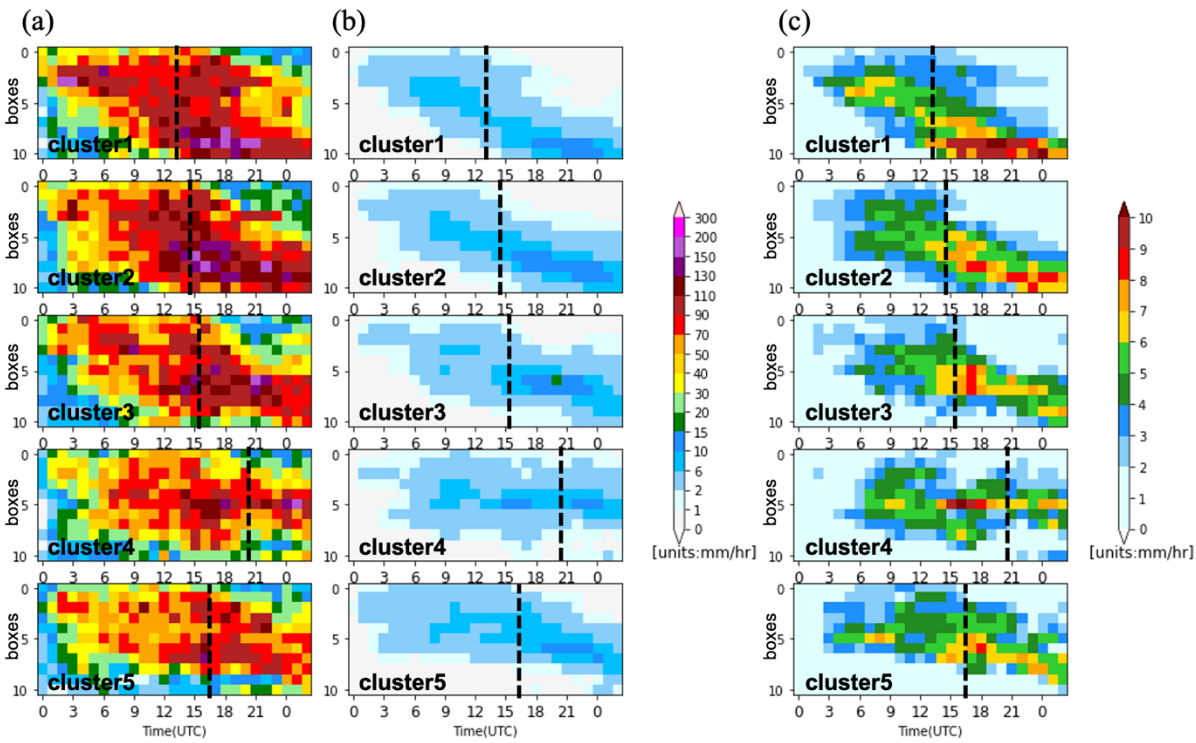

Fig. 47 The time series of (a) maximum accumulated rainfall in 8-hr at each box (b) mean accumulated rainfall in 8-hr at each box (c) rainfall standard deviation in each box from Fig. 46. Figures from the top to bottom indicate cluster 1 to 5. The dashed line indicates when the short-wave trough affects.

Chapter 6 Summary and future works

6.1 Summary

During 01-02 June 2017, an east-west quasi-stationary front stagnated in northern Taiwan and resulted in an extreme rainfall event of over 550 mm within 8 hours, with the abundant moisture and kinetic energy from the strong low-level jet. There were two main goals in this study, which are to: 1) investigate the dynamic structure of the 2017 Mei-Yu frontal case through the multiple Doppler wind retrieval algorithm results, and understand the interaction between barrier jet and the heavy rain; 2) with the advanced tools nowadays, such as cluster analysis or ensemble forecasts, try to find out the main factors of the extreme rainfall during the Mei-Yu season.

By the 3-dimensional wind and satellite images, the extreme precipitation lifetime can be separated into three parts that are southward moving, MCSs merging, and back-building stages.

1. In the first stage, the frontal cyclone kept moving southward from eastern China and reached the edge of Taiwan as the southeastward propagation of MCS-1. Due to the terrain blocking and frontal convections, a secondary downward motion was found and separated the barrier jet area. The MCS-1 decayed rapidly with less moisture and dynamic contributions from the jet at low level.
2. For the second stage, with the merging and reorganization of two MCSs (MCS-1 and MCS-2), the MCS restrengthened the front and resulted in a more tilted profile. Therefore, the secondary circulation was diminished and enhanced the 1-km barrier jet able to pass through northwestern Taiwan. Meanwhile, the low-level jet encountered the baroclinic system and forced the vertical velocity to its strongest strength at 2200 UTC.

3. In the last stage, a new MCS-5 formed upstream of the eastward moving MCS-4 and further made the frontal propagate southward inland.

Through WISSDOM, there reveals a strong connection between the strength of barrier jet and frontal system that stronger jet would enhance more powerful system. Then, we extend what we get from observations and cluster the 128 ensemble simulations, which can represent as the model uncertainty, to inspect the model performance and further investigate the Mei-Yu process in models in both meso-α and meso-β scales.

The cluster analysis part can be summarized into the following points:

1. The K-mean method was used for separating the rainfall characteristics of the 2017 heavy rainfall event in northern Taiwan; further, the five clusters illustrated different locations of extreme rainfall: some were over the ocean, and some were inland near west coast or northeast of Taiwan.
2. The different pre-storm environments and low-level pressure patterns can tell the spatial distribution of these clusters. For the pre-12hr period, a weak zonal wind as cluster 5 would result in a more west rainband, while a strong southwesterly wind may induce a quasi-stationary system northeast of Taiwan (cluster 4). The time series of dynamics variables also reveals that with the contribution of barrier jet or low-level jet would enhance the heavy rainfall as we studied in the retrieval results. The strong wind at low-level is a cause than the result.
3. Through the gaussian distribution feature of ensemble perturbations, cluster 2 remained the most similar pattern to the observation in both rainfall pattern and barrier jet location. Several threshold settings and statistics reveal that the frontal position is dominated in the model forecasts which also verify Wang et al. (2021)'s result.

4. Through the pressure gradient effect in previous studies, prevailing southwesterly wind would form a relatively high at southwestern Taiwan. With a faster short-wave trough moving eastward, the frontal rainband reached northern Taiwan earlier. The strong low at northwest Taiwan in cluster 5 results in a less zonal component of the pressure gradient force and further triggers a rainband at south edge of the low, and the strongest pressure gradient force in cluster 4 also enhances the rainband remain more northeastward.
5. The hodographs explained a connection between short-wave trough and wind near Taiwan and were consistent with the previous studies about barrier jet formation. The closer the trough moved, the stronger the pressure gradient formed. Therefore, the V-wind at the SW domain strengthened and could maintain the frontal convective system. After the trough left eastward, the meridional component of southwesterly decreased and turned to the original wind direction but with a stronger wind speed. In the meantime, the wind in NE domain changed from southwesterly and westerly wind to easterly with time and finally to the northeasterly wind, corresponding to the frontal strong wind shear structure. These features are also revealed in the time series of rainfall that heavy rainfall and larger uncertainty occur after the short-wave trough effect.

6.2 Future works

Based on the cluster-averaged hodograph of simulated mean wind in the BJ domain, NE domain, and SW domain, we validated the correlation between pressure gradient force and the frontal system as in previous research. To further understand the contribution of initial conditions to ensemble performances, in the future, we would like to investigate the feature of each variable with time. In the preliminary test, the 128-member wind patterns at pre-rainfall period (during 0500 UTC 01 June to 0700 UTC 01 June) and rainfall period (during 1800 UTC 01 June to 0200 UTC 02 June) in the BJ domain, NE domain, and SW domain are shown in Fig. 48, Fig. 49, and Fig. 50. Although they showed differences in hodographs (Fig. 43b, Fig. 44b, and Fig. 45b), the scatter plots with different colors reveal the feature of each member and the discrepancy of which cannot be easily told from the others.

In BJ domain, all members appear a clockwise turning and wind speed enhancement with time. Similar to the hodograph, the speed decrement of each cluster corresponds to the period when the southward frontal cyclone is the closest. With the low-level trough moving eastward away, the wind at NE domain turns from westerly to ENE which is related to the southwestern flank and southeastern flank of the 850-hPa cyclone. Therefore, a consistent U-wind reduction is revealed in almost all 128 members. Compared to the pre-12hr period, the southwesterly wind reacts stronger wind speed after the passage of the trough.

In Li and Chen (1998)'s study, the vertical wind shear features at both top and below the jet, while the shear is about $10 \times 10^{-3}\ s^{-1}$ below and $4 \times 10^{-3}\ s^{-1}$ above. The jet not only provide sufficient moisture and force to the system, the change with height also may be a sign of warm advection. To quantify the vertical wind shear effect, we try to use storm relative helicity (SRH) which can represent as the potential for cyclonic updraft rotation in right-moving supercells, and further analyze the connection between southwesterly wind shear and the front in the future.

Although there are some relationships between members in the cluster, the model uncertainty, thermodynamic process, initial conditions, and other factors may also play a role in these simulation results. For the verification of thermodynamics structure, we can apply the thermodynamics field by the Terrain-Permitting Thermodynamics Retrieval Scheme (TPTRS, (Liou et al., 2019)) to investigate the cold pool effect among the frontal system. More case studies and detailed considerations are needed to further understand the Mei-Yu that accompanied the extreme rainfall event.

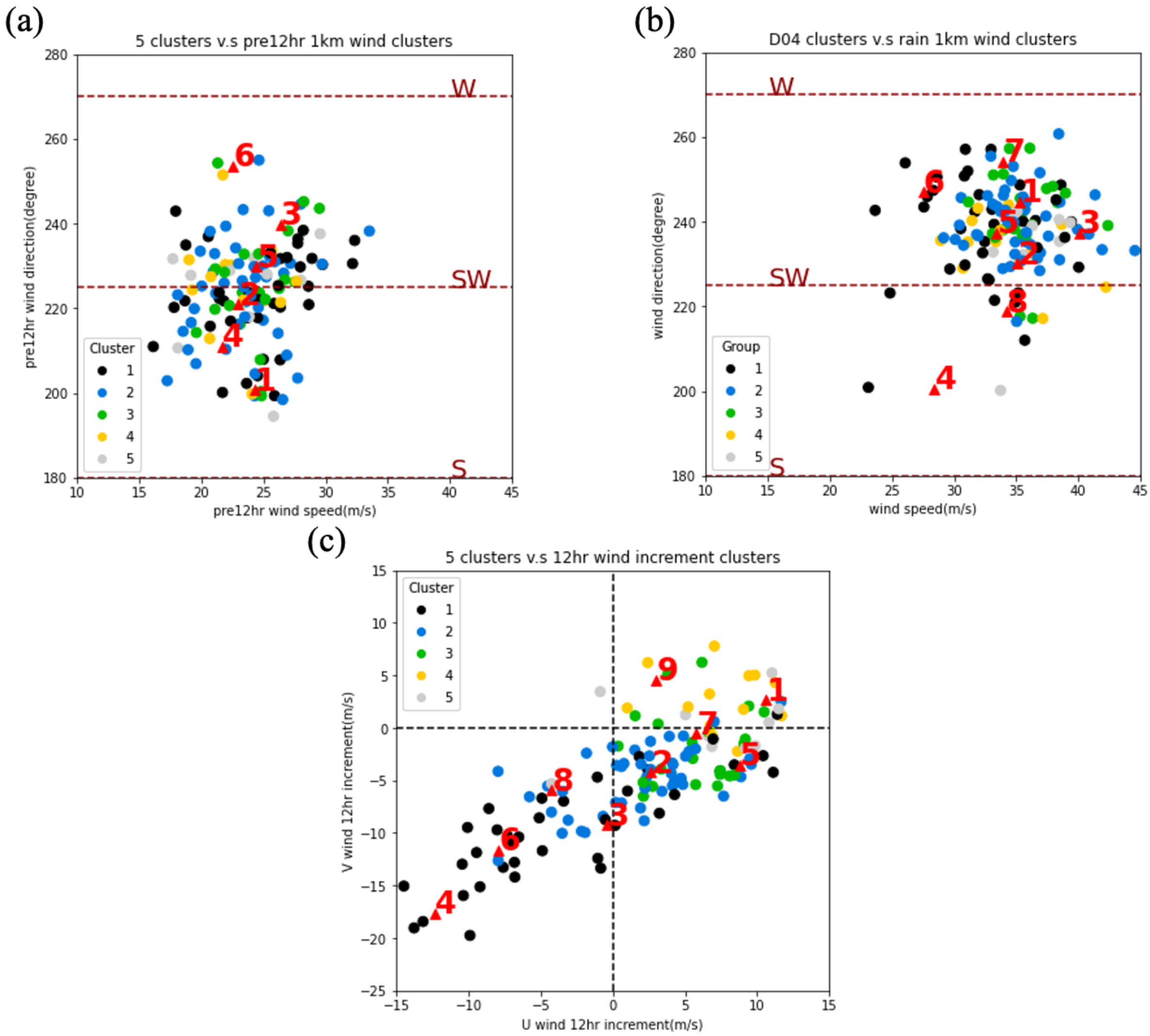

Fig. 48 The max 1-km wind speed and direction in BJ domain (a) during 0500 UTC 1 June 2017 to 0700 UTC 1 June 2017 (b) during 1800 UTC 1 June 2017 to 0200 UTC 2 June 2017. (c) The 12-hr mean increment of meridional and zonal wind in BJ domain for 128 members. The dot colors indicate 5 defined clusters, and the red triangles reveal the new cluster centers of the increment.

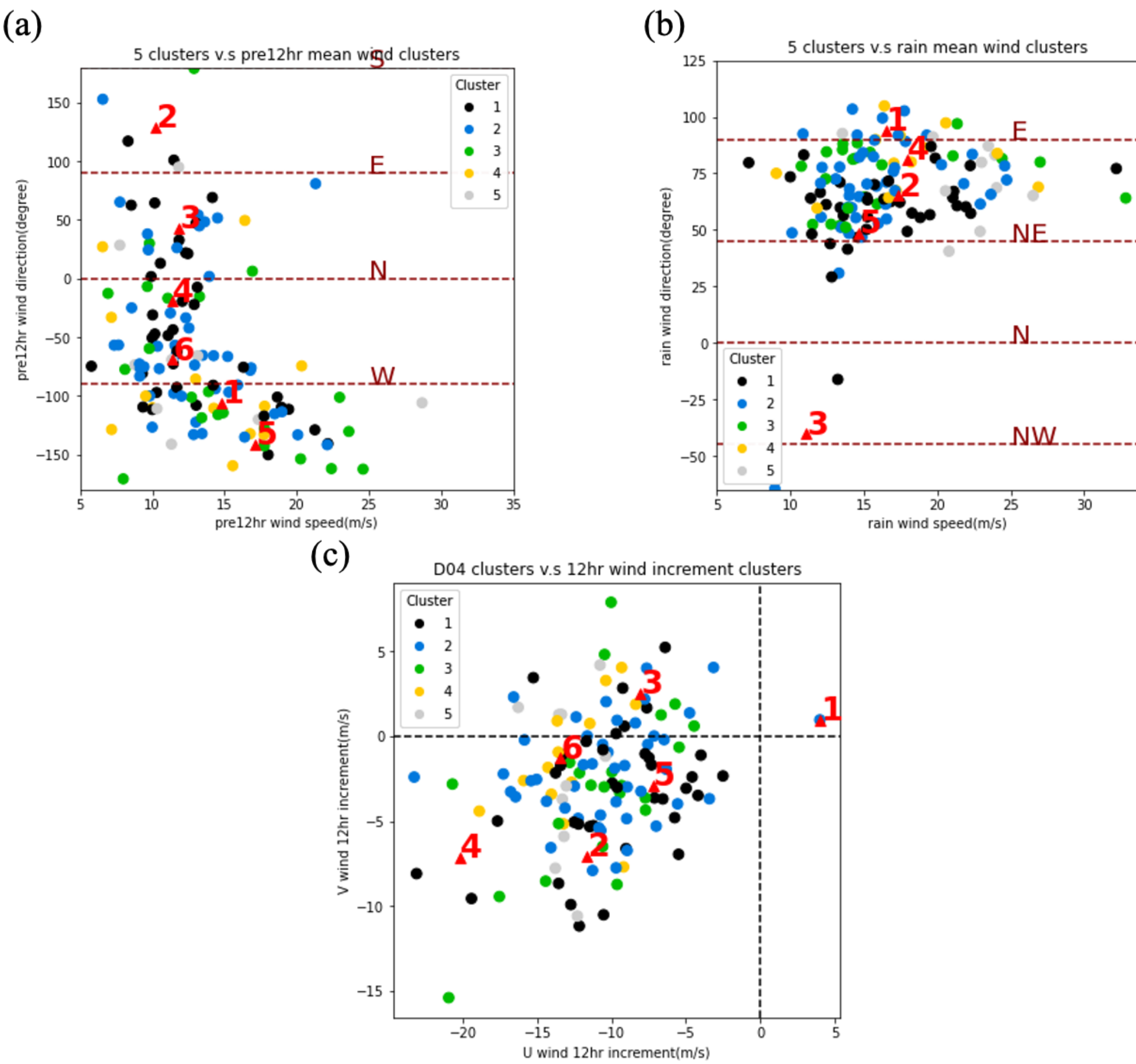

Fig. 49 Same as Fig. 48, but for the max wind speed and direction in NE domain.

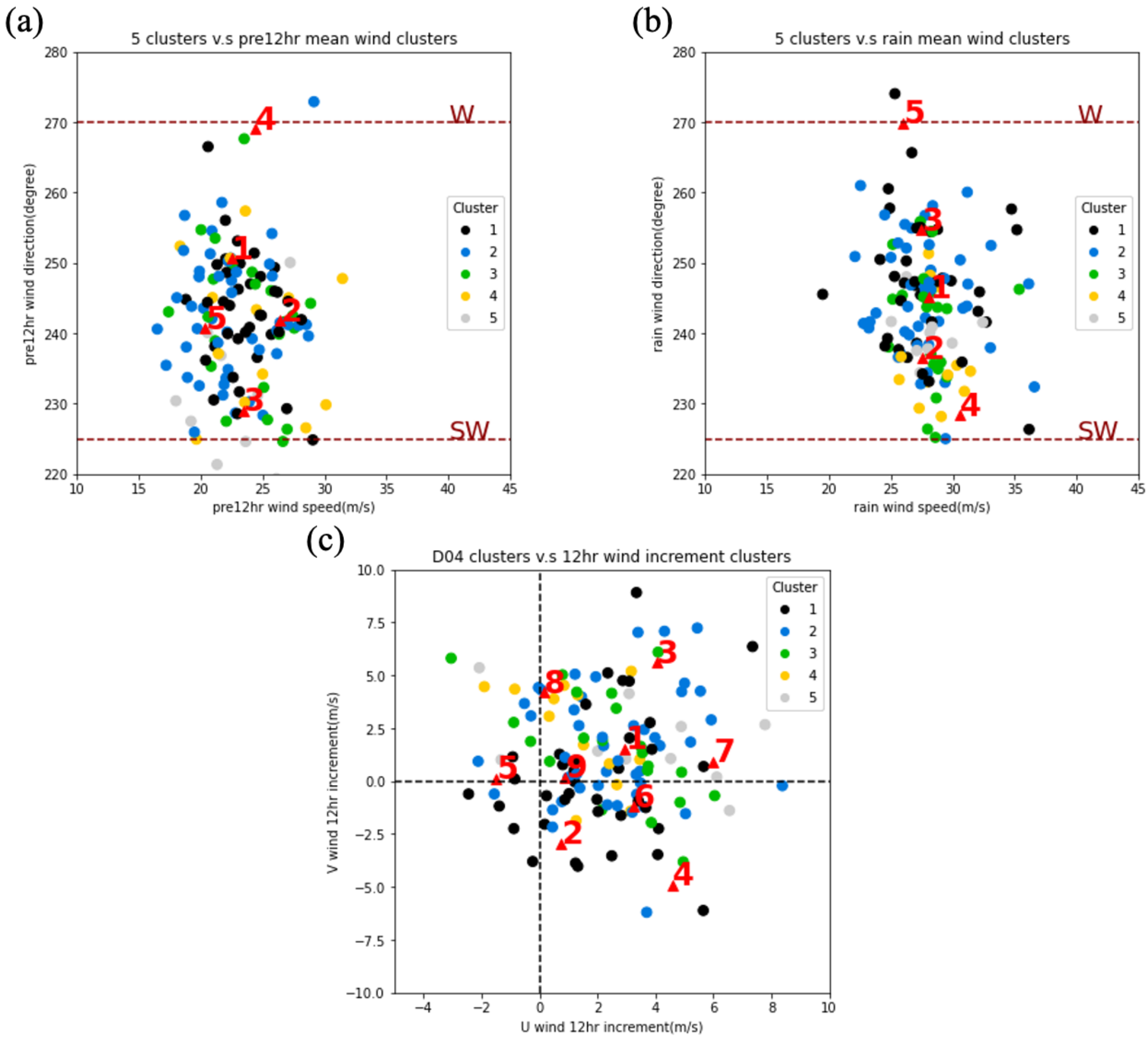

Fig. 50 Same as Fig. 48, but for the max wind speed and direction in SW domain.

References

簡芳菁、柳懿秦、周仲島、林沛練、洪景山、蕭玲鳳，2005：2003年梅雨季MM5系集降水預報

李志昕、洪景山，2014：區域系集預報系統研究：系集成員產生方式之評估

蘇凱翊，2016：使用群集分析分類綜觀尺度天氣型態以探討台灣北部地區午後熱對流系統局部環流結構與系統發展特性，碩士論文，國立中央大學大氣物理研究所

施筱柔，2019：2017年6月2-3日梅雨鋒面個案分析，碩士論文，國立中央大學大氣物理研究所

鄭羽廷，2019：同化雷達觀測與反演變數改善模式對流尺度降雨預報能力：探討OSSE與真實個案，碩士論文，國立中央大學大氣物理研究所

陳奕安，2019：多都卜勒氣象雷達反演之垂直速度的剖風儀驗證及高解析度三維風場反演能力的測試，碩士論文，國立中央大學大氣物理研究所

蔡博安，2020：評估TAHOPE觀測實驗同化S-PolKa徑向風、回波與折射指數對短期降雨預報的影響：觀測系統模擬實驗(OSSE)之測試，碩士論文，國立中央大學大氣物理研究所

莊秉學，2021：使用局地系集轉換卡爾曼濾波器同化雙偏極化參數的全新方法：夏季真實個案中的分析場與預報場，碩士論文，國立中央大學大氣物理研究所

蘇奕叡、賴曉薇等，2021：WEPS 降雨情境預報於梅雨預報應用之發展

Chen, C.-H., Chung, K.-S., Yang, S.-C., & Chen, L.-H. (2021). Sensitivity of Forecast Uncertainty to Different Microphysics Schemes within a Convection-Allowing Ensemble during SoWMEX-IOP8. *Monthly Weather Review,* **149(12)**, 4145-4166. https://doi.org/10.1175/mwr-d-20-0366.1

Chen, G. T.-J., Wang, C.-C., & Lin, D. D.-W. (2005). Characteristics of Low-Level Jets over Northern Taiwan in Mei-Yu Season and Their Relationship to Heavy Rain Events. *Monthly Weather Review,* **133**, 20-43. https://doi.org/10.1175/MWR-2813.1.

Chen, G. T.-J., & Yu, C.-C. (1988). Study of Low-Level Jet and Extremely Heavy Rainfall over Northern Taiwan in the Mei-Yu Season. *Monthly Weather Review,* **116**, 884-891. https://doi.org/10.1175/1520-0493(1988)116<0884:SOLLJA>2.0.CO;2

Chen, Y.-L., Chu, Y.-J., Chen, C.-S., Tu, C.-C., Teng, J.-H., & Lin, P.-L. (2018). Analysis and Simulations of a Heavy Rainfall Event over Northern Taiwan during 11–12 June 2012. *Monthly Weather Review,* **146(9)**, 2697-2715. https://doi.org/10.1175/mwr-d-18-0001.1

Chen, Y.-L., & Li, J. (1995). Characteristics of Surface Airflow and Pressure Patterns over the Island of Taiwan during TAMEX. *Monthly Weather Review,* **123**, 695-716.

Chen, Y.-L., Tu, C.-C., Hsiao, F., Chen, C.-S., Lin, P.-L., & Lin, P.-H. (2022). An Overview of Low-Level Jets (LLJs) and Their Roles in Heavy Rainfall over the Taiwan Area during the Early Summer Rainy Season. *Meteorology,* **1(1)**, 64-112. https://doi.org/10.3390/meteorology1010006

Chung, K.-S., Chiu, H.-J., Liu, C.-Y., & Lin, M.-Y. (2020). Satellite Observation for Evaluating Cloud Properties of the Microphysical Schemes in Weather Research and Forecasting Simulation: A Case Study of the Mei-Yu Front Precipitation System. *Remote Sensing,* **12(18)**. https://doi.org/10.3390/rs12183060

Du, Y., & Chen, G. (2018). Heavy Rainfall Associated with Double Low-Level Jets over Southern China. Part I: Ensemble-Based Analysis. *Monthly Weather Review,* **146(11)**, 3827-3844. https://doi.org/10.1175/mwr-d-18-0101.1

Dudhia, J. (1989). Numerical Study of Convection Observed during the Winter Monsoon Experiment Using a Mesoscale Two-Dimensional Model. *Journal of the Atmospheric Sciences,* **46(20)**, 3077–3107. https://doi.org/https://doi.org/10.1175/1520-0469(1989)046<3077:NSOCOD>2.0.CO;2

Hong, S.-Y., Kim, J.-H., Kim, J.-o., & Dudhia, J. (2006). The WRF single moment microphysics scheme (WSM). *Journal of the Korean Meteorological Society,* **42**, 129-151.

Ke, C.-Y., Chung, K.-S., Chen Wang, T.-C., & Liou, Y.-C. (2019). Analysis of heavy rainfall and barrier-jet evolution during Mei-Yu season using multiple Doppler radar retrievals: a case study on 11 June 2012. *Tellus A: Dynamic Meteorology and Oceanography,* **71(1)**. https://doi.org/10.1080/16000870.2019.1571369

Kohone. (2001). Self-Organizing Maps.

Kuo, Y.-H., & Chen, G. T.-J. (1990). The Taiwan Area Mesoscale Experiment(TAMEX): An Overview. *Bulletin of the American Meteorological Society,* **71(4)**, 488-503. https://doi.org/10.1175/1520-0477(1990)071<0488:TTAMEA>2.0.CO;2

Lang, S. E., Tao, W.-K., Chern, J.-D., Wu, D., & Li, X. (2014). Benefits of a Fourth Ice Class in the Simulated Radar Reflectivities of Convective Systems Using a Bulk Microphysics Scheme. *Journal of the Atmospheric Sciences,* **71(10)**, 3583-3612. https://doi.org/10.1175/jas-d-13-0330.1

Li, J., & Chen, Y.-L. (1998). Barrier Jets during TAMEX. *Monthly Weather Review,* **126**, 959-971. https://doi.org/10.1175/1520-0493(1998)126<0959:BJDT>2.0.CO;2

Li, J., Chen, Y.-L., & Lee, W.-C. (1997). Analysis of a Heavy Rainfall Event during TAMEX. *Monthly Weather Review,* **125**, 1060-1082. https://doi.org/10.1175/1520-0493(1997)125<1060:AOAHRE>2.0.CO;2

Lin, Y.-F., Wu, C.-C., Yen, T.-H., Huang, Y.-H., & Lien, G.-Y. (2020). Typhoon Fanapi (2010) and its Interaction with Taiwan Terrain – Evaluation of the Uncertainty in Track, Intensity and Rainfall Simulations. *Journal of the Meteorological Society of Japan. Ser. II,* **98(1)**, 93-113. https://doi.org/10.2151/jmsj.2020-006

Liou, Y.-C., Chang, S.-F., & Sun, J. (2012). An Application of the Immersed Boundary Method for Recovering the Three-Dimensional Wind Fields over Complex Terrain Using Multiple-Doppler Radar Data. *Monthly Weather Review,* **140(5)**, 1603-1619. https://doi.org/10.1175/mwr-d-11-00151.1

Liou, Y.-C., & Chang, Y.-J. (2009). A Variational Multiple–Doppler Radar Three-Dimensional Wind Synthesis Method and Its Impacts on Thermodynamic Retrieval. *Monthly Weather Review,* **137(11)**, 3992-4010. https://doi.org/10.1175/2009mwr2980.1

Liou, Y.-C., Chiou, J.-L., Chen, W.-H., & Yu, H.-Y. (2014). Improving the Model Convective Storm Quantitative Precipitation Nowcasting by Assimilating State Variables Retrieved from Multiple-Doppler Radar Observations. *Monthly Weather Review,* **142(11)**, 4017-4035. https://doi.org/10.1175/mwr-d-13-00315.1

Liou, Y.-C., Yang, P.-C., & Wang, W.-Y. (2019). Thermodynamic Recovery of the Pressure and Temperature Fields over Complex Terrain Using Wind Fields Derived by Multiple-Doppler Radar Synthesis. *Monthly Weather Review,* **147(10)**, 3843-3857. https://doi.org/10.1175/mwr-d-19-0059.1

Mlawer, E. J., Taubman, S. J., Brown, P. D., Iacono, M. J., & Clough, S. A. (1997). Radiative transfer for inhomogeneous atmospheres: RRTM, a validated correlated-k model for the longwave. *Journal of Geophysical Research: Atmospheres,* **102(D14)**, 16663-16682. https://doi.org/10.1029/97jd00237

Raut, B. A., de la Fuente, L., Seed, A. W., Jakob, C., & Reeder, M. J. (2012). Application of a Space-Time Stochastic Model for Downscaling Future Rainfall Projections. *Sydney, Australia: Engineers Australia*, 579-586.

Tao, W.-K., Simpson, J., Baker, D., Braun, S., Chou, M., Ferrier, B., Johnson, D. E., Khain, A., Lynn, B., Shie, C., Starr, D., Sui, C., Wang, Y., & Wetzel, P. (2003). Microphysics, radiation and surface processes in the Goddard Cumulus Ensemble (GCE) model.

Meteorology and Atmospheric Physics, **82**, 97-137. https://doi.org/10.1007/s00703-001-0594-7

Tao, W.-K., Simpson, J., & McCumber, M. (1989). An Ice-Water Saturation Adjustment.

Tao, W. K., Wu, D., Lang, S., Chern, J. D., Peters-Lidard, C., Fridlind, A., & Matsui, T. (2016, Feb 16). High-resolution NU-WRF simulations of a deep convective-precipitation system during MC3E: Further improvements and comparisons between Goddard microphysics schemes and observations. *J Geophys Res Atmos,* **121(3)**, 1278-1305. https://doi.org/10.1002/2015JD023986

Teng, H.-F., Lee, C.-S., Hsu, H.-H., Done, J. M., & Holland, G. J. (2019). Tropical Cloud Cluster Environments and Their Importance for Tropical Cyclone Formation. *Journal of Climate,* **32(13)**, 4069-4088. https://doi.org/10.1175/jcli-d-18-0679.1

Tu, C.-C., Chen, Y.-L., Chen, C.-S., Lin, P.-L., & Lin, P.-H. (2014). A Comparison of Two Heavy Rainfall Events during the Terrain-Influenced Monsoon Rainfall Experiment (TiMREX) 2008. *Monthly Weather Review,* **142(7)**, 2436-2463. https://doi.org/10.1175/mwr-d-13-00293.1

Tu, C.-C., Chen, Y.-L., Chen, S.-Y., Kuo, Y.-H., & Lin, P.-L. (2017). Impacts of Including Rain-Evaporative Cooling in the Initial Conditions on the Prediction of a Coastal Heavy Rainfall Event during TiMREX. *Monthly Weather Review,* **145(1)**, 253-277. https://doi.org/10.1175/mwr-d-16-0224.1

Tu, C.-C., Chen, Y.-L., Lin, P.-L., & Huang, M.-Q. (2022). Analysis and Simulations of a Heavy Rainfall Event Associated with the Passage of a Shallow Front over Northern Taiwan on 2 June 2017. *Monthly Weather Review,* **150(3)**, 505-528. https://doi.org/10.1175/MWR-D-21-0113.1

Turgu, E., & Kömüşcü, A. Ü. (2019). Using K-Means Methodology for Reclassifying Rainfall Regions of Turkey.

Wang, C.-C., Chiou, B.-K., Chen, G. T.-J., Kuo, H.-C., & Liu, C.-H. (2016). A numerical study of back-building process in a quasistationary rainband with extreme rainfall over northern Taiwan during 11–12 June 2012. *Atmospheric Chemistry and Physics,* **16(18)**, 12359-12382. https://doi.org/10.5194/acp-16-12359-2016

Wang, C.-C., Li, M.-S., Chang, C.-S., Chuang, P.-Y., Chen, S.-H., & Tsuboki, K. (2021). Ensemble-based sensitivity analysis and predictability of an extreme rainfall event over northern Taiwan in the Mei-yu season: The 2 June 2017 case. *Atmospheric Research,* **259**. https://doi.org/10.1016/j.atmosres.2021.105684

Yeh, H.-C., & Chen, Y.-L. (2003). Numerical Simulations of the Barrier Jet over Northwestern Taiwan during the Mei-Yu Season. *Monthly Weather Review,* **131**, 1396-1407. https://doi.org/10.1175/1520-0493(2003)131<1396:NSOTBJ>2.0.CO;2

Zhang, Q., Du, Y., Chen, Y.-l., Zhao, Y., & Wang, X. (2014). Numerical Simulations of Spatial Distributions and Diurnal Variations of Low-Level Jets in China during Early Summer. *Journal of Climate,* **27(15)**, 5747-5767. https://doi.org/10.1175/jcli-d-13-00571.1